Stony Brook University

The official electronic file of this thesis or dissertation is maintained by the University Libraries on behalf of The Graduate School at Stony Brook University.

X-ray Spectromicroscopy Analysis and Its Applications to Bacterial Interactions in the Environment.

A Dissertation Presented

by

Bjorg A. Larson

to

The Graduate School

in Partial Fulfillment of the Requirements

for the Degree of

Doctor of Philosophy

in

Physics

Stony Brook University

August 2008

Bjorg A. Larson

We, the dissertation committee for the above candidate for the Doctor of Philosophy degree, hereby recommend acceptance of this dissertation.

Chris J. Jacobsen – Dissertation Advisor
Professor, Department of Physics and Astronomy

George F. Sterman – Chairperson of Defense
Distinguished Professor, Department of Physics and Astronomy

John D. Hobbs
Associate Professor, Department of Physics and Astronomy

Jeffrey P. Fitts
Associate Geochemist, Environmental Sciences Department
Brookhaven National Laboratory

This dissertation is accepted by the Graduate School.

Lawrence Martin
Dean of the Graduate School

Abstract of the Dissertation

X-ray Spectromicroscopy Analysis and Its Applications to Bacterial Interactions in the Environment.

by

Bjorg A. Larson

Doctor of Philosophy

in

Physics

Stony Brook University

2008

The US Department of Energy must clean up a large number of sites with groundwater and soils polluted with multiple contaminants including heavy metals and radionuclides. Important *in situ* remediation approaches are being developed to reduce the bioavailability and prevent the further spread of these contaminants via groundwater transport by promoting the activity of microorganisms that will transform the contaminants into insoluble and immobile forms. In order for this approach to work the soil bacteria must be resistant to a wide range of co-contaminant metals such as nickel. Scanning Transmission X-ray Microscopy (STXM) provides the means for studying chemical speciation at the 30-50 nm spatial scale, and can be used to identify spectroscopic signatures of metal resistant mechanisms used by common soil bacteria.

We have been using pattern-recognition clustering techniques developed at Stony Brook in a unique way to identify subcellular

features in bacteria and to investigate the changes in bacterial chemistry due to interactions with contaminants in their environment. We can determine the functional group responsible for metal binding using the C1s absorption edge spectra. We can quantify the extent of the nickel binding associated with the cell wall, the interior of the cell, and surrounding the cell.

In addition, we have been using a segmented detector to record a dark field image simultaneously with the bright field absorption image. Dark field imaging identifies small strongly scattering objects, such as nanoparticles or metal precipitates and can be used in combination with bright field absorption data to determine the spatial distribution of the precipitates in relation to the bacterium.

Dedicated to my parents.

Contents

List of Figures

List of Tables

Acknowledgements

First I thank my thesis advisor, Chris Jacobsen, for all his support and encouragement during my time at Stony Brook. From the beginning he encouraged me to continue through my early frustrations and helped to find me a project that I found interesting.

I began work with Jeff Gillow through the Center for Environmental Molecular Science (CEMS) at Stony Brook, while he was in the Department of Environmental Science at BNL. Jeff introduced me to the world of microbiology and environmental science, and his incredible breadth and depth of knowledge was inspiring.

I was sorry to see Jeff Gillow leave BNL, but I was extremely lucky to have Jeff Fitts, geochemist in the Department of Environmental Science at BNL, continue the bacteria project with me. I can't thank him enough for all his help, encouragement, and endless discussions on data analysis.

David Moreels, formerly in the Biology Department at BNL, prepared many of our bacteria samples, especially in the last year of our experiments. He was crucial to our understanding of much of the microbiology, particularly the nickel-resistant organisms.

I would not have survived the beamline without Sue Wirick's endless patience and knowledge. Thank you Sue!

And thank you to Holger Fleckenstein, solver of all problems computer, hardware, logical and grammatical.

Chapter 1

Introduction

1.1 The Role of Nanoscale Bacterial Chemistry in Environmental Sites

Contaminated soil and groundwater sites generally require large expenditures of energy and money by the federal government on short term remediation efforts and long term monitoring programs. The most common methods in use require simply digging up or pumping out of large quantities of contaminated soil or water and transporting the excavated soils and waste to a new, presumably safe storage site. There is great interest in developing *in situ* remediation techniques, in which the contaminants are destroyed or immobilized by the addition of chemical or biological agents. These techniques are particularly useful in subsurface environments, where the inaccessibility of these areas make traditional methods difficult.

Microorganisms are capable of transforming contaminants through a variety of methods. They can change soil chemistry by altering the oxidation-reduction potential of their environment which affects metal speciation; they may even use toxic metals and radionuclides as electron acceptors for anaerobic respiration. For example, some species of Clostridium will use Fe(III) oxides such as geothite and ferrihydrite as electron acceptors in respiration. This metabolic pathway results in a change in the valence state of Fe(III) to Fe(II), and the resulting change in solubility from the relatively insoluble Fe(III) to the soluble Fe(II) [1]. Microorganisms also transform organic metabolites and exudates, and can biodegrade organic contaminants. Through these processes they can change the toxicity and mobility of contaminants and radionuclides.

A common type of bioremediation is the oxidation of toxic contaminants to non-toxic products by using oxygen as an electron receptor in respiration. This process can degrade many types of organic contaminants such as pesti-

cides or aromatic hydrocarbons. The bacterium genus *Pseudomonas* has been studied extensively for its ability to degrade many different contaminants. In environments where oxygen is not available for respiration, microorganisms will use alternate electron acceptors, such as nitrate, sulphate and Fe(III) oxides. Increasing the availability of these electron acceptors can stimulate the degradation of organic contaminants.

Some contaminants serve as electron acceptors rather than electron donors. For example, in reductive dechlorination, microorganisms remove chlorines from contaminants by using the chlorinated compounds as electron acceptors in respiration. Inorganic chlorine compounds such as nitrate and perchlorate can be reduced to nontoxic products by some microorganisms. Metals can also be used by microorganisms as electron receptors. The result of these reactions is not the destruction of the metals but solubility and biotoxicity changes. For example, the soluble form of uranium, U(VI), can be reduced by *Geobacter* species to the insoluble form, U(IV). This causes precipitation of the uranium from groundwater, preventing its spread. It also means that because *Geobacter* can use uranium as an electron receptor in respiration, its growth is stimulated in uranium-contaminated environments.

1.2 Methods to Study Chemistry at the Nanoscale

Various bulk methods have traditionally been applied to studying the chemistry of biological specimens. But improvements in the spatial resolution of imaging techniques make it possible to determine the location in the sample of specific chemistry. This is important because the sample may contain a mix of bacteria, precipitates, clays and other things. Bulk methods will average these very different chemistries together. A bacterium itself has internal structure that varies in chemistry, as will be shown in Chapter 4 of this thesis by showing spectroscopic information on a nanoscopic scale.

We will now discuss methods available for microscopic studies of biological specimens, such as visible light microscopy and fluorescence imaging, electron microscopy, and finally x-ray microscopy.

1.2.1 Visible Light Microscopy

Visible light microscopy has the advantage of viewing the specimen without destroying it. That is, a biological specimen can be viewed *in vivo* and observed over time to record dynamic changes in the sample. The major disadvantage of

light microscopy in the visible range is the resolution limit determined by the wavelength itself. The visible region of the electromagnetic spectrum ranges in wavelength from about 400 to 700 nm, and so the resolution possible for a standard light microscope is restricted by this wavelength.

The classical lateral resolution of a microscope is determined by the diffraction of light by the specimen and the objective lens [2]. The minimum distance d between two points before they can no longer be resolved as two separate points can be written

$$d = \frac{1.22\lambda}{\text{NA}},$$
(1.1)

where λ is the wavelength of the light used in imaging and NA is the numerical aperture. The numerical aperture is $\text{NA} = n\sin\theta$, determined by the acceptance half-angle of the lens, θ, and the index of refraction of the medium in which the lens is immersed, n.

To study chemistry using visible light microscopy, dyes have traditionally been used. For example, the Gram stain, developed in 1884 by Christian Gram, is a method to divide bacteria into two major classes based on the chemical and physical structure of their cell wall. Other stains target specific proteins that make up certain parts of a cell, such as the membrane or nucleus.

Fluorescence Microscopy

Another approach to the chemical labeling of specimens for microscopy is the use of fluorescent labels and dyes. In fluorescent microscopy the idea is that only that which fluoresces is imaged, and nothing else. In practice however, there may be overlaps of the exciting or fluorescing spectra and auto-fluorescence of molecules in the sample that can complicate the image. Chemists have developed over 3000 fluorescent probes to label almost any part of a biological specimen.

The term 'fluorescence' was first used in 1852 by George Stokes to describe the light that was emitted by fluorspar when illuminated by an ultraviolet light source. Later it was found that many minerals fluoresce, and the first fluorescence microscope was built in 1904. In fluorescence, an atom or molecule absorbs light of a particular wavelength, called the exciting wavelength. This wavelength depends on the electronic structure of the atom or molecule. Nanoseconds after the absorbtion of this energy, the atom releases the energy as a second photon of a different wavelength, called the emitted wavelength. This difference in exciting and emitted wavelengths is called the Stokes shift, and results from relaxations within the excited states.The Stokes shift allows one to filter out the exciting light and detect only the fluorescence from the sample.

Source Pinhole	Condenser	Sample	Objective	Detector Pinhole
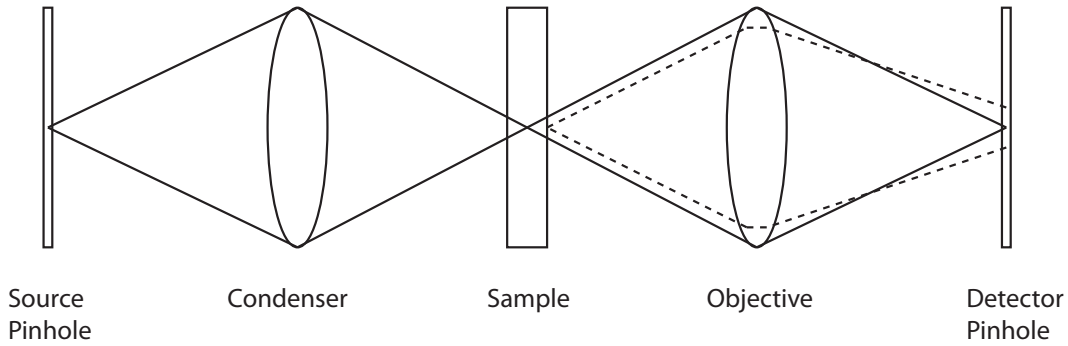
Figure 1.1: Confocal imaging schematic. The condenser lens forms an image of the source pinhole on the object. The objective lens forms an image of the focal spot on the exit pinhole, which is confocal to the first pinhole. The light that is not in the focal plane will be excluded from entering the exit pinhole.

Confocal Imaging

Confocal imaging was developed to improve the resolution, depth of focus, and contrast of the traditional visible light microscope. Optical sections can be imaged in a thick specimen, and background information away from the focal plane can be reduced or eliminated.

In a confocal imaging system, shown in Figure 1.1, the condenser lens forms an image of the source pinhole on the object. The objective lens forms an image of the focal spot on the exit pinhole, which is confocal to the first pinhole. If the specimen is thick, light that is not in the focal plane will be excluded from entering the exit pinhole. The sample is then raster scanned through the focal spot to form an image.

This confocal imaging scheme has several advantages over a traditional microscope. There is reduced blurring of the image from light scattering and improved signal to noise ratio due to the exclusion of out of focus light by the pinhole. Improvement in resolution comes from the fact that the numerical aperture, (NA), is greatly reduced.

Fluorescent imaging techniques are ideal for use in the confocal system. In a conventional epifluorescence setup, fluorescence from many layers of the sample would overwhelm the image. The Stokes' shift in wavelength of the emitted light makes the folded diagram in Figure 1.2 possible. In this setup, a single lens serves as both condenser and objective. A dichromatic mirror can be used to reflect the exciting light onto the sample while passing the emitted light through to the detector. In this way the illuminating light does not contribute to the image.
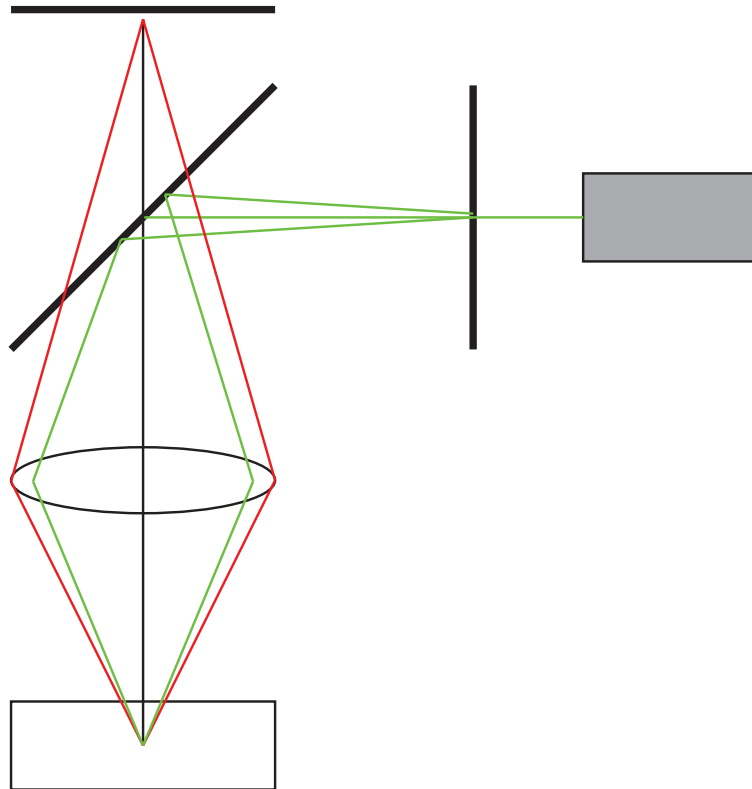
Figure 1.2: The folded confocal schematic. The Stokes' shift in wavelength of the emitted light makes this folded diagram possible. A single lens serves as both condenser and objective. A dichromatic mirror can be used to reflect the exciting light onto the sample while passing the emitted light through to the detector.

1.2.2 Electron Microscopy and Electron Energy-Loss Spectroscopy

Electron microscopy is another method used to study environmental microbes, and has the advantage of very high spatial resolution. In a transmission electron microscope (TEM), electrons are accelerated and focused onto a thin sample, then post-specimen optics are used to form an image. The sample must be thin-sectioned and mounted in vacuum. Samples generally must be less than 100 nm thick. The spatial resolution can be as high as 1 nm for biological, or 'soft' samples and 0.1 nm for 'hard' samples.

A transmission electron microscope (TEM) can be used for electron energy-loss spectroscopy (EELS). The electrons transfer energy to the molecules and atoms in the sample via inelastic scattering. The EELS spectrum provides information that overlaps in part with what can be provided in the soft x-ray and UV spectral regions. The amount of energy lost is characteristic of the type of atom or molecule, and so chemical analysis of the sample is possible. See Figure 1.3 for an example of an EELS spectrum.

The zero-loss peak includes both electrons that pass undeflected through the sample and electrons that excite phonon modes in the sample. Phonon or lattice modes are associated with the vibrations of the lattice itself, and typically require so little energy that they are indistinguishable from the elastically scatters electrons. Elastically scattered electrons interact with the atom nucleus and lose no energy but are strongly deflected as they pass through the sample. The angular distribution of the elastically scattered electrons differs from the inelastically scattered electrons, and can be used to estimate the atomic number Z of the atom.

Inelastically scattered electrons are those that have lost energy in interactions with the electrons in the sample. Low-energy losses are due to scattering with the outer shell electrons of the atom and can give information about the solid-state character of the sample. This low-energy loss peak from 5-50 eV is also known as the plasmon peak.

At higher energy loss, there are resonances corresponding to the energy required to ionize an inner-shell electron from its atom. Because each element has unique electron binding energies, one can study a specific element surrounded by atoms of other elements by using the characteristic ionization edge. The energy-loss near edge structure (ELNES) region of the spectrum is just below the ionization edge of an element. Spectra in this region provide information on the chemical bonding and density of states of the edge element. The ELNES region corresponds to x-ray absorption near-edge spectroscopy (XANES). The extended energy loss fine structure (EXELFS) region of the spectrum lies beyond the ionization edge, and has details of the bond distance
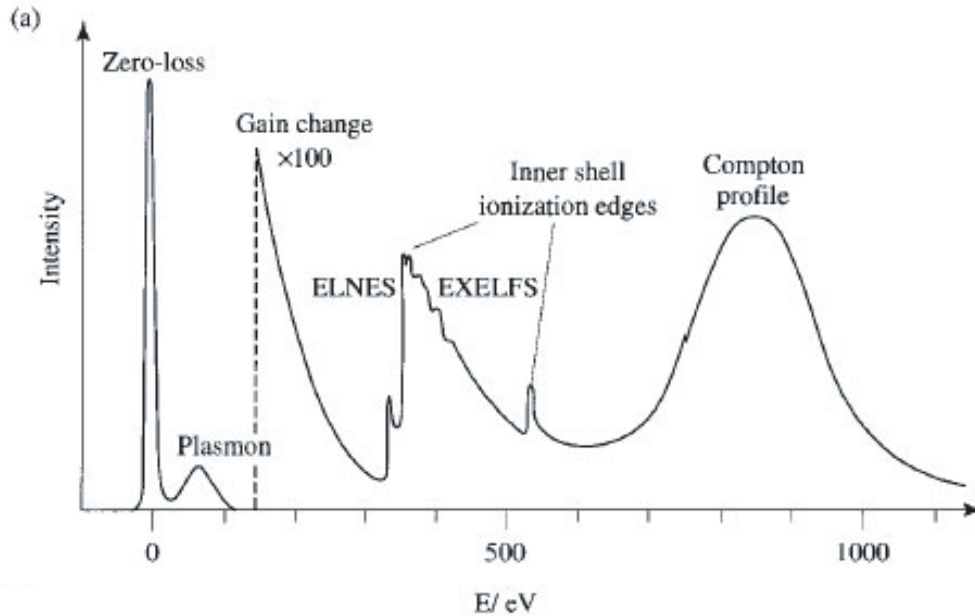
Figure 1.3: An example of a typical EELS spectrum, from [3]. The zero-loss peak includes unscattered electrons, with a finite width determined by the experimental apparatus. The wide plasmon peak corresponds to valence electron excitations in the sample by the incoming electrons. The ionization peak of an element is preceded by the energy-loss near edge structure (ELNES) which provides insight into the chemical bonding and density of states of the edge element. An analysis of the extended energy-loss fine structure (EXELFS) beyond the ionization edge gives details of the bond length and coordination numbers of the element.

and coordination number of the atom, and corresponds to the extended x-ray absorption fine structure (EXAFS). XANES and EXAFS will be discussed in more detail in Chapter 3.

The inner-shell ionization edges are superimposed on a decreasing background from the tails of other processes. Because the edge intensity is comparable, or less than, the background, a careful subtraction must be made. For thin samples this background comes from two sources. The first is the tail of the broad plasmon peak at low energy loss. This tail decreases as E^{-3} for high energies, and can be subtracted from the region. The second source of background comes from the tails of inner shell edges at lower energy. These tails are generally fit with a least-squares fit or the 'two-area' method. [3]

As the sample thickness approaches and exceeds the mean free path for

inelastic scattering events, it becomes likely that a single electron would inelastically scatter more than once in the sample. This results in a total energy loss that is a sum of the energy lost in each scattering event. For 100 keV electrons, the mean free path is between 50-100 nm for outer shell scattering. The mean free path for inner shell scattering events is long compared to specimen thickness, so it is unlikely that a single electron would produce more than one inner shell event. But it is probable that an electron that has produced a single inner shell excitation would then produce an outer shell event, resulting in a broad peak above the ionization threshold. This peak can be removed from the spectrum by deconvolution methods such as Fourier-log deconvolution [4].

A typical EELS setup consists of a standard TEM with a magnetic prism spectrometer mounted below. Electrons exiting the microscope in the z-direction enter a magnetic field B in the y-direction. An electron with speed v will travel in a circular orbit of radius

$$R = (\gamma m_0/eB)v, \tag{1.2}$$

where $\gamma = 1/(1 - v^2/c^2)^{1/2}$ and m_0 is the rest mass of the electron. The deflection of the electron as it exits the region of magnetic field depends precisely on its velocity within the field. Electrons with higher energy loss and therefore lower velocity will have a larger deflection angle. Recording of the spectrum can be serial, in which the electrons are scanned across a slit that selects only one channel at a time, or parallel, in which the entire spectrum is recorded at once using a position sensitive detector such as a photodiode or CCD array. Because the dispersion is fairly low, about 2 μm per eV for 100 keV electrons, serial recording requires a very finely machined slit and reliable scanning mechanisms. Serial recording is inefficient, resulting in a longer recording time and therefore higher radiation dose to the sample, but can be used for recording spectra in the low-loss region. For parallel recording, magnifying optics are generally used to increase the energy resolution of the detector.

The electrons are produced for the TEM by an electron gun consisting of a thermal source at temperature T_s and an accelerating voltage V. These electrons have an energy spread with $\Delta E_s = 2.45(kT_s)$ as described by free-electron theory [5]. This spread is further increased by parameters of the microscope such as accelerating voltage, vacuum conditions and cathode temperature. A Wien filter, which consists of both electrostatic and magnetic fields, can be used in conjunction with an energy-selecting slit as a monochromator.

The energy resolution ultimately depends on the spread of the source, the resolution of the detector, and aberrations in the magnifying optics. Typical energy resolution is 0.1-0.5 eV. [3]

1.2.3 X Rays

Soft x rays have a photon energy between 100-1000 eV, or wavelengths between 1-10 nm. This wavelength provides the potential for high spatial resolution, and the photon energy is matched to the inner-shell binding energies of low-Z elements. This gives great penetration depth for biological samples. Photoelectric absorption is the dominant process for this energy range. Compton scattering has a small and negligible cross-section in this region. Elastic scattering is only important when the scattering amplitudes constructively interfere, as in the case of crystals. The transmission of x rays through the sample can be described by the Lambert-Beer law,

$$I = I_0 \exp -\mu z, \tag{1.3}$$

where I_0 is the intensity of the beam incident on the sample, I is the transmitted intensity, μ is the absorption coefficient of the material and z is the material thickness. The absorption coefficient, μ, will be discussed in Chapter 3. The soft x ray energy range is particularly suited to imaging of hydrated biological samples, due to the 'water window' [6] between the carbon and oxygen edges, as shown in Figure 1.4. The $1/e$ penetration depth of x rays for protein and water is plotted versus photon energy, showing the contrast between highly absorbing carbon-rich sample and water. Also plotted is the mean free path λ of electrons for elastic and inelastic scattering. X rays have far greater penetration depth in biological samples than electrons. This allows x-ray imaging of whole, unsectioned biological samples up to 1 μm in thickness.

At the absorption edge of an element, the absorption coefficient, μ, undergoes a steplike increase. If the energy of the x ray incident on the sample is close to, but not great enough to completely remove an inner shell electron from the atom, it may excite the electron into a molecular orbital just below the ionization threshold. This excitation process results in x-ray absorption near-edge structure (XANES) in the region of the absorption edge. XANES is also known as near-edge x-ray absorption fine structure (NEXAFS). A schematic of the process and resulting spectrum is shown in Figure 1.5. Fine-tuning of the x-ray energy near the absorption edge of an atom provides sensitivity to the chemical bonding state of atoms of that type. The first exploitation of chemical state transmission imaging was performed at the Stony Brook beamline X1A by Ade *et al.* [7].

Table 1.1 compares x-ray and electron spectroscopy techniques. While the spatial resolution of electrons is considerably higher for electrons, the energy resolution of x-ray sources is better.

X ray interactions with matter will be described in greater detail in Chap-
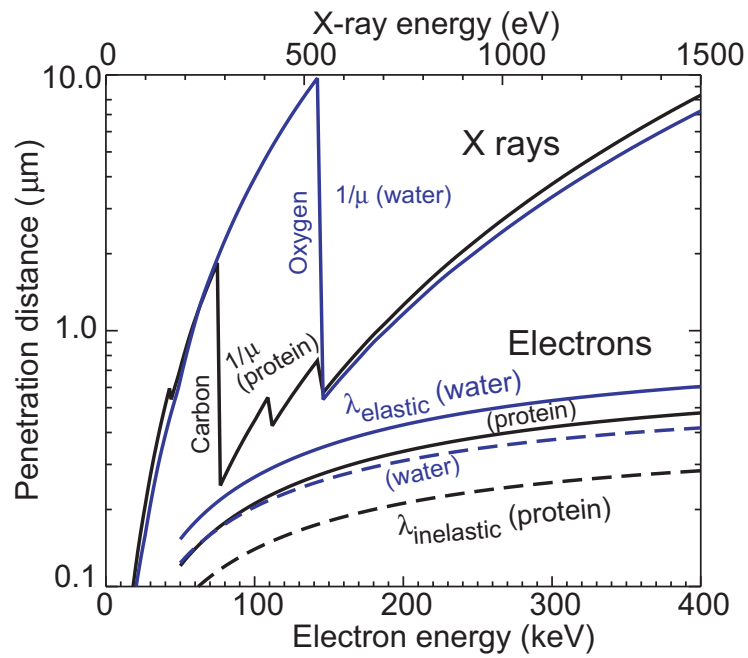
Figure 1.4: The penetration depth for x rays for water and protein is plotted between the carbon and oxygen absorption edges. Protein is highly absorbing in this so-called 'water window', making it an ideal region to image hydrated biological samples. X rays are far more penetrating than electrons, which allows whole samples to be imaged without sectioning.
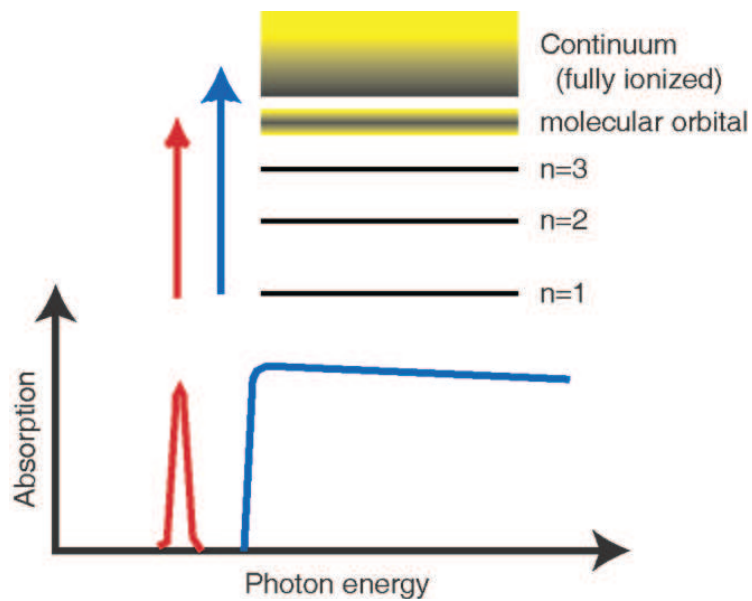
Figure 1.5: At the absorption edge of an element the absorption coefficient, μ, increases in a steplike manner. A photon that does not have enough energy to remove an inner shell electron from the atom may excite it into an orbital just below the vacuum level. These excitations result in the XANES spectrum.

	EELS	STXM
Spatial resolution	0.1 nm	30-50 nm
Energy resolution	0.1-0.5 eV	0.05-0.1 eV
Specimen thickness	< 100 nm	< 1 μm
Sample mounted	in vacuum	in atmosphere

Table 1.1: A comparison of x-ray and electron spectroscopy techniques.

ter 3.

1.3   Summary of work in this dissertation

Based on the above discussions of microscopy techniques, x-ray microscopy would have a nice advantage for studying microbial interaction in the environment. This dissertation takes up the challenge of realizing the advantages of x-ray microscopes in three main discussions. Chapter 2 will cover the requirements needed for a scanning transmission x-ray microscope (STXM). This will include a discussion of flux, brightness and monochromaticity and focusing of the x-ray beam as well as motor scanning and xray detectors. This will lead to a section on dark field imaging which includes a demonstration of dark field imaging of gold nanoparticles using the segmented silicon detector on beamline X1A2 at NSLS. Chapter 3 begins with a lesson on the refractive index and x-ray absorption edges. The near-edge region contains information about the chemical speciation of the edge element, but the data are complicated to unravel. Thickness calculations on simulated and actual samples and the extension of existing spectromicroscopy analysis techniques to infrared data will also be covered in Chapter 3. In Chapter 4, these analysis techniques will be applied to studies of soil bacteria.

Chapter 2

The X1A STXM

2.1 Requirements for STXM

In a scanning transmission x-ray microscope (STXM), spectroscopy and imaging are combined to form data sets containing spectral information about a sample at a spatial resolution of 30 nm. This chapter will include a discussion of the requirements for a STXM and the specific parameters of the STXM run by the Stony Brook X-ray Microscopy group at the National Synchrotron Light Source at Brookhaven National Lab. Look to Figure 2.1 for a schematic of beamline X1A at NSLS. An undulator produces a bright x ray beam which is monochromatized and focused onto the sample. The sample is scanned through the focal point using a combination of stepper and piezo motors. The x ray energy is incremented between each sample scan, which results in a spectrum at each pixel of the sample across the absorption edge of an element. X ray interactions in material and analysis of these spectra will be discussed in Chapter 3.

2.1.1 X Ray Sources: The X-ray Tube

A traditional source of x rays is the x-ray tube. X-ray tubes are widely used in areas including medical and dental diagnostics, non-destructive testing in industry, and scientific applications. In an x-ray tube, electrons are "boiled off" the cathode and accelerated until they strike the anode. X rays are produced by two mechanisms, bremsstrahlung and characteristic x rays. Bremsstrahlung, or braking radiation, is emitted as the electrons are quickly decelerated as they strike the anode, producing a continuum of radiation, the peak of which depends on the energy of the incident electron. If the electrons have sufficient energy to knock some inner-shell electrons out of the anode

material, outer shell electrons drop down to fill the vacancy. During the transition from the outer shell to inner shell, characteristic x rays are emitted. The energy of the x ray is equal to the energy difference between the two transition levels.

2.1.2   X Ray Sources: Synchrotron Radiation

For x-ray microscopy, an x-ray tube does not provide the brightness needed. Other sources of x-rays have been developed to provide high flux and high brightness sources. Synchrotron radiation was first observed in 1947 at a synchrotron in Schenectady, NY. It uses the fact that accelerated charges emit radiation. For an accelerated charge in nonrelativistic motion the angular distribution shows a simple $\sin^2\theta$ behavior, called the Larmor result for the power radiated per unit solid angle [8]:

$$\frac{dP}{d\Omega} = \frac{e^2}{4\pi c^3}|\dot{\boldsymbol{v}}|^2 sin^2\theta. \tag{2.1}$$

For relativistic motion the fields depend on the velocity as well as the acceleration. The power distribution for a particle whose acceleration is parallel to the velocity vector, such as in a linear accelerator, becomes

$$\frac{dP}{d\Omega} = \frac{e^2\dot{v}^2}{4\pi c^3}\frac{\sin^2\theta}{(1-\beta\cos\theta)^5}, \tag{2.2}$$

where $\beta \equiv v/c$, v is the velocity of the particle, and θ is the angle measured with respect to the direction of propagation. For $\beta \ll 1$, this equation reduces to the Larmor result of Eq. 2.1. But as $\beta \to 1$, the angular distribution is pushed forward and the magnitude of the radiation increases as well. Therefore for relativistic particles, the radiation is confined to a narrow cone in the direction of propagation of the particle. In the bending magnet of a synchrotron, however, the acceleration vector of the particle is perpendicular to the velocity vector. The power distribution in the relativistic limit ($\gamma \gg 1$) is approximately

$$\frac{dP}{d\Omega} \simeq \frac{2e^2}{\pi c^3}\gamma^6\frac{|\dot{\boldsymbol{v}}|^2}{(1+\gamma^2\theta^2)^3}\left[1 - \frac{4\gamma^2\theta^2\cos^2\phi}{(1+\gamma^2\theta^2)^2}\right]. \tag{2.3}$$

The electron in this bending magnet radiates into a fan in the horizontal direction. The total power radiated from this transversely accelerated electron is a factor of γ^2 larger than the power radiated in the case of the parallel acceleration.

2.1.3   X ray Sources: Undulators

The magnetic structure, or lattice, of a second-generation synchrotron ring is designed to allow for straight sections between bends in which the dispersion of the electrons is very small. An undulator is a periodic magnetic structure inserted into the straight section to produce very bright radiation. A series of magnetic dipoles creates an alternating magnetic field along the length of the undulator. The undulator wavelength, λ_u, refers to the wavelength of the alternating magnetic field, or the distance between successive dipoles. The relativistic electrons oscillate due to the alternating magnetic field and radiate into a narrow cone. Because of Lorentz contraction and the relativistic Doppler shift, the wavelength of the radiation is of the order $\lambda_u/2\gamma^2$, where $\gamma \equiv 1/\sqrt{(1 - v^2/c^2)}$, v is the relative velocity and c is the velocity of light in vacuum. As γ can have a value of several thousand, undulator magnet periods of centimeters are capable of producing x ray wavelengths of angstroms [9].

To calculate the radiation output of an undulator we need to find the motion of the electron in the alternating magnetic field of the undulator. The force equation for a charge in the presence of electric and magnetic fields can be written

$$\frac{d\mathbf{p}}{dt} = q(\mathbf{E} + \mathbf{v} \times \mathbf{B}) \tag{2.4}$$

where $\mathbf{p} = \gamma m \mathbf{v}$ is momentum, q is the charge, $\mathbf{v}$ is the velocity, and $\mathbf{E}$ and $\mathbf{B}$ are the electric and magnetic fields.

There are no applied electric fields in undulators, and except for the case of free-electron lasers, the radiation field produced by the electrons is too weak to affect their motion [9].

The electron motion in the transverse direction depends on the magnetic strength parameter,

$$K \equiv \frac{eB_0\lambda_u}{2\pi mc}. \tag{2.5}$$

The parameter K is also referred to as the deflection parameter: the maximum angle the electron makes with the longitudinal, or z-axis, is bounded by $\pm K/\gamma$. For $K < 1$, the electron's motion is completely within the radiation cone and leads to interference effects that result in higher spectral brightness, cone narrowing, and partial coherence. For $K \gg 1$ the interference effects are lost but the power radiated is increased by a factor of $2N$, where N is the number of magnet periods. At $K \gg 1$ there is also is a broad shift to higher photon energies. The case of $K \lesssim 1$ is called the undulator limit, and the case of $K \gg 1$ produces 'wiggler' radiation [9].
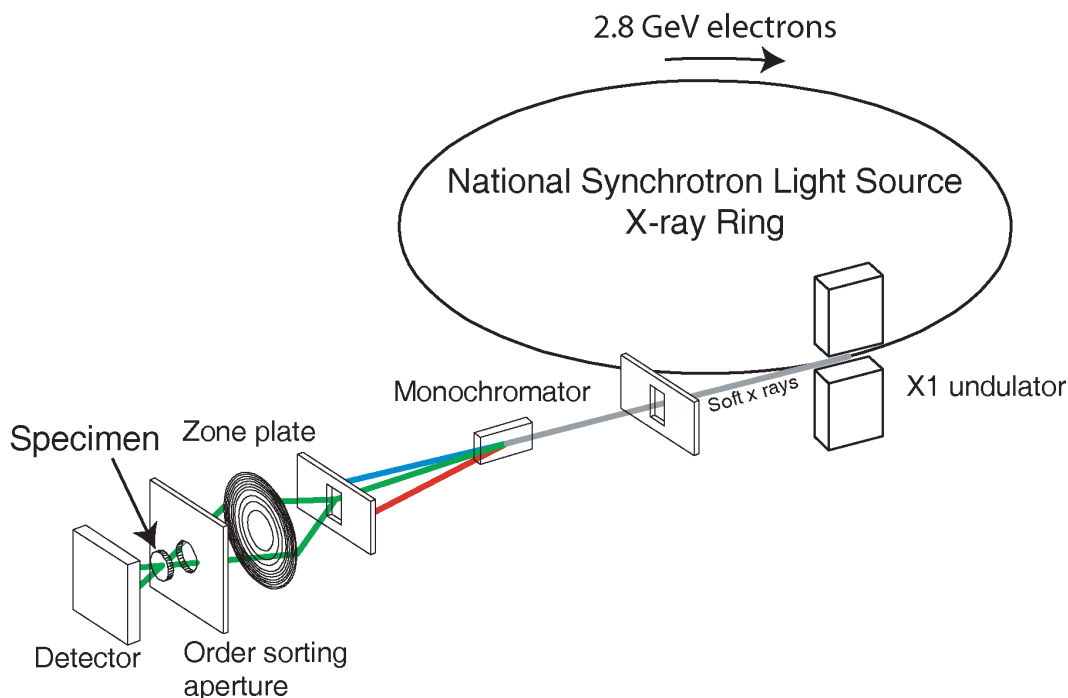
Figure 2.1: NSLS beamline X1 schematic. The coherent x-ray beam provided by the X1 undulator is monochromatized and then focused by the zone plate onto the sample. The sample is raster scanned pixel by pixel through the focal point to obtain an image.

The X1 Undulator

The X1 undulator is shared between beamlines X1A and X1B. The undulator has 35 periods, with a minimum gap of 32 mm. The calculated undulator output is shown in Figure 2.2. Because the undulator is shared among beamlines, the gap setting is chosen to best fit the needs of all endstations. For our work on the carbon and oxygen $1s$ absorption edges, a gap of 36 mm is used. Figure 2.3 is a plot of the undulator output for a gap of 36 mm. The first harmonic peak can be used for carbon $1s$ edge spectroscopy, which is around 288 eV. A typical carbon spectrum will span the energy range from 280 to 310 eV. The second harmonic peak covers the range of the oxygen $1s$ absorption edge spectrum, from 520 to 560 eV.

16
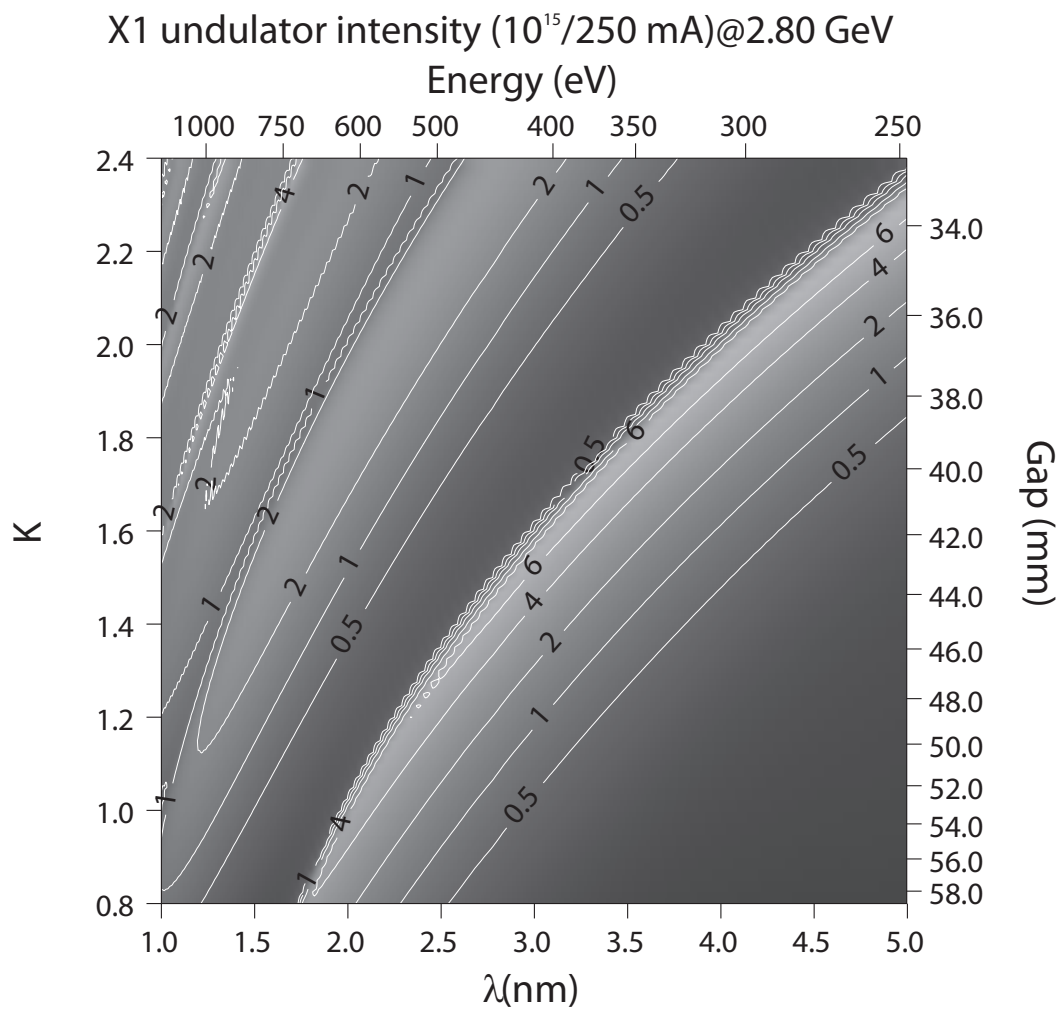
Figure 2.2: Calculated output from the X1 undulator at NSLS. The magnetic strength parameter, K, increases with decreasing gap width.
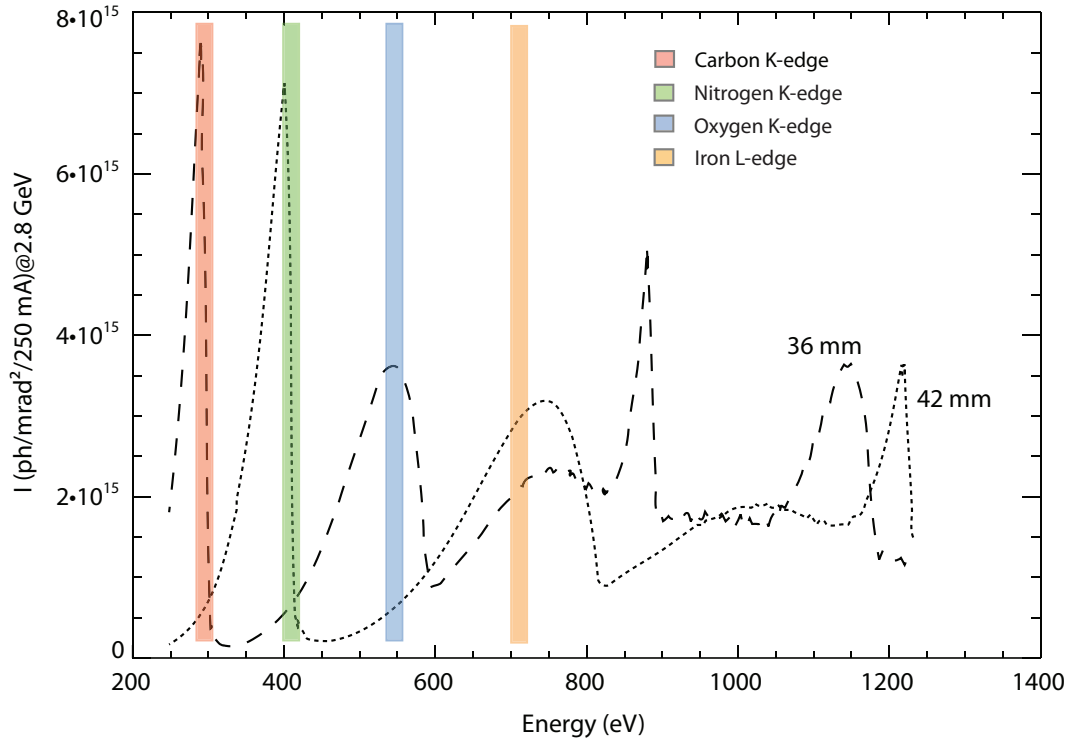
Figure 2.3: Output from the X1 undulator calculated from [10] for the typical gap settings of 36 mm and 42 mm. The 36 mm gap setting is used for the carbon and oxygen $1s$ absorption edges. The carbon $1s$ absorption edge at 288 eV sits at the first harmonic peak and the oxygen $1s$ absorption edge at 544 eV sits at the second harmonic peak of the undulator output. This provides a large intensity beam for imaging at these edges. For imaging at the nitrogen $1s$ absorption edge, which lies at 410 eV, a gap setting of 42 mm is used.

2.1.4 Temporal and Spatial Coherence

The coherence of a field is the degree to which the field correlations are known from one position in space and time to another. To propagate x rays a great distance with little divergence and to focus them to the smallest possible spot size, the phase and amplitude of the field needs to be well-defined across the region of interest.

If the electric field is known at one position in space and time, then the electric field can be predicted at any other point for a coherent field. An example of a completely incoherent field is a large number of atoms moving at random and radiating at various frequencies. In this case there is no relation between one point in the field and another. In practice, a radiation source is neither perfectly coherent or incoherent. For a partially coherent source there is a region in time and space over which the field is coherent.

For temporal coherence, a coherence length can be defined along the direction of propagation of the wave. The coherence length is defined as the distance over which two waves of wavelength difference $\Delta\lambda$ become π radians out of phase. For a source of bandwidth $\Delta\lambda$, the coherence length is defined

$$l_{coh} = \frac{\lambda^2}{2\Delta\lambda}. \tag{2.6}$$

The temporal coherence can be improved by decreasing the bandwidth $\Delta\lambda$ of the source. This is done using a monochromator, as discussed in Section 2.1.4.

Spatial coherence is the phase correlation along the direction perpendicular to the direction of propagation. In the coordinate system of the X1A microscope, it is phase correlation in the x-y plane. An ideal example of spatial coherence is that of spherical waves produced by a point source. Because a real source is not an ideal source, we need to determine what maximum source size will produce a spatially coherent wavefront across the region of interest. Conversely, a source that is smaller than necessary will not improve the coherence in the region of interest. We can start by using Heisenberg's uncertainty principle,

$$\Delta\mathbf{x} \cdot \Delta\mathbf{p} \geq \hbar/2, \tag{2.7}$$

where $\Delta\mathbf{x}$ and $\Delta\mathbf{p}$ are the uncertainties in position and momentum. Then use $d = 2\Delta x$ as the source size that is resolvable with wavelength λ at a beam divergence θ relative to the propagation axis. Photon momentum is $\hbar\mathbf{k}$ and wavenumber $\mathbf{k}$ is $2\pi/\lambda$. If $\Delta\lambda/\lambda$ is small, then the uncertainty in momentum is due to θ. Substituting all these into the above equation we can write the relation

$$d \cdot \theta = \lambda/2\pi. \tag{2.8}$$

This relation determines the smallest source size d that it is possible to discern for a given beam divergence θ and the wavelength of light λ. This means that a source smaller than $\lambda/2\pi\theta$ will not improve the coherence over the region of interest that subtends angle θ, but a source size larger than $\lambda/2\pi\theta$ will decrease the coherence of the wavefront over the region of interest. In other words, this means that as the phase space product, $\rho = d \cdot \theta$ is increased by increasing the source size, the coherence across the angle θ decreases.

Spatial and Spectral Filters for Coherence

The undulator radiation must be filtered to obtain a high degree of spectral and spatial coherence that is required for even illumination of the zone plate (Section 2.2). The filtering is done using a combination of a monochromator and slits. A monochromator is a diffraction grating used in conjunction with entrance and exit slits to select the wavelength λ and reduce the bandwidth $\Delta\lambda$. The light incident on the monochromator grating is deflected into an angle that is dependent on the energy according to the grating equation,

$$m\lambda = d_0(\sin\alpha + \sin\beta), \tag{2.9}$$

where m is the spectral order, d_0 is the grating period, α is the incident beam angle, and β is the diffracted angle of light with wavelength λ. The grating is rotated so that only x rays of wavelength $\lambda \pm \Delta\lambda$ pass through the slit.

At beamline X1A the undulator beam is divided into three beamlines, X1A1, X1A2 and X1B, by toroidal mirrors. On the X1A branches, each toroid focuses horizontally onto the entrance slit of the monochromator and focuses vertically onto the exit slit. The X1A monochromators are identical spherical gratings. The exit slit is positioned at the focal point of the spherical grating. The slit aperture size is motor controlled, and the entrance and exit slits are generally set to the same size aperture. Together they determine the energy resolution of the monochromator. The entrance slit reduces the spread of the beam on the monochromator grating and the exit slit selects the energy width of the beam leaving the grating.

The exit slit then becomes the source for the zone plate optics, and its size is chosen to optimize the coherence and flux of the beam incident on the zone plate using Equation 2.8:

$$d \cdot \theta = \lambda/2\pi.$$

Using the small angle approximation, $\tan\theta \simeq \theta$, we can rewrite the angle $\theta = d_{ZP}/z$ where z is the distance from the exit slit to the zone plate and d_{ZP} is the radius of the zone plate. The phase space product ρ can be rewritten in

terms of these beamline parameters as

$$\rho = d_{slit} \cdot (d_{ZP}/z) \, . \tag{2.10}$$

As d_{slit} increases to allow for more photons, the coherence of the wavefront across the diameter of the zone plate decreases [11].

Order Sorting Mirrors

The monochromator grating deflects wavelength λ into an angle β, but also deflects light of wavelength $n\lambda$, where n is any integer, into that same angle β. These higher orders would result in unwanted background signal. In some cases a higher order of light would coincide with the absorption edge of another element. To filter out these higher orders, mirrors are placed in the beam at a grazing incidence. The reflectivity of these mirrors depends on both incidence angle and wavelength. The wavelength dependence of the refractive index will be discussed in Section 3.1.1. Figure 2.4 shows the reflectivities of quartz (SiO_2) and nickel for several different incidence angles. For quartz, the reflectivity drops to zero at about 540 eV, which corresponds to the K absorption edge of oxygen. At an angle of $4°$ the reflectivity remains small for higher energies. A quartz mirror is used for imaging at the carbon edge (280-310 eV) because it will reflect 60% of the light in that energy range but will absorb the higher orders above 540 eV. Quartz mirrors would not be a good choice for imaging at the oxygen edge, and so nickel mirrors are used.

2.2 Zone Plate Optics

A Fresnel zone plate is a circular diffraction grating consisting of concentric rings of alternating opaque and translucent material with radii given by

$$r_n^2 = nf\lambda + \frac{n^2\lambda^2}{4}, \tag{2.11}$$

where n is the zone number, λ is the wavelength, and f is the first-order focal length. If one considers a spherical wavefront as being divided into zones whose radii differ by $\lambda/2$, then radiation from adjacent zones have opposite phases. If alternating zones are blocked, light with the same phase constructively interferes. The zone width decreases radially, causing the path length to the focal spot from adjacent pairs of zones to differ by λ.

The transverse resolution, or focal spot size, is determined by the width of the outermost zone, $\Delta r_N \equiv r_N - r_{N-1}$. Three parameters fully specify the
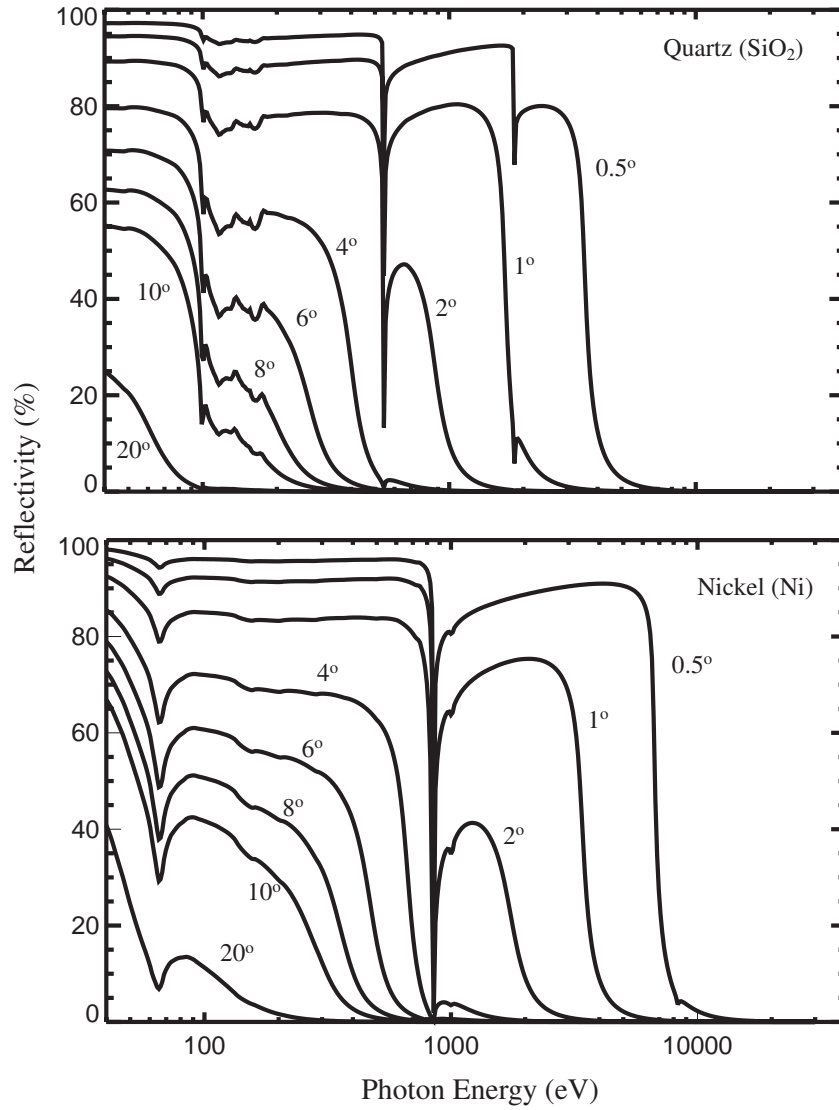
Figure 2.4: Grazing incidence reflectivities for quartz and nickel mirrors [12]. The reflectivity of quartz drops above 540 eV for an incident angle of 4°, making it a good mirror choice for absorbing higher orders from the monochromator when doing carbon edge (280-310 eV) spectroscopy. Similarly, a nickel-coated mirror could be used for spectroscopy at the oxygen edge while absorbing orders above 850 eV.

zone plate, such as the number of zones N, wavelength λ and outermost zone width Δr. Other parameters can be written in terms of these, such as the diameter of the zone plate,

$$D = 4N\Delta r, \tag{2.12}$$

the focal length,

$$f = \frac{4N\left(\Delta r\right)^2}{\lambda}, \tag{2.13}$$

and the numerical aperture,

$$\mathrm{NA} = \frac{\lambda}{2\Delta r}. \tag{2.14}$$

The dependence of f on λ makes the zone plate chromatic, and so it must be illuminated by monochromatic light. To avoid chromatic blurring, the number of zones must be less than the monochromaticity,

$$N < \frac{\lambda}{\Delta\lambda}. \tag{2.15}$$

The zone plate has higher order foci as well, and so an order-sorting aperture (OSA) is used to block higher orders. See Figure 2.5. The OSA is a circular aperture with diameter equal to the diameter of the zone plate central stop.

A typical zone plate used at X1A has a diameter of 160 μm and an outermost zone width of 30 nm. The thickness of the zone plate is about 200 nm [13].

2.3 Scanning Microscope Systems

To acquire spectromicroscopy data, the sample is raster scanned through the focus of the zone plate to collect a 2D image, and this process is repeated over many energies across an absorption edge to get an x-ray absorption near-edge spectrum (XANES) at every point in the sample. The pixel-by-pixel scanning is done by X and Y stepper motors with 1 μm resolution, and by an X-Y piezo scanning stage with nanometer resolution. Because the focal length of the zone plate depends on wavelength, the sample must also be moved in relation to the zone plate using a stepper motor to maintain focus.

The OSA position must also be changed as the focal length changes. A stepper motor moves the OSA along the z-axis automatically as the energy is scanned.

To compensate for hysteresis and other nonlinearities in the piezo positioners, a capacitance micrometer feedback system is used. The piezo stage
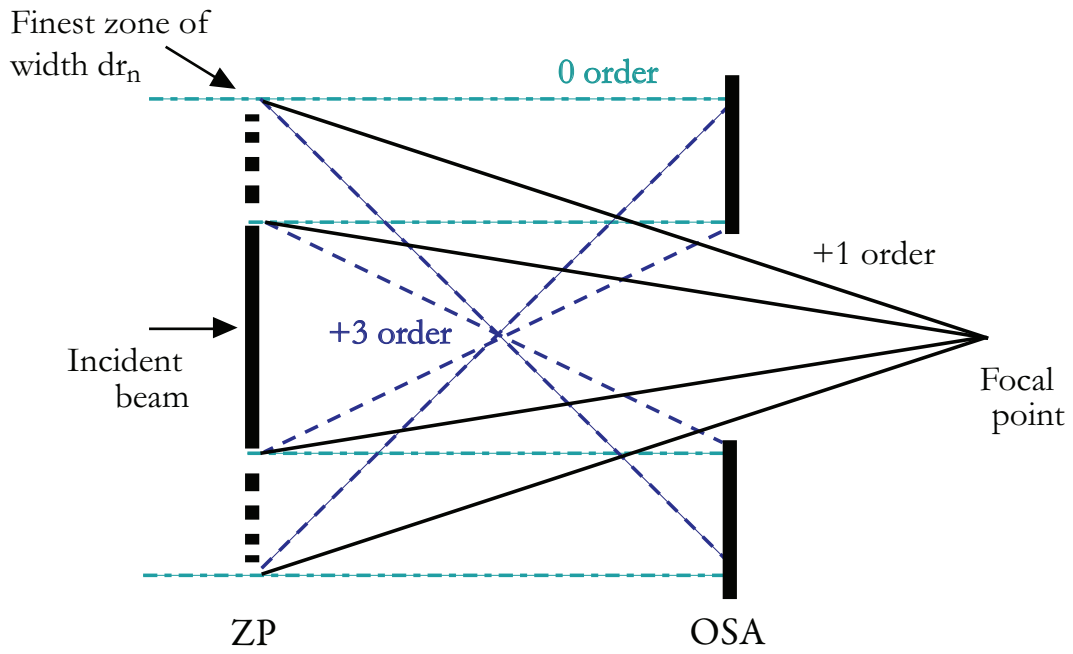
Figure 2.5: Side view schematic of zone plate and order-sorting aperture (OSA). The OSA is a pinhole of the same diameter as the zone plate central stop, and is used to block zero-order radiation and also higher-order foci from the zone plate.

is a finely machined from a single piece of aluminum or stainless steel with flexures allowing movement in the x-y plane. The position of the piezo stage is measured relative to its own frame and this position is used in a closed loop to maintain the desired position.

While the capacitance micrometer feedback loop checks that the piezo motor actually moved to the desired position, as measured relative to its own frame, there are motions between the sample holder and zone plate that need to be corrected. As the z-position of the sample follows the changing z-position of the focal point, wobbles in the Z-stage motion and thermal drifts cause drifts in X and Y. Changes in X and Y cause changes in the field of view between images. In extreme cases the sample can be completely lost from the field of view during the course of a many-hour scan. Defocusing of the sample can also occur due to thermal drifts in the relative Z position of the zone plate and sample. To correct for this, a laser interferometer system was included in the STXM V upgrade [14, 15]. The interferometer provides high precision information on the relative position between sample and zone plate. This information can be used as feedback to motors in keeping the sample in focus and within the field of view.

2.4 Dark Field Microscopy

While x-ray microscopes can image unstained specimens with high contrast, it is often useful to label molecules within the specimen. In visible light microscopy fluorescent dyes are often used to label specific proteins within a cell, and for electron microscopy gold labels are used. Fluorescence techniques can be used in an x-ray microscope in much the same way as in visible light microscopy, by using the x-ray beam to excite the fluorescent labels. The emitted fluorescence can be detected by a detector placed at an angle from the upstream side of the sample while the x rays pass through the sample. Another labeling technique is to use small gold spheres as biological labels which can be detected with dark field imaging in the STXM. The gold spheres can be designed with protein chains that will selectively attach to the biological structure of interest.

Dark field imaging of gold spheres relies on the fact that the scattering strength of biological structures is small compared to that of gold labels. The gold spheres are small point-like objects that will scatter photons out of the light cone produced by the zone plate. If the straight-through beam is blocked so that only the scattered photons are detected, then only the gold labels will be imaged as bright spots in a dark background. Though the total number scattered photons is small, the contrast is high, as the large background signal

from the transmitted beam is eliminated.

The dark field signal depends on both the absorption and phase of the sample, and so is not linearly related to the transmitted intensity. A high-resolution image of a complex specimen is difficult to interpret. Dark field imaging is best suited to small strongly scattering isolated objects. For a cell labeled with gold nanoparticles, the cell itself can be imaged using absorption contrast and the gold labels can be detected from their dark field signal [16, 17].

In Section 2.4.1 we will cover the characteristics of dark field imaging and look at the effects of detector and objective configurations on contrast and resolution. In the following Section 2.4.2 we will look at examples of dark field imaging at X1A.

2.4.1   Dark Field Image Formation

The formation of an image in STXM can be described by a set of equations as described in [18]. A diagram labeling the positions of each of the elements in the calculation is shown in Figure 2.6. The coherent monochromatic beam is focused onto the sample by a Fresnel zone plate objective. In dark field imaging the dark field stop blocks the straight-through beam and the scattered signal is detected by an area-integrating detector.

In the following we will refer to spatial frequencies f which are wavelength-scaled diffraction angles $f = \theta/\lambda$, and which correspond to diffraction of light at normal incidence to a grating with period d according to $f = 1/d$. For brightfield incoherent imaging with a zone plate of finest zone width dr_N, the bright field cone extends out to a maximum spatial frequency of $f = 1/(2dr_N)$ while the modulation transfer function, measuring the optical response as a function of spatial frequency, extends out to a maximum frequency of $f = 1/dr_N$.

Signal to Noise Ratio and Contrast

The signal to noise ratio (SNR) is a commonly used measure to determine the integrity of the image. If p_1 is the fraction of the illumination intensity at the image location corresponding to the center of a protein rod, and p_2 represents the intensity at the image center (between the two rods), then the SNR can be written [19]

$$\text{SNR} = \frac{|np_1 - np_2|}{\sqrt{np_1 + np_2}} \tag{2.16}$$

where n is the number of photons incident on each point in the object plane. The signal is the difference in intensity between object and no object. The
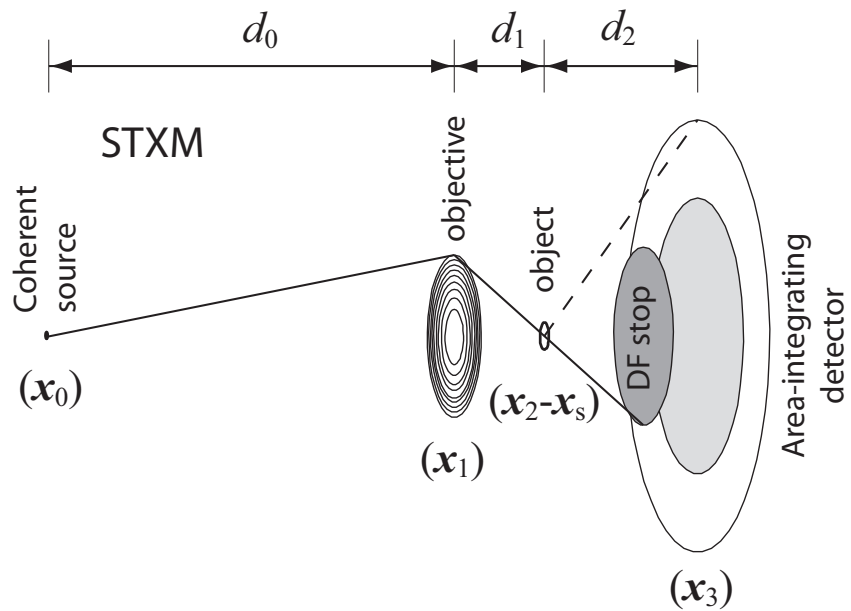
Figure 2.6: Schematic representation of dark field imaging in STXM, from [18]. The illumination rays are shown in solid lines and the scattered beam is shown as a dotted line. The objective lens is a Fresnel zone plate with focal length f_0 and pupil function $P_0(\mathbf{x}_1)$. The unscattered light from the zone plate is intercepted by the dark field stop. The light scattered from the object is collected by an area-integrating detector.

noise is the square root of the total number of photons incident on the object. The SNR can be rewritten as

$$\text{SNR} = \sqrt{n}\frac{|p_1 - p_2|}{\sqrt{p_1 + p_2}} = \sqrt{n}\Theta \qquad (2.17)$$

where we have defined a contrast parameter, Θ. The contrast gives us a parameter with which to determine how well the object is distinguishable from the background.

Dark Field Stop

The dark field stop blocks the unscattered beam from striking the detector so that only the photons scattered by the sample are detected. First we'll look at the effect of the shape of the dark field stop on the image contrast. A large area detector with sensitivity out to spatial frequencies of $1/(2 \cdot 1 \text{ nm})$ was used in conjunction with three different types of dark field stop, shown schematically in Figure 2.7. The first is a bar-shaped stop oriented parallel to the two object rods. The second is a solid disk that must be aligned in two directions perpendicular to the beam and also must be located at the proper distance from the object plane. The third is an annular stop that gives sensitivity to the 'shadow' of the zone plate's central stop.

The image intensity is plotted for each of these three configurations in Figure 2.7 with varying object separation. In the first two plots, corresponding to the bar-shaped and solid disk stops, the objects are distinguishable at an object separation as small as 20 nm. But the annular stop has slightly worse results, despite the fact that it allows for the collection of more scattered light. This can be explained by the fact that the inner part of the detector is a point-like aperture and so contributes to the bright field image. Because we measure the transmitted beam, the bright field signal is actually the absence of photons. The dark field signal is then the presence of scattered photons. Because these two mechanism are opposites, the added signal from the center of the detector in fact acts to reduce the contrast of the dark field signal.

Detector Aperture

In the results discussed above, the detector was assumed to be very large. A very large detector will increase the number of photons collected, but as we learned from the example of the annular dark field stop, higher detection sensitivity does not necessarily lead to better contrast in the dark field image. So what happens when the detector aperture is reduced? Figure 2.8 shows
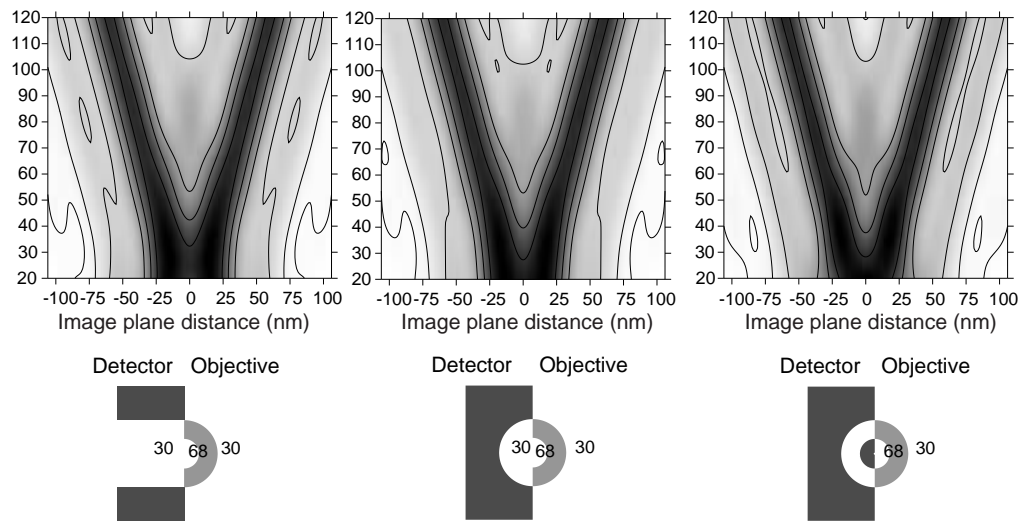
Figure 2.7: Dark field image intensities for three dark field stop geometries. Two cylinders of 20 nm protein and 20 nm gold are imaged using three different dark field stop geometries. The first is a bar-shaped stop aligned parallel to the object cylinders. The second is a solid disk stop, and the third is an annular stop that allows photon collection in the shadow of the zone plate's central stop. Both the bar-shaped and the solid disk stops can resolve closely-spaced cylinders, but the annular stop shows a decline in the resolution of the two objects.

the difference between the large area detector and a small detector. In both cases a solid disk dark field stop was used. The smaller detector has an angular acceptance of $1/(2 \cdot 20 \text{ nm})$ which corresponds to 1.5 times the numerical aperture of the zone plate. From Figure 2.8 it is clear that the smaller detector gives better results for small object separations. In practice it is important to note that closing down the acceptance angle also reduces the total signal. This decrease in signal will make background signals from poor alignment and imperfect zone plates more pronounced.

The improvement in contrast seen with smaller acceptance angles can be described partly by considering double-slit interference patterns. The larger acceptance angle allows the detector to integrate over both constructive and destructive components, and so reduces the contrast between the two objects. When the acceptance angle is reduced, integration is only over the constructive interference fringes. This explanation suggests that there is an ideal detector acceptance angle for dark field imaging that can be calculated. Figure 2.9 shows the image intensities for a fixed object separation of 24 nm while varying the acceptance angle of the detector. The detector acceptance angle is written in terms of an equivalent zone width. For very large and very small acceptance angles the resolution is poor. The objects were best resolved when the acceptance angle of the detector was between $1/(2 \cdot 20 \text{ nm})$ and $1/(2 \cdot 15 \text{ nm})$, which corresponds to a numerical aperture of 1.5-2.0 times that of the objective zone plate.

Because the purpose of using dark field imaging would be to distinguish labeled structures from unlabeled structures, we want a dark field signal only when gold labels are present. Figure 2.10, taken from [18] shows image intensities for labeled and unlabeled protein. For this calculation a detector acceptance angle of 1.5 times the objective numerical aperture and a solid disk stop were used. The relative intensity of two cylinders that are labeled versus those that are unlabeled are plotted in Figure 2.10 with varying object separation. The plot shows that the labeled structures can be distinguished from the unlabeled proteins by setting an intensity threshold.

2.4.2 Dark Field Imaging at X1A

Soft x rays are an ideal probe for biological specimens due to the high absorption contrast in the region between the carbon and oxygen absorption edges. Dark field imaging in the x-ray microscope is a complimentary tool that can be used to image labeled biological specimens. Labels are used to target specific proteins in a biological specimen to identify specific structures or processes within the cell. If the labels are made of a strongly scattering material, such as gold, they can be imaged in the dark field imaging mode in STXM. In this
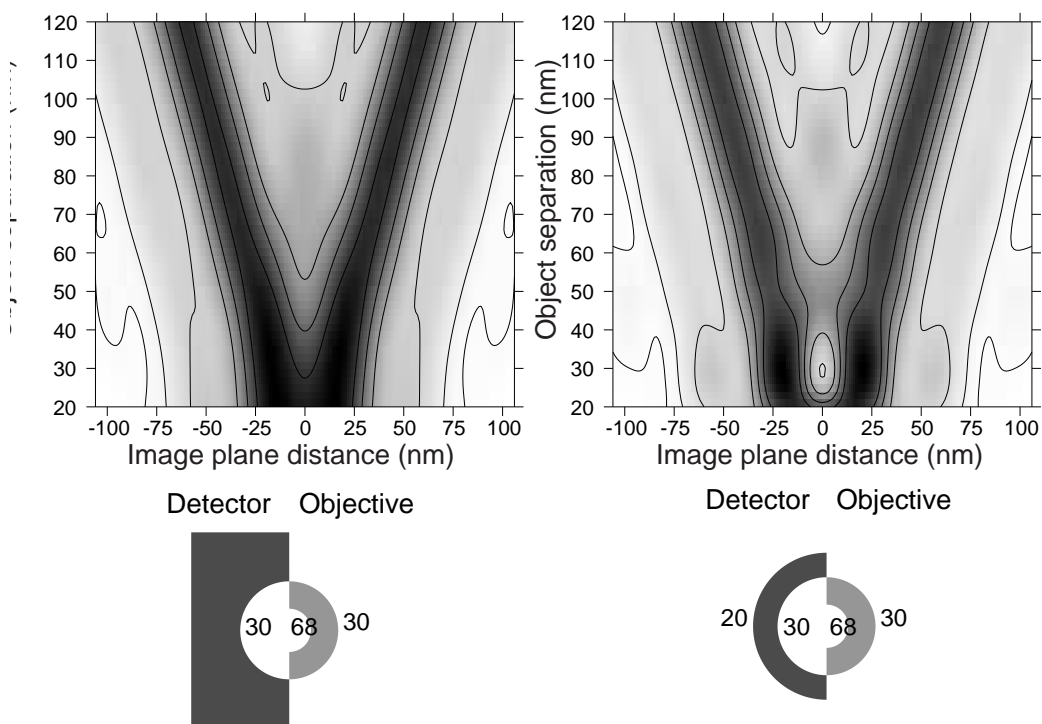
Figure 2.8: Figure from [18] of dark field image intensities for two different detector acceptance angles. Two cylinders of 20 nm protein and 20 nm gold are varied in separation distance. High intensity is shown as darker regions. On the right, the small detector acceptance angle leads to an increase in resolution over the large acceptance angle detector on the left. The contrast between the object cylinder and the space between the cylinders is greater for the detector with smaller acceptance angle [18].
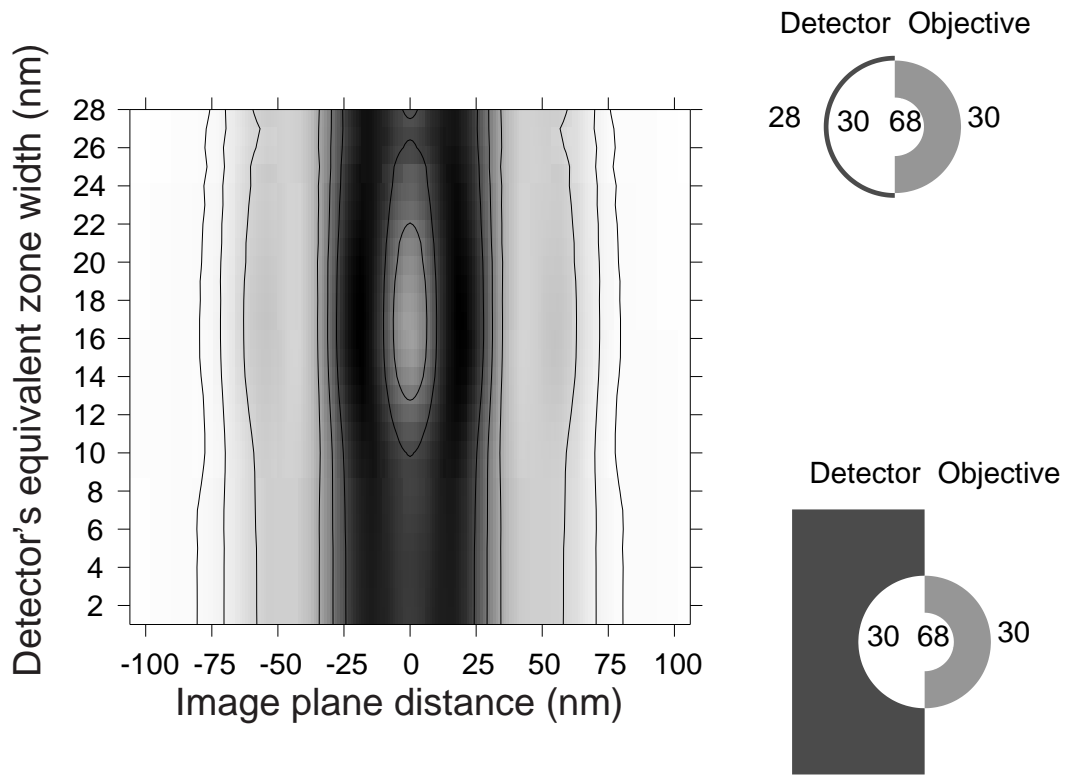
Figure 2.9: Figure taken from [18]. Two 20 nm diameter protein rods are assumed to have center-to-center separation of 24 nm. The detector acceptance angle is given in units of the equivalent outermost zone width if a condenser zone plate had been used, and was varied between 2 and 28. The objects were most clearly separated with a detector aperture of $1/(2{\cdot}20$ nm) to $1/(2{\cdot}15$ nm) is used. This corresponds to 1.5-2.0 times the maximum aperture of the $\delta_{r_N} = 30$ nm objective zone plate [18].
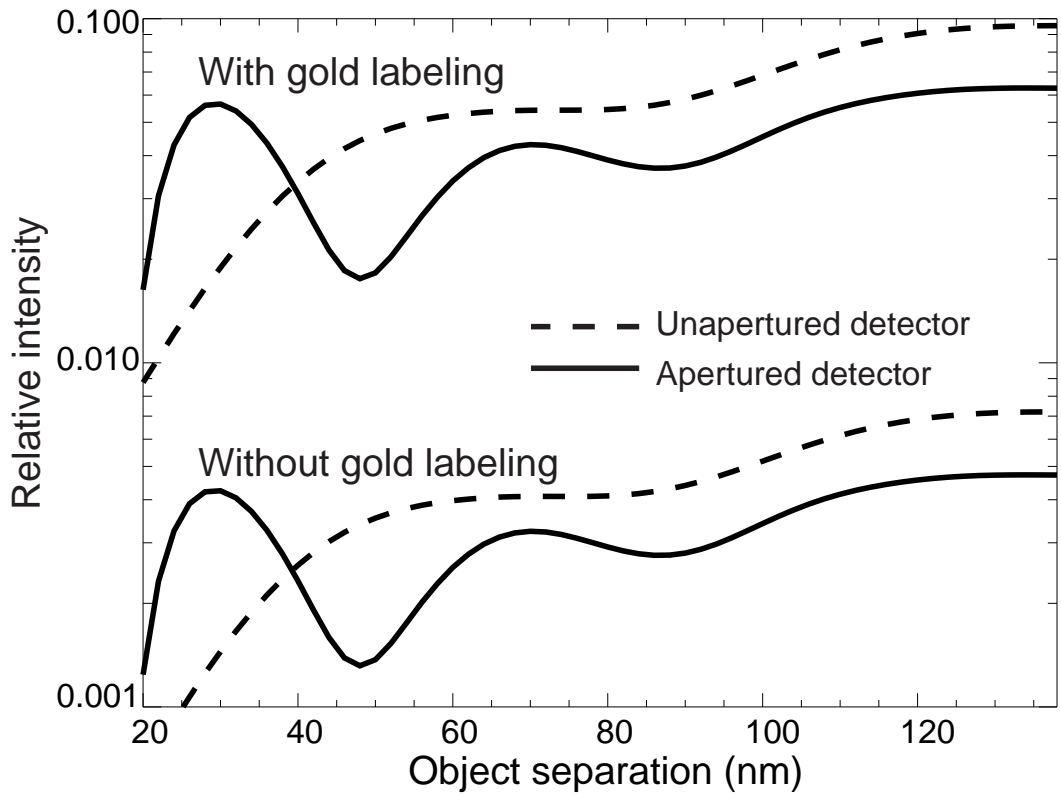
Figure 2.10: Image intensities for labeled and unlabeled protein, taken from [18]. The relative intensity of two cylinders that are labeled (top) versus those that are unlabeled (bottom) are plotted here with varying object separation. This shows that the labeled structures are clearly distinguishable from the unlabeled proteins by setting an intensity threshold. A detector acceptance angle of 1.5 times the objective numerical aperture and a solid disk stop were used.

section we'll discuss dark field imaging done at the X1A STXM.

Alignment of the Segmented Detector

The segmented detector used on beamline X1A2 can be used to simultaneously record bright and dark field images of the sample. The eighth segment of the detector is an annulus with inner diameter 600 μm and outer diameter 1200 μm. The light cone from the zone plate must be aligned with the inner bright field segments. The signal on the dark field segment from the straight-through beam must be minimized or else the dark field signal will be overwhelmed.

The silicon detector is sensitive to visible light, so the chamber must be made sealed from any outside light by covering the viewports with aluminum foil and covering the plexiglass chamber cover with a rubber cover and several layers of black fabric.

The detector is supported by motorized stages that can be moved in x, y and z. The detector must be aligned so that none of the unscattered light from the zone plate falls onto the eighth dark field segment of the detector. The detector can be moved upstream, toward the sample and zone plate, to reduce the acceptance angle of the detector and therefore reduce the size of the light cone on the detector. A 10 μm pinhole is inserted as the sample and a large area scan of the pinhole is made using the stepper motors, for example 400 by 400 μm. The resulting image is a map of the intensity on the detector segments. Then the detector is moved in the x-y plane to reduce the photons on the eighth segment. The pinhole is scanned again to judge the success of the detector move. This process is repeated until there are very few counts on the dark field segment.

2.4.3   Imaging Gold Nanoparticles

Gold nanoparticles are ideal dark field objects, as they are small and highly scattering. Gold nanoparticles of various sizes were produced at the Center for Functional Nanomaterials at BNL. The nanoparticles have a citric acid cap and are suspended in water. A small drop is placed on a silicon nitride window and allowed to air dry. We found that the nanoparticles tend to aggregate during the drying process. Because of large size of the clumps, the nanoparticles are also clearly visible in the bright field images as seen in Figures 2.11 and 2.12.

In Figure 2.11 the pixel size is 1 μm. This pixel size is the stepping motor step size, not the size of focal spot on the sample. Therefore we are still sensitive to the detection of the 44 nm gold spheres, and large area scans can be used to identify regions of interest in the sample.

Bright field absorption imaging can be used to image the non-scattering cell. The dark field image can be superimposed in false color on the bright field image in order to see the spatial distribution of the labels within the cell. This superposition of data sets is easily accomplished using the segmented detector on the X1A2 microscope because both the bright field and dark field data is collected simultaneously.

2.4.4   Imaging Nickel Precipitates

We know from electron microscopy studies that nickel precipitates are formed by the interaction with a living bacterial cell of a *Clostridium* species CH34. This species and its importance to environmental science will be discussed in more detail in Chapter 4. The nickel precipitates will scatter strongly, so dark field imaging is an ideal probe for first identifying the presence of the precipitates and then determining their distribution in relation to the cell. In this section we will discuss the method of collecting dark field images of these samples.

Simultaneous bright and dark field images were collected over the O1s absorption edge, 520-560 eV. The careful alignment of the detector with the x-ray beam was lost after the first fifty images were collected, as the cells show up as shadowy figures in what should be a dark field image. The misalignment of the detector causes the bright field signal from the straight-through beam to strike the dark field segment of the detector, swamping the much weaker dark field signal. This misalignment is most likely due to a drift in the relative position of the detector and zone plate stages.

Figures 2.13 and 2.14 show two samples of the *Clostridium* species CH34, known for its ability to withstand amounts of nickel in its environment that would be fatal to most organisms [20]. The first sample (a) was grown in the presence of nickel chloride. The second sample (b) was grown in regular growth medium, rinsed, and then nickel chloride was added. In this way we wished to identify differences in the active versus passive interactions with the bacteria.

The dark field image in Figure 2.13 shows a sliver of bright pixels to indicate the presence of a strongly scattering object. The histogram of the flux through each pixel in the dark field image was used to select only the highest flux pixels in the image. Figure 2.14 shows dark field and bright field images of the *Clostridium* sp. sample with nickel added later. The dark field image does indicate the presence of nickel precipitates, and the histogram used to select the dark field signal is shown in (e). The bright field image (c) shows a wide margin of exopolysaccharides (EPS) surrounding the cells, but the nickel is not visible. The dark field pixels superimposed on the bright field image (d)
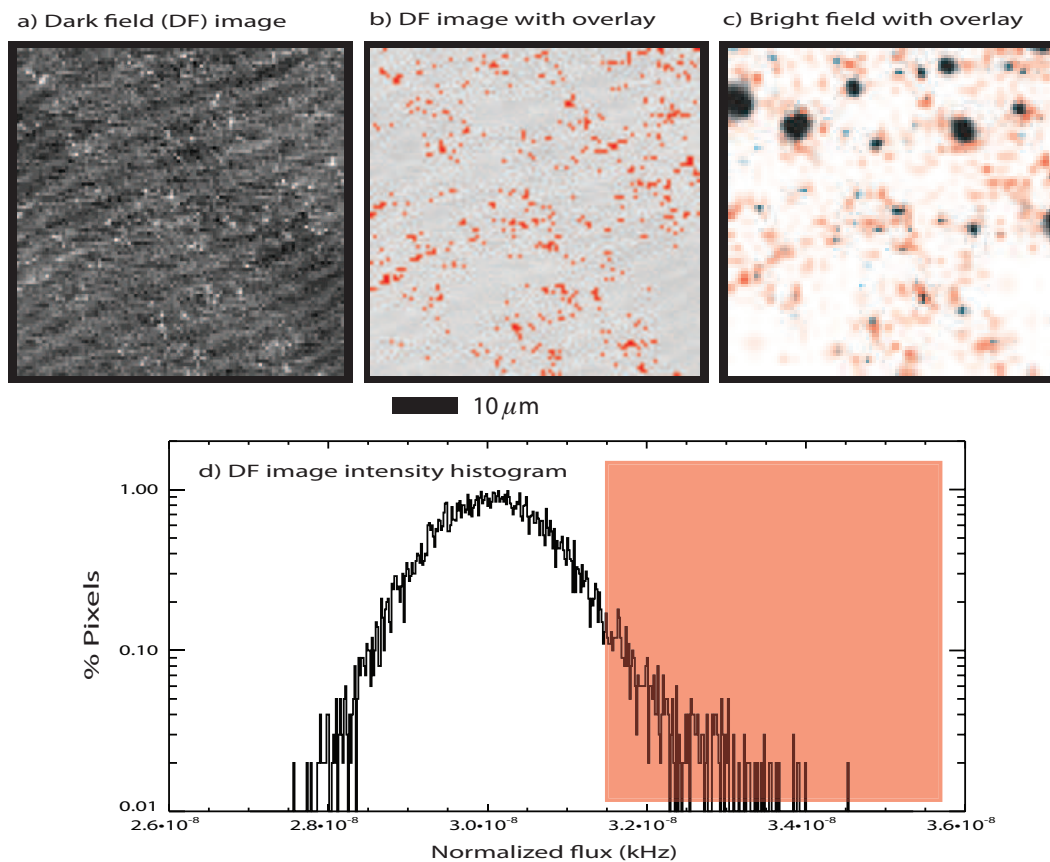
Figure 2.11: A large area scan of 44 nm gold nanoparticles. The step size is 1 μm but the focal point size remains the same. A large area dark field scan like this can be used to identify a region of interest.

a) Dark field image

e) Histogram of dark field image

10 μm

b) Bright field image

c) Dark field with threshold

d) Bright field with dark field pixels
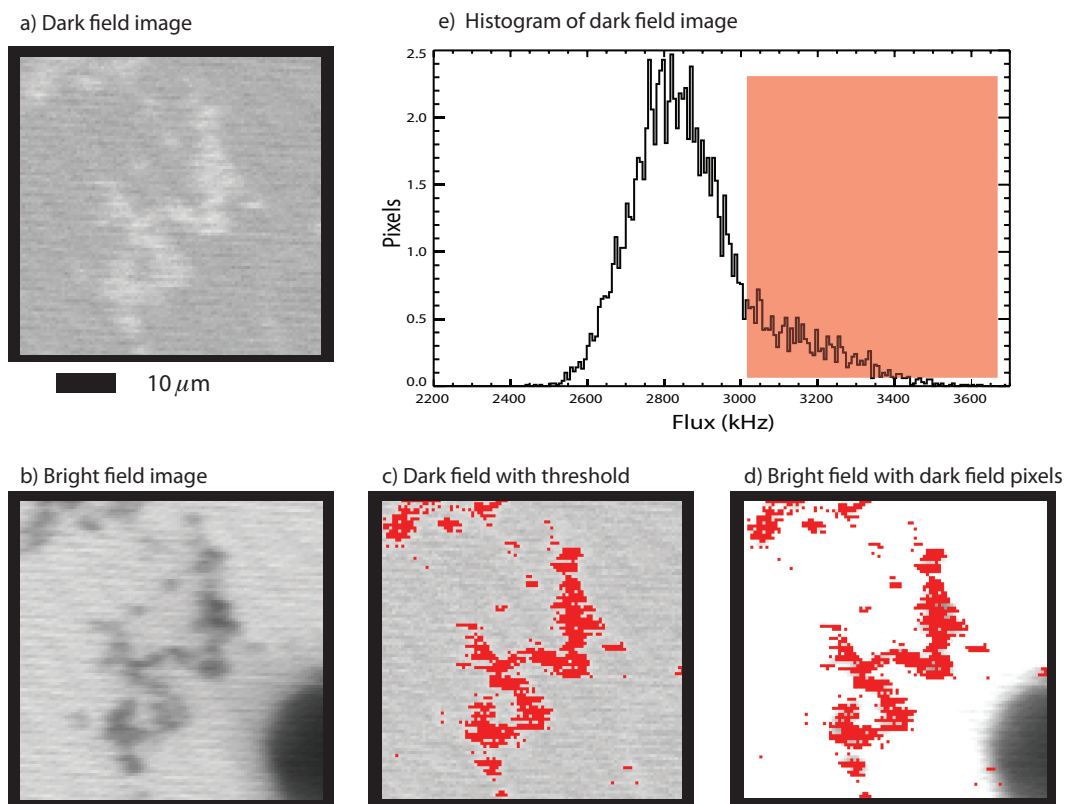
Figure 2.12: Dark field and bright field images of 44 nm gold nanoparticles. a) Dark field image of 44 nm gold nanoparticles. b) Bright field image collected simultaneously. c) Dark field image with high intensity pixels superimposed in red. d) Bright field image with dark field pixels superimposed in red. e) Histogram of dark field image pixels intensities. A threshold intensity was chosen at the red line to select only those pixels which correspond to a strong dark field signal. Those pixels which fall above the threshold intensity are shown in red in Figures b) and c).

37

shows that the nickel is closely associated with the cell and embedded in the EPS.

Dark field x-ray microscopy is a convenient tool that can be used to identify the presence of and map the distribution of small strongly scattering objects in a biological sample. It would be particularly useful for use with gold-labeled biological samples. Careful alignment of the detector and zone plate are required to obtain a good dark field signal, and frequent realignment may be necessary.
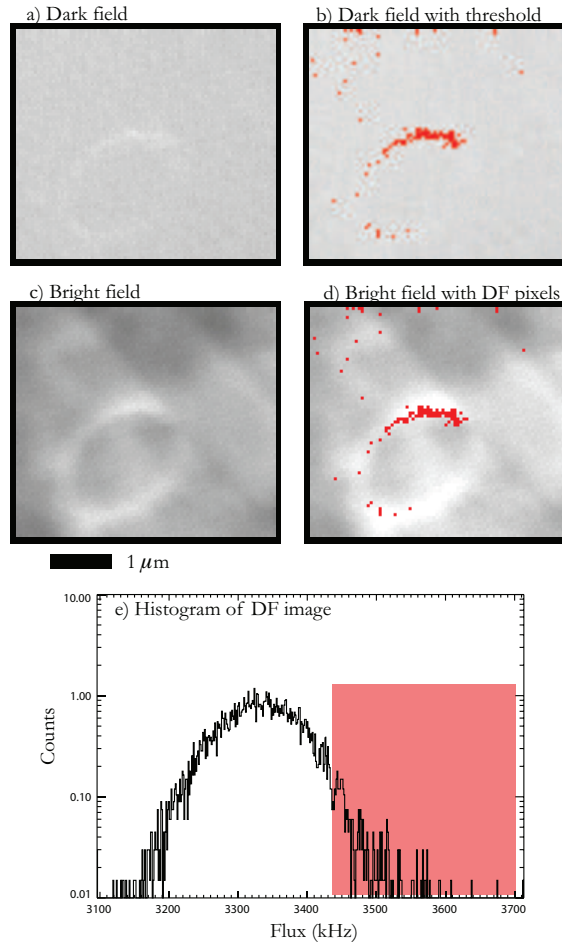
Figure 2.13: Dark field and bright field images of CH34 *Clostridium* bacteria [20] grown in the presence of nickel. a) Dark field image of CH34 grown in the presence of nickel chloride. b) Dark field image with overlay of pixels which lie above the flux threshold, as chosen using the histogram in (e). c) The bright field image does not indicate the presence of nickel precipitates. d) Bright field image with dark field pixels superimposed. This indicates that there most likely are nickel precipitates present, and they tend to be closely associated with the cell.
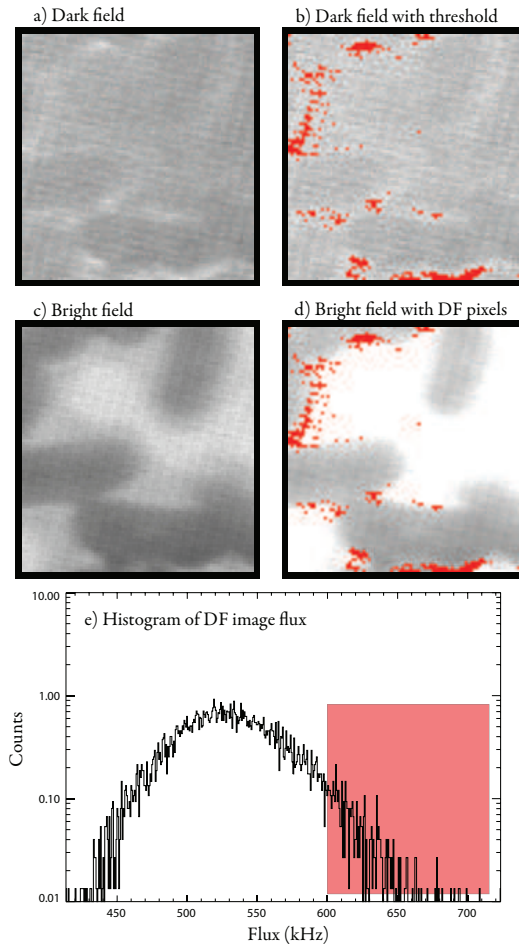
Figure 2.14: Dark field and bright field images of CH34 *Clostridium* bacteria [20] with nickel added. a) Dark field image of CH34 with nickel added. b) The dark field image with overlay of pixels which lie above the flux threshold suggests that the nickel does form precipitates when in contact with the bacteria. c) The bright field image shows a wide margin of exopolysaccharides surrounding the cell, and the superimposed dark field pixels in (d) indicate that the precipitates tend to clump in the exopolysaccharides surrounding the cell. e) Histogram of pixel flux in dark field image.

Chapter 3

Spectromicroscopy Analysis

3.1 The Refractive Index

3.1.1 Damped, Driven Harmonic Oscillator Model

In this section we will derive an expression for the complex index of refraction of a nonconducting medium using the atomic model of a damped, driven harmonic oscillator. In the medium the electrons are bound to the nucleus and can oscillate like a mass on a spring. We can treat the nucleus as stationary because of its large mass compared to that of the electrons. The binding force for a mass on a spring is

$$F_{\text{binding}} = -k_{\text{spring}}x = -m\omega_0^2 x, \tag{3.1}$$

where m is the electron's mass and $\omega_0 = \sqrt{k_{\text{spring}}/m}$ is the natural oscillation frequency.

An incident electromagnetic wave of frequency ω provides a driving force to the electron of

$$F_{\text{driving}} = qE = qE_0 e^{i\omega t}. \tag{3.2}$$

Because the electron is oscillating, it must radiate power as $\dddot{v} = \partial^3 x/\partial t^3$, as given by the Abraham-Lorentz formula [8]. To find an expression for $\dddot{v}$, we can apply an electric field of $\text{Re}[E_0 e^{i\omega t}]$, and then the displacement and its

derivatives can be written as the following:

$$
\begin{aligned}
x &\propto \cos\omega t \\
v = \dot{x} &\propto -\omega\sin\omega t \\
\dot{v} = \ddot{x} &\propto -\omega^2\cos\omega t \\
\dddot{x} &\propto \omega^3\sin\omega t = -\omega^2\dot{x}.
\end{aligned}
$$

This allows us to write the radiation damping force $F_{\text{radiation}} \propto \dddot{x} \propto \omega^2\dot{x}$ as

$$
F_{\text{damping}} = -m_e\gamma\dot{x}, \tag{3.3}
$$

where γ is a damping coefficient that will depend on ω. According to Newton's second law, the sum of the forces will give us the acceleration of the electron, or

$$
\begin{aligned}
m_e\ddot{x} = F_{\text{tot}} &= F_{\text{binding}} + F_{\text{damping}} + F_{\text{driving}} \tag{3.4}\\
&= -m\omega_0^2 x - m_e\gamma\dot{x} + qE_0 e^{i\omega t}. \tag{3.5}
\end{aligned}
$$

$$
\tag{3.6}
$$

The electron oscillates at the driving frequency,

$$
x(t) = x_0 e^{i\omega t}, \tag{3.7}
$$

and using this to solve Equation 3.1.1, the oscillation amplitude as a function of frequency can be found to be

$$
x(\omega) = \frac{q/m_e}{(\omega_0^2 - \omega^2) + i\gamma\omega}\text{Re}[E_0 e^{i\omega t}]. \tag{3.8}
$$

Because the driving force from the incident wave displaces the electron from the nucleus, the atom has a dipole moment of

$$
p(t) = qx(t) = \frac{q^2/m_e}{(\omega_0^2 - \omega^2) + i\gamma\omega}\text{Re}[E_0 e^{i\omega t}]. \tag{3.9}
$$

This is the dipole moment associated with a single oscillator. In a material there will be n_a atoms per volume, each with Z electrons. Each electron may have more than one resonant frequency, so that the number of oscillators, j, may be greater than Z. Every oscillator has a resonant frequency, ω_j, damping coefficient γ_j and strength g_j such that $\sum_j g_j/(4\pi\epsilon_0) = Z$. At driving frequen-

cies above all resonances, we have $n_a \sum_j g_j$ oscillators per volume. Then the volume polarization is

$$P = \frac{n_a e^2}{m_e} \left(\sum_j \frac{g_j}{(\omega_j^2 - \omega^2) + i\gamma\omega} \right) \mathrm{Re}[E_0 e^{i\omega t}]. \qquad (3.10)$$

The electric susceptibility, defined as $\chi_e \equiv P/(\epsilon_0 E)$, is a measure of how easily the material polarizes in the presence of the electric field. Using the equation for P above, χ_e can be written as

$$\chi_e = \frac{n_a e^2}{m_e} \sum_j \frac{g_j}{(\omega_j^2 - \omega^2) + i\gamma\omega}. \qquad (3.11)$$

For nonconducting, electrostatically neutral, linear media the wave equation is

$$\nabla^2 \boldsymbol{E} = \mu\epsilon \frac{\partial^2 \boldsymbol{E}}{\partial t^2}, \qquad (3.12)$$

where μ and ϵ are the permeability and permittivity of the medium, respectively. There is a plane wave solution,

$$E = \mathrm{Re}[E_0 e^{-i(kr - \omega t)}]. \qquad (3.13)$$

If we insert the plane wave solution into the wave equation, we get the relation

$$k^2 = \mu\epsilon\omega^2. \qquad (3.14)$$

If we define the index of refraction n to be the ratio of the wave vector in the medium to that in vacuum, we have

$$n \equiv \frac{k}{k_0} = \frac{\sqrt{\mu\epsilon}\omega}{\sqrt{\mu_0\epsilon_0}\omega} = \sqrt{(1 + \chi_m)(1 + \chi_e)} \qquad (3.15)$$

where we have used $\epsilon = \epsilon_0(1 + \chi_e)$ and $\mu = \mu_0(1 + \chi_m)$. Many materials have a small magnetic susceptibility compared to the electric susceptibility, and furthermore we often have $\chi_e \ll 1$, so we can approximate $n \simeq 1 + \frac{1}{2}\chi_e$, giving

$$\begin{aligned} n &= 1 + \frac{n_a e^2}{2m_e\epsilon_0} \sum_j \frac{g_j}{(\omega_j^2 - \omega^2) + i\gamma_j\omega} \\ &= 1 - \frac{n_a e^2}{2m_e\epsilon_0} \sum_j \frac{g_j}{(\omega_j^2 - \omega^2)^2 + \gamma_j^2\omega^2} \left[(\omega^2 - \omega_j^2) + i\gamma_j\omega \right], \quad (3.16) \end{aligned}$$

where the top and bottom have been multiplied by the complex conjugate, $[(\omega_j^2 - \omega^2) - i\gamma_j\omega]$. We can separate this into real and imaginary parts:

$$\text{Re}[n] = 1 - \frac{n_a e^2}{2m_e\epsilon_0} \sum_j \frac{(\omega^2 - \omega_j^2)\, g_j}{(\omega_j^2 - \omega^2)^2 + \gamma_j^2\omega^2} \tag{3.17}$$

$$\text{Im}[n] = -\frac{n_a e^2}{2m_e\epsilon_0} \sum_j \frac{\gamma_j\omega\, g_j}{(\omega_j^2 - \omega^2)^2 + \gamma_j^2\omega^2}. \tag{3.18}$$

Now, if we rewrite our plane wave using $k = nk_0$, we have

$$\begin{aligned}
\psi(\boldsymbol{x}, t) &= \psi_0 \exp[-i(n\boldsymbol{k_0} \cdot \boldsymbol{x} - \omega t)] \\
&= \psi_0 \exp[-i(\boldsymbol{k_0} \cdot \boldsymbol{x} - \omega t)] \\
&\qquad \exp\big[-i\,\text{Re}[n-1]\,\boldsymbol{k_0} \cdot \boldsymbol{x}\big] \exp\big[\text{Im}[n]\,\boldsymbol{k_0} \cdot \boldsymbol{x}\big]. \tag{3.19}
\end{aligned}$$

From Equation 3.19 we can now see that the index of refraction describes the behavior of the wave in the material. The imaginary part of n describes the attenuation of the wave in the material, and the real part of n, in the oscillating term, describes the phase shift of the wave relative to vacuum.

3.1.2 The Oscillator Strengths

We have oscillation frequencies across the spectrum, from very low energy vibrational states to optically excited valence states to inner-shell absorption of x-rays. But is there a part of the spectrum where there is a greater concentration of oscillators? By ignoring the damping terms γ_j and examining Equation 3.16, we see that there exists a natural frequency called the plasma frequency,

$$\omega_p^2 = \frac{n_a e^2}{m_e\epsilon_0} \sum_j g_j = \frac{n_a e^2 Z}{m_e\epsilon_0}. \tag{3.20}$$

For most solids, the plasma frequency has a peak corresponding to an energy of about 10–20 eV.

If we are interested in energies in the high frequency limit, above the plasma frequency, where $\omega \gg \omega_j$ and for low damping ($\gamma \to 0$), we can reduce the

equation for the refractive index to

$$n \simeq 1 - \frac{n_a e^2}{2 m_e \epsilon_0} \sum_j \frac{(\omega^2 + i\gamma_j \omega) g_j}{\omega^4} \tag{3.21}$$

$$= 1 - \frac{n_a e^2}{2 m_e \epsilon_0} \frac{1}{\omega^2} \sum_j \left(1 + \frac{i\gamma_j}{\omega}\right) g_j \tag{3.22}$$

$$= 1 - \frac{n_a}{8\pi^2 \epsilon_0} \lambda^2 r_e \sum_j \left(1 + \frac{i\gamma_j}{\omega}\right) g_j \tag{3.23}$$

using $\omega = 2\pi/\lambda$ and $r_e = e^2/m_e c^2$.

We can write n in a different form:

$$n = 1 - \delta - i\beta = 1 - \alpha\lambda^2(f_1 + if_2) \text{ where } \alpha \equiv \frac{n_a r_e}{2\pi}, \tag{3.24}$$

and we have chosen to separate n into its real and imaginary parts, using

$$f_1 = \frac{1}{4\pi\epsilon_0} \sum_j g_j \tag{3.25}$$

$$\text{and } f_2 = \frac{1}{4\pi\epsilon_0} \sum_j \frac{\gamma_j}{\omega} g_j \tag{3.26}$$

The quantity $(f_1 + if_2)$ then represents the complex number of oscillators associated with the atom. Now let's write our plane wave again using this form of n.

$$\psi = \psi_0 \exp[-i(k_0 n z - \omega t)] \tag{3.27}$$

$$= \psi_0 \exp[-i(k_0 z - \omega t)] \exp[ik_0 \alpha \lambda^2 f_1 z] \exp[-k_0 \alpha \lambda^2 f_2 z]. \tag{3.28}$$

We now see that the phase-shifting part of the wave function, $\exp[ik_0 \alpha \lambda^2 f_1 z]$, is associated with f_1. The negative sign in the term $\exp[-k_0 \alpha \lambda^2 f_2 z]$ tells us that f_2 determines the attenuation of the wave.

3.1.3 Finding the Factors f_1 and f_2

Now that we have an expression for the complex index of refraction, how can we measure it? When we illuminate a sample of thickness z, we measure the intensity of the wave that passes through it, $I = \psi^\dagger \psi = I_0 \exp[-2k_0 \alpha \lambda^2 f_2 z]$. This is often written as $I = I_0 \exp[-\mu z]$ where μ is the linear absorption

coefficient,

$$\mu = 2k_0 \alpha \lambda^2 f_2 = 2n_a r_e \lambda f_2. \tag{3.29}$$

If we measure the absorption of photons by a thin film of material, we can calculate f_2 for that material at the measured photon energy. Remember that Equation 3.28 assumes that the incident photon energy is much greater than the plasma frequency of the material, or greater than 50 eV. This equation also breaks down near thresholds, where $\omega \sim \omega_j$.

We know how to find f_2 experimentally, but how can we find f_1? Notice that Equations 3.17 and 3.18 share the same parameters, g_j, ω_j and γ_j. This means that we can calculate $\text{Re}[n(\omega)]$ from a complete knowledge of $\text{Im}[n(\omega)]$. The equations that relate the two are

$$\text{Re}[\epsilon(\omega)] = 1 + \frac{2}{\pi} P \int_0^\infty \frac{\omega' \text{Im}[\epsilon(\omega')]}{\omega'^2 - \omega^2} d\omega' \tag{3.30}$$

$$\text{Im}[\epsilon(\omega)] = -\frac{2\omega}{\pi} P \int_0^\infty \frac{\text{Re}[\epsilon(\omega') - 1]}{\omega'^2 - \omega^2} d\omega' \tag{3.31}$$

where P is the principal part of a complex integral. These equations are called Kramers-Kronig relations, or dispersion relations, and can be found by making the assumption of causality between the polarization and the electric field [8], meaning that the polarization is caused by the electric field. They can be related to the index of refraction by $n \simeq \sqrt{\epsilon(\omega)/\epsilon_0}$. This means that after measuring the absorption of a material to obtain f_2, we can then use equation (3.30) to calculate f_1. Figure 3.1 is a plot of the coefficients f_2 and f_2 from tabulated data [12]. This plot shows the relationship between the phase-shifting part, f_1 and the attenuation coefficient f_2, as is described by the Kramer-Kronig equations.

Calculations of f_2 by measuring absorption data from dozens of thin films [12] show that the attenuation coefficient f_2 decreases approximately as E^{-2} away from absorption edges, as shown in Figure 3.2, a plot of f_2 for the elements gold, copper, silicon and carbon. At the absorption edge f_2 rises sharply because the photon energy is sufficient to remove an inner electron from the atom.

3.2 Near-Edges and Chemistry

Figure 3.2 shows clear steps at the absorption energy of the atoms carbon, silicon, copper and gold. This neat picture does not tell the whole story. Near to but below the absorption edge are resonances that correspond to electronic transitions of an inner shell electron to states near the vacuum level. This
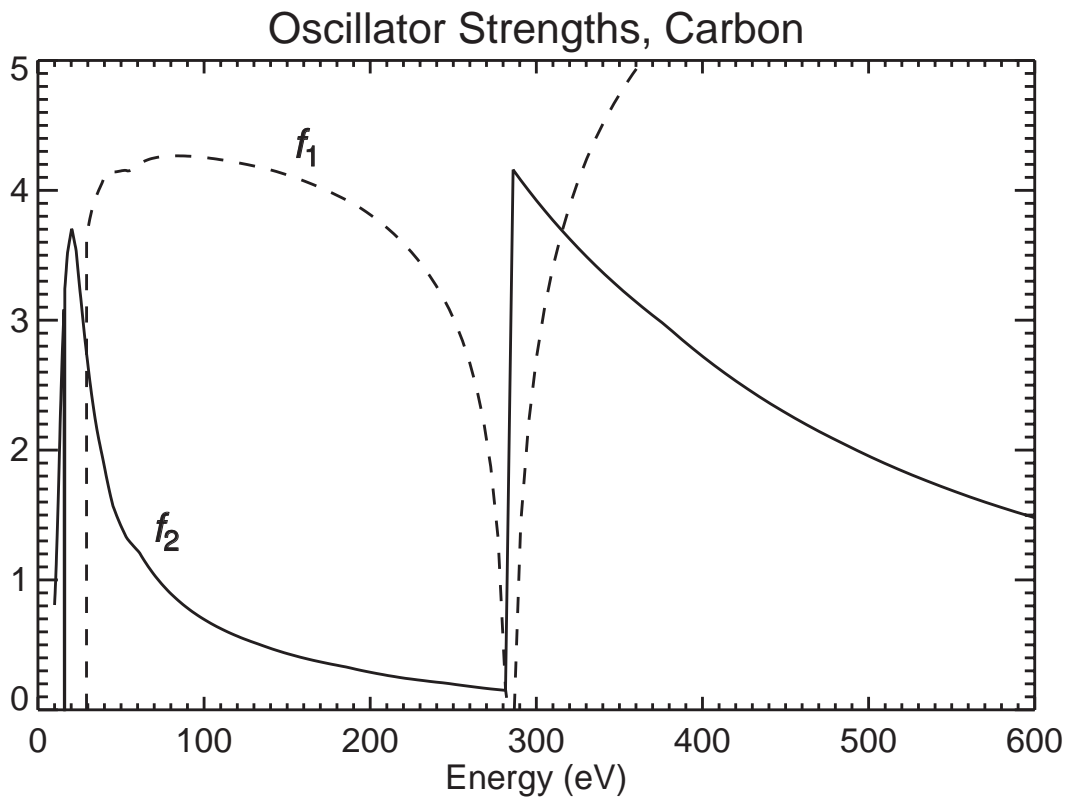
Figure 3.1: A plot of oscillator strengths f_1 and f_2 for carbon, as tabulated by Henke *et al*[12]
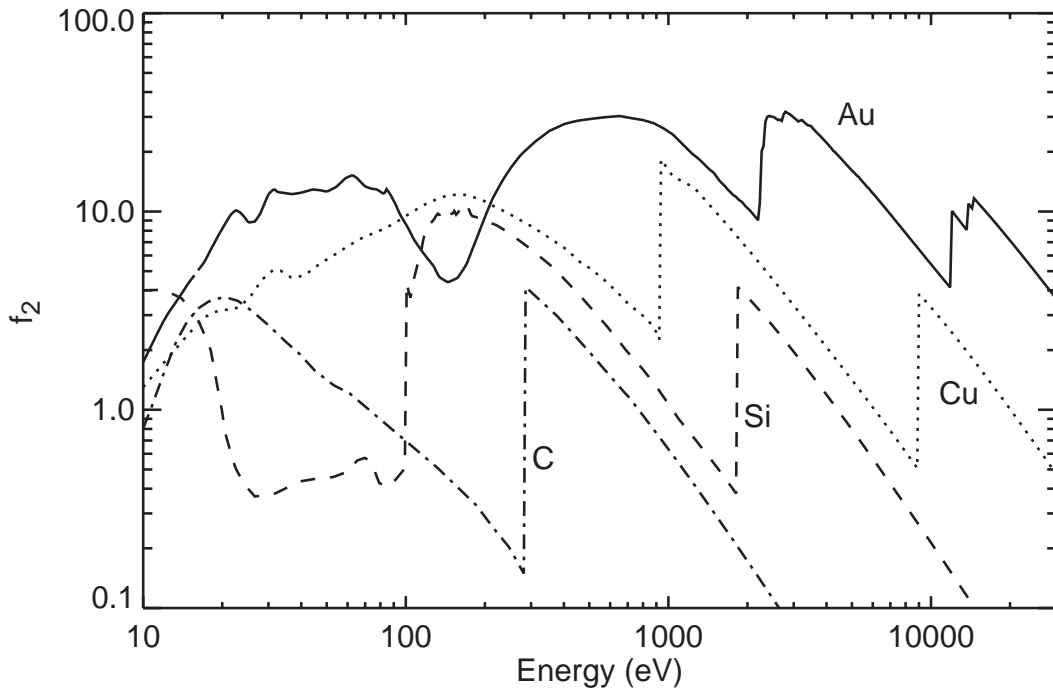
Figure 3.2: A plot of f_2 for the elements gold, copper, silicon and carbon, as tabulated by Henke *et al*[12].

structure, within a range of about 30 eV of the absorption edge, is called x-ray absorption near-edge structure (XANES) or near-edge x-ray absorption fine structure (NEXAFS). In atoms these states correspond to unoccupied atomic orbitals below the vacuum level. In molecules, the near-edge structure results from transitions to unfilled molecular orbitals. The XANES spectrum of an atom or molecule is characteristic of its structure, and can be used as identification of the presence of the substance or to give clues as to the chemical structure. These applications will be covered in detail in Chapter 4 of this thesis.

The K-edge XANES spectrum refers to the excitation of a K-shell electron to states near the vacuum level.

3.3 Analyzing Stacks

A typical STXM data stack consists of a 100 by 100 pixel image of the sample scanned across 150 energies. That is 10,000 spectra for a single data set. If the sample is made up of regions of pure substances for which one has reference spectra, then analysis is fairly straightforward. But environmental and biological samples are often very complex, and the components that make up the sample may not be known beforehand. This section describes a method developed by Lerotic et al [21, 22] to deal with this complexity.

Principle component analysis (PCA) [23] is used to orthogonalize the data set and to eliminate much of the noise in the data. An unsupervised pattern matching algorithm called cluster analysis [24] is then used to group pixels according to similarity in their spectra.

In x-ray spectromicroscopy we measure the absorption of x rays as they pass through the sample. We can define an optical density, $D(E)$ of a thin film of thickness z and absorption coefficient $\mu(E)$ to be

$$D(E) = -\ln\left(\frac{I(E)}{I_0(E)}\right) = \mu(E)z \tag{3.32}$$

where we have used the Lambert-Beer from Equation 1.3. Spectromicroscopy data sets consist of a series of images, or 'stack' of images [7, 25], across a range of energies.The optical density of each pixel at a specific energy E_i can be written as

$$D(E_i) = \mu(E_i) \cdot z. \tag{3.33}$$

From these data at $n = 1 \ldots N$ energies we can form a data matrix $D_{N \times P}$ with columns indexed by $p = 1 \ldots P$ for pixels. The pixel indices refer to image positions $p = i_{col} + (i_{row} - 1) \cdot n_{rows}$ where i_{col} and i_{row} are indexed starting

from a value of one.

If the sample is made up of $s = 1 \ldots S$ spectroscopically distinct components, then we can write the optical density of a pixel p at energy n as a sum of the thickness z_{sp} of each component s at pixel p times the absorption coefficient μ_{ns} of component s at energy n. That is,

$$D_{np} = \mu_{n1}z_{1p} + \mu_{n2}z_{2p} + \cdots + \mu_{nS}z_{Sp} = \sum_{s=1}^{S} \mu_{ns}z_{sp}, \qquad (3.34)$$

more simply written in matrix notation,

$$D_{N \times P} = \mu_{N \times S} \cdot z_{S \times P}. \qquad (3.35)$$

3.3.1 Principle Component Analysis

For samples which contain large areas of pure substances, the data can be interpreted by using reference spectra for the known materials in the sample to obtain compositional maps of the sample [26]. However, for many biological and environmental samples, the sample is made up of many substances for which a reference spectrum is not known. It is difficult to process these data sets by hand, first because there are 10,000 spectra in a typical stack, and second because subtle differences in spectra may be overlooked by relying solely on one's eye. Principle component analysis is one method that can be used to characterize the data set in terms of its most significant features. Factor analysis techniques such as PCA were initially developed for use by behaviorial scientists in the early 20th century [27, 28], but was discovered to be useful by the chemical profession in the 1970s [23]. It has recently been extended for use in x-ray absorption spectroscopy [29], electron energy-loss spectromicroscopy [30] and x-ray spectromicroscopy [31, 32].

In PCA the data set is rewritten in terms of a number of abstract components $s = 1 \ldots S_{abs}$ where $S_{abs} \leq N$ [23]. These components do not correspond to physical chemical spectra, but represent the most significant features of the spectroscopic data, and may be linear combinations of the actual chemical components in the sample. We can rewrite our data in terms of column and row matrices as

$$D_{N \times P} = C_{N \times S_{abs}} \cdot R_{S_{abs} \times P}, \qquad (3.36)$$

where each column of the matrix $C_{N \times S_{abs}}$ contains a spectrum with N points of abstract component s and each row of the matrix $R_{S_{abs} \times P}$ contains an image with P pixels of abstract component s. To calculate the column matrix $C_{N \times S_{abs}}$, one can use either the spectral or spatial covariance of the data. The

spectral covariance matrix is formed by

$$Z_{N \times N} = D_{N \times P} \cdot D_{P \times N}^T. \tag{3.37}$$

The spectral covariance measures the correlation between images at each energy, and is a symmetric matrix. The spatial covariance $Z_{P \times P}$ can also be used, and may be more appropriate in some situations.

The column matrix $C_{N \times S_{abs}}$ that we are seeking is then made up of the eigenvectors of the covariance matrix:

$$Z_{N \times N} \cdot C_{N \times S_{abs}} = C_{N \times S_{abs}} \cdot \Lambda_{N \times N}, \tag{3.38}$$

where $S_{abs} = N$ and $\Lambda_{N \times N}$ is a diagonal matrix made up of the eigenvalues $\lambda(s)$ of the covariance matrix. The columns of $C_{N \times S_{abs}}$ are made up the eigenvectors (called eigenspectra) in order of decreasing eigenvalue. An eigenimage matrix can be found by solving Equation 3.36 as

$$R_{S_{abs} \times P} = C_{N \times S_{abs}}^T \cdot D_{N \times P} \tag{3.39}$$

where we used $C^{-1} = C^T$ because C is composed of eigenvectors, and is therefore orthogonal.

The first eigenspectrum is something like an average of all the spectra in the image, and the second eigenspectrum is the largest difference from the first eigenspectrum. Each following eigenspectrum displays differences from the first that are less significant than the last, until the differences between one eigenspectrum and the next is due to nothing but random fluctuations due to noise. Therefore we can choose a subset of significant eigenspectra that together represent the important features of the sample. Note that after the first component, the eigenspectra may have negative values, which is clearly unphysical and demonstrates that the principle components do not represent real spectral signatures. For this reason PCA is used as a first step to orthogonalize and reduce the data set before applying pattern matching algorithms.

3.3.2 Cluster Analysis

After PCA has been applied to the data set, the data is orthogonalized by identifying eigenspectra and noise-filtered by eliminating higher-order eigenspectra. Next we will use cluster analysis, or unsupervised pattern matching [24] to group pixels with similar experimentally-determined spectra together.

In the data matrix, each pixel p is represented by its response at each of N energies. In the eigenimage matrix each pixel is represented by a weighting $R_{s,p}$ of each abstract component s. Pixels with similar spectra will have similar

weights, and therefore form natural 'clusters' at a location in the eigenimage space, as depicted in Figure 3.3. First we locate cluster centers in this S_{abs}-dimensional space and then classify pixels according to their distance to each cluster center. The initial guesses for cluster centers are uniformly scattered about the origin, so each eigenimage is shifted so that the pixels are centered about the origin of each component. This is done by subtracting the average of each eigenimage from itself. The steps to cluster the data are illustrated in Figure 3.3 and are as follows:

1. We assign random positions to each of G cluster centers. The number of cluster centers is generally larger than the number of significant components chosen.

2. We choose a pixel p at random and calculate the distance from that pixel to each of the G cluster centers. The cluster center that is closest is then moved toward the pixel, as pictured in Figure 3.3. Repeating this step for the remaining pixels results in each cluster center being moved to the center of a natural grouping of the data.

3. After the cluster centers have been found, each pixel is assigned to the closest cluster center.

At the end of the algorithm, there may be cluster centers which were not close to any pixels and so were never moved. The clusters associated with those cluster centers will have no members, and so are eliminated from the list of cluster centers.

The clusters are displayed as false-colored maps.The spectra from all the pixels that belong to a cluster are averaged to produce color-coded spectra.These spectra can then be compared to standard spectra to understand the chemistry differences present in the sample. The cluster analysis is able to pick out subtle differences in chemistry, as will be described in Chapter 4.

Angle-distance Measure

Consider two pixels, one from a thick section of the sample and one from a thinner section of the sample, but chemically identical. In the eigenimage matrix representation, the two pixels will have the same ratio of component weights. In this case, a simple Euclidean distance measure, $\sqrt{x^2 + y^2 + z^2}$ for dimensions x, y and z, would not be the best measure to use. If the Euclidean distance measure were used, areas of thicker sample would show up as a distinct cluster, when what we actually want is clusters based purely on differences in spectra, not thicknesses.
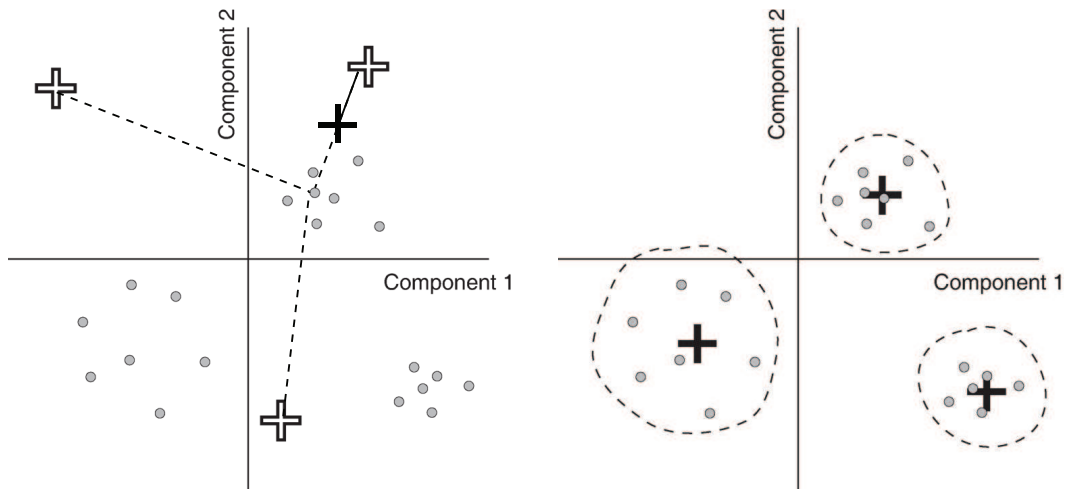
Figure 3.3: An illustration of the clustering algorithm, adapted from [15]. The data points p are plotted here based on their weights $R_{i,p}$ and $R_{j,p}$ in two eigenimages i and j. (a) Initial guesses for cluster centers G are randomly positioned about the origin. For each pixel p the distance to each cluster center is calculated, and the closest cluster center is moved closer to that pixel. This process is repeated over all pixels. (b) Once the cluster centers have been set, each pixel is assigned to the closest cluster center.

To cluster pixels of different thicknesses but similar chemistry together, we use instead an angle distance measure [33]. If we have a specimen with two distinct unknown compositions and varying thickness, we can represent the data (using PCA) by two significant components. We expect that pixels of the same composition but different thickness would be plot along a line extending from the origin, as illustrated in Figure 3.4. If Euclidean distance were used, pixels would tend to be clustered based on their distance from the origin rather than their ratio of PCA components. The angle distance measure, θ, or normalized scalar product, is defined as

$$\theta = \arccos \frac{\sum_i x_i y_i}{\sqrt{\sum_i x_i^2 \cdot y_i^2}}. \tag{3.40}$$

Angle distance measure is a measure of the angle between pixels, disregarding the radial distance from the origin. The illustration of angle distance measure in Figure 3.4 suggests that angle distance measure will better distinguish between chemically different pixels, independent of the sample thickness.

3.4 Calculating Sample Thickness

3.4.1 The Engstrom Model

Suppose we look at a sample on either side of the carbon edge. We wish to find out if the sample has some carbon in it, but we also know that it must have other elements in it as well. We will do this by acquiring images at an energy E_1 below the edge and at an energy E_2 above the edge. The intensity we measure at energy E_1 can be written as

$$I_{11} = I_{01} \exp\left[-\mu_{1s}z_s - \mu_{1b}z_b\right], \tag{3.41}$$

where the subscripts s and b refer to edge and non-edge elements, respectively. We can rewrite this equation using $m = \rho z$, where m is the mass per unit area, ρ is density and z is the sample thickness. Then we have

$$I_{11} = I_{01} \exp\left[-\left(\frac{\mu_1}{\rho}\right)_s m_s - \left(\frac{\mu_1}{\rho}\right)_b m_b\right]. \tag{3.42}$$

Similarly, we can write the intensity at E_2 as

$$I_{12} = I_{02} \exp\left[-\left(\frac{\mu_2}{\rho}\right)_s m_s - \left(\frac{\mu_2}{\rho}\right)_b m_b\right]. \tag{3.43}$$
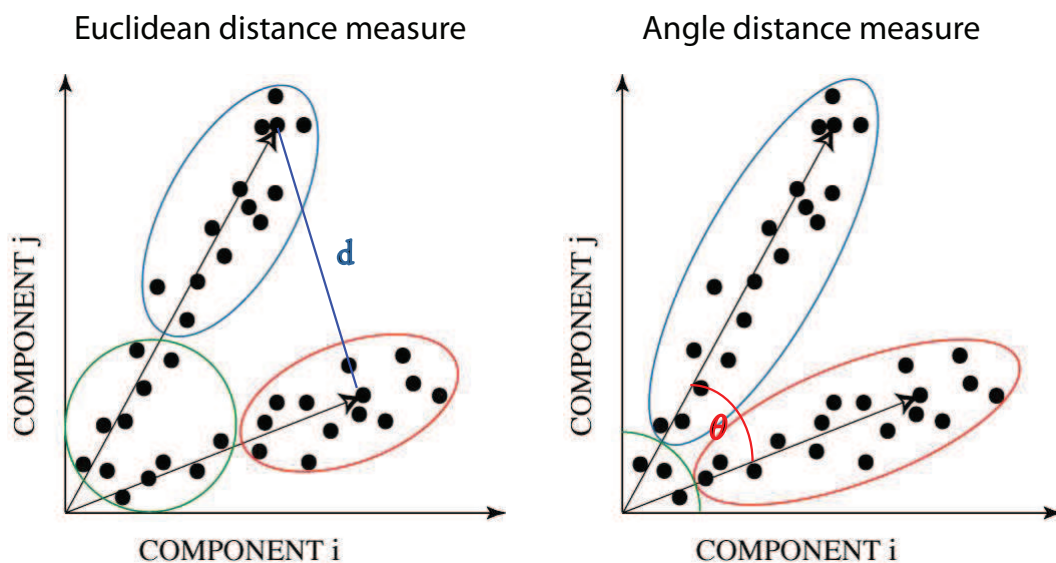
Figure 3.4: An illustration of the angle distance measure, adapted from [15]. A specimen made of two compositions is represented by two significant components. The pixels with the same composition but different thicknesses are plotted along a line extended from the origin. The Euclidean distance measure at left groups pixels of different thicknesses into different clusters. The angle distance measure at right clearly obtains a better clustering of the data into chemical rather than thickness based clusters.

Now solve both equations for m_b:

$$m_b = \frac{\ln\left(\frac{I_{01}}{I_{11}}\right) - \left(\frac{\mu_1}{\rho}\right)_s m_s}{\left(\frac{\mu_1}{\rho}\right)_b} = \frac{\ln\left(\frac{I_{02}}{I_{12}}\right) - \left(\frac{\mu_2}{\rho}\right)_s m_s}{\left(\frac{\mu_2}{\rho}\right)_b}. \tag{3.44}$$

After eliminating m_b the equation can be solved for m_s.

$$\left(\frac{\mu_2}{\rho}\right)_b \ln\left(\frac{I_{01}}{I_{11}}\right) - \left(\frac{\mu_1}{\rho}\right)_b \ln\left(\frac{I_{02}}{I_{12}}\right) = \left[-\left(\frac{\mu_1}{\rho}\right)_b \left(\frac{\mu_2}{\rho}\right)_s + \left(\frac{\mu_2}{\rho}\right)_b \left(\frac{\mu_1}{\rho}\right)_s\right] m_s \tag{3.45}$$

$$m_s = \frac{\left(\frac{\mu_2}{\rho}\right)_b \ln\left(\frac{I_{01}}{I_{11}}\right) - \left(\frac{\mu_1}{\rho}\right)_b \ln\left(\frac{I_{02}}{I_{12}}\right)}{\left(\frac{\mu_2}{\rho}\right)_b \left(\frac{\mu_1}{\rho}\right)_s - \left(\frac{\mu_1}{\rho}\right)_b \left(\frac{\mu_2}{\rho}\right)_s} \tag{3.46}$$

$$= \frac{\ln\left(\frac{I_{01}}{I_{11}}\right) - \left(\frac{\left(\frac{\mu_1}{\rho}\right)_b}{\left(\frac{\mu_2}{\rho}\right)_b}\right) \ln\left(\frac{I_{02}}{I_{12}}\right)}{\left(\frac{\mu_1}{\rho}\right)_s - \left(\frac{\mu_2}{\rho}\right)_s \left(\frac{\left(\frac{\mu_1}{\rho}\right)_b}{\left(\frac{\mu_2}{\rho}\right)_b}\right)} \tag{3.47}$$

If we choose energies across a small interval, we can approximate $\frac{\left(\frac{\mu_1}{\rho}\right)_b}{\left(\frac{\mu_2}{\rho}\right)_b} \approx$ $\left(\frac{\lambda_1}{\lambda_2}\right)^{f(Z,\lambda_{1,2})}$, because the μ of the background element is smoothly varying across the interval. We can further assume a value of 3 for $f(Z, \lambda_{1,2})$ because $\mu \approx \text{constant} Z^4 \lambda^3$, as was shown in Section 3.1.3. Then the equation reduces to

$$m_s = \frac{\ln\left(\frac{I_{01}}{I_{11}}\right) - \left(\frac{\lambda_1}{\lambda_2}\right)^3 \ln\left(\frac{I_{02}}{I_{12}}\right)}{\left(\frac{\mu_1}{\rho}\right)_s - \left(\frac{\mu_2}{\rho}\right)_s \left(\frac{\lambda_1}{\lambda_2}\right)^3}. \tag{3.48}$$

The smaller the interval, the better the approximation

$$\left(\frac{\lambda_1}{\lambda_2}\right)^3 \approx 1 \tag{3.49}$$

holds, and the expression reduces to

$$m_s = \frac{\ln\left(\frac{I_{12}}{I_{11}}\right)}{\left(\frac{\mu_1}{\rho}\right)_s - \left(\frac{\mu_2}{\rho}\right)_s}. \tag{3.50}$$

This expression can be used to calculate a map of the edge element for the sample.

Use the equation for mass per unit area, $m_s = \rho z_s$, to find the thickness, z_s.

$$z_s = \frac{\ln\left(\frac{I_{12}}{I_{11}}\right)}{\mu_{1s} - \mu_{2s}}. \tag{3.51}$$

This is only valid if $(\lambda_1/\lambda_2) \approx 1$. Generally the energies chosen are several electron volts above and below the absorption edge, and so we must use the equation

$$z_s = \frac{\ln\left(\frac{I_{01}}{I_{11}}\right) - \left(\frac{\lambda_1}{\lambda_2}\right)^3 \ln\left(\frac{I_{02}}{I_{12}}\right)}{\mu_{1s} - \mu_{2s}\left(\frac{\lambda_1}{\lambda_2}\right)^3}. \tag{3.52}$$

This equation gives the thickness of the sample in terms of the measured intensities, but also relies on a knowledge of μ for the sample. This μ can be calculated from

$$\mu = 2n_a r_e \lambda f_2$$

using the tabulated values for f_2 from [34] and [12]. If the sample is composed of known compounds

This μ can be calculated for the edge element using Henke's tabulated f_2 values and an assumption of the density, ρ.

Calculating the Thickness of STXM Samples

To demonstrate the thickness calculation both a simulated data set and a real bacteria specimen will be used. The simulated sample is adapted from Lerotic [15]. Experimental spectra of the amino acids tyrosine and leucine, measured by Kaznachev *et al.* [35], and the collagen spectrum, measured by A. Osanna (unpublished), were used to construct the spectromicroscopy data. The background of the specimen was assigned transmission spectrum of 200 nm of collagen and the letters A, B, and C were assigned 10%, 50% and 90%, respectively, of tyrosine or leucine. Collagen was used to make total thickness of 200 nm. A few pixels at lower left was left empty to provide an I_0 normalization region.

For the transmission coefficients, I, used in the calculation of the thickness using Equations 3.51 and 3.52, averages of the signal over the energy regions 280-283 eV and 300-305 eV were used. Figure 3.5 shows the calculated thicknesses for both samples, calculated using the μ associated with the amino acid that makes up the letters, leucine and tyrosine. Both these coefficients were calculated using thin film data by Henke *et al.* [34]. To calculate μ, we

must make an estimate of the density of the compound, which highly affects the calculation of thickness. In the sample with tyrosine letters, we see that the tyrosine letters appear to be much thicker than the collagen background. Underestimating the density of a compound results in greater apparent thicknesses. The density of leucine in this example has been underestimated, resulting in an apparent thickness of about 230 nm throughout. This is because we can really only truly measure the product of density and thickness. The sample has uniform thickness throughout, but the differences in density among the three compositions result in nonuniform thickness results, as seen particularly in the sample with tyrosine letters.

Figure 3.6 shows the thickness calculation for a bacterium. The top image shows the thickness for the whole sample, and the graph below plots a cross section of the thickness across the sample as denoted by the red line. These rod-shaped bacteria should be as thick as they are wide. The thickness calculation, using μ_{protein} as a guess, underestimates the thickness of the bacterium.

The thickness calculation would work fairly well for a sample of large areas of known composition, but fails for samples where the μ is unknown in advance. One can obtain a map of the product of density and thickness, but no simple thickness map can be obtained.
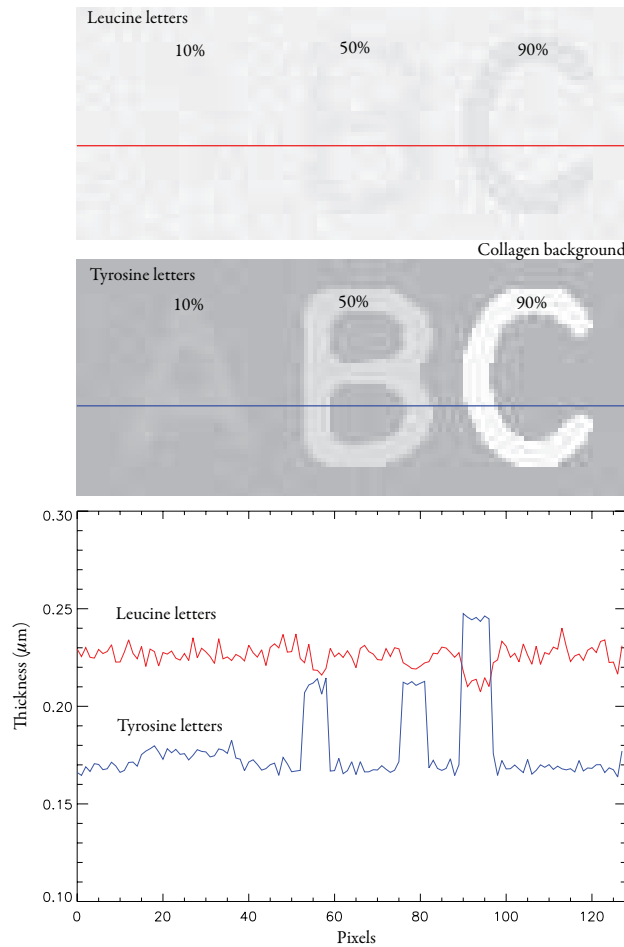
Figure 3.5: The simulated data set, adapted from [15], was constructed using experimental spectra of the amino acids leucine and tyrosine, measured by Kaznachev *et al.* [35], and collagen, measured by A. Osanna (unpublished). The letters A, B and C were assigned 10%, 50% and 90% compositions, respectively, of tyrosine or leucine, with collagen making up the rest of the 200 nm thickness. The background was filled with 200 nm of collagen. The thickness calculation depends on the choice of μ and density for the sample, which explains the apparent difference in thickness between the tyrosine letters and the collagen background.
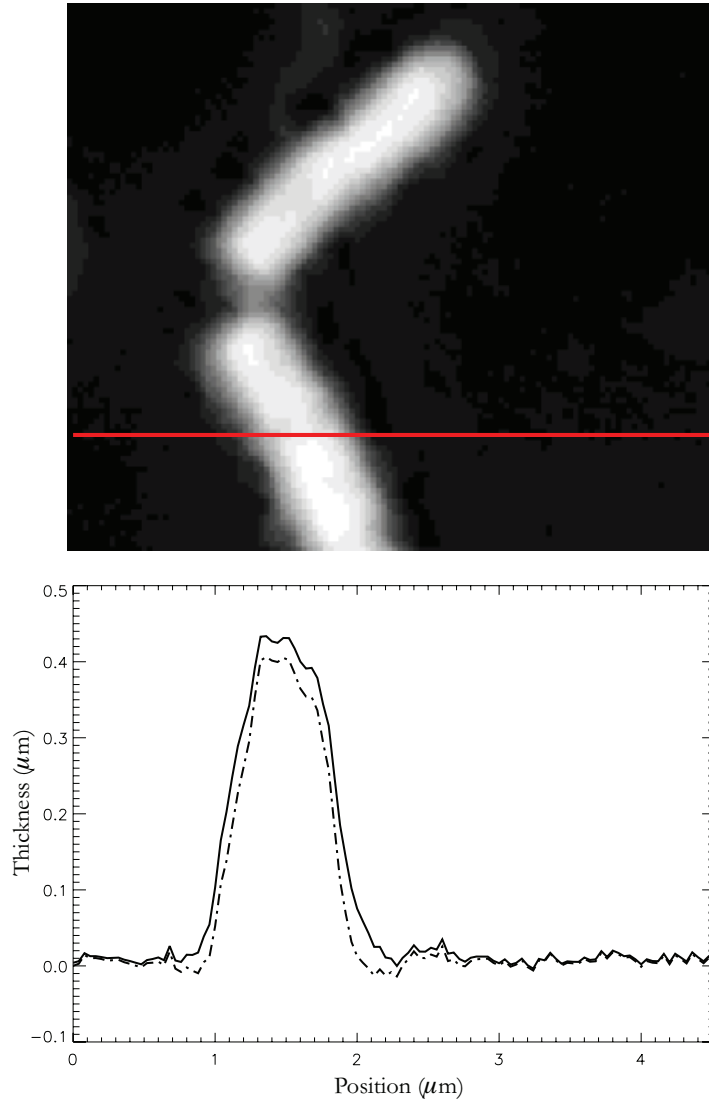
Figure 3.6: (a) A thickness map of an FRC bacteria sample. (b) A plot of the thickness cross section along the red line marked in (a). The dotted line was calculated using the approximation in Equation 3.51 and the solid line was calculated using the approximation of Equation 3.52.

60

Chapter 4

STXM Studies of Soil Bacteria

4.1 The Role of Bacteria in Soil Chemistry

There are between 100 million and 1 billion bacteria in each teaspoon of soil. This makes bacteria a highly important factor in the chemistry of soil, where they play a prominent role in the cycling, hydrologic transport and bioavilibility of metal ions and radionuclides in soils, aquifers and surface waters [36, 37]. As mentioned in Chapter 1, bacteria are capable of transforming the oxidation state and coordination chemistry of these contaminants through a variety of mechanisms, including metabolic processes where metals and radionuclides serve as electron acceptors for anaerobic respiration.

Microorganisms in the natural environment may interact with radionuclide and toxic metal contaminants through (i) sorption, (ii) intracellular accumulation, and (iii) transformation of chemical speciation. These interactions may retard or enhance the mobility of the contaminants via dissolution and precipitation reactions, biocolloid formation, or production of complexing ligands that affect solubility. An understanding of these interactions are critical to the design and implementation of biorememdiation strategies. In addition, current and planned radioactive waste repository environments, such as deep subsurface halite formations, have been found to harbor 'extremophiles;' microorganisms that have developed mechanisms which enable them to thrive in otherwise toxic environments. Life processes in these extreme environments have the potential to compromise the integrity of waste repositories; there is a paucity of information on how these bacteria detoxify their environment and how their activity will impact contaminant fate and mobility.

Microbes nad their organic exudates typically combine to form biofilms on a significant fraction of the reactive mineral surface area in soils. Sorption is a predominant non-metabolic mechanism by which biofilms influence

contaminant concentration and speciation. Metals and radionuclides bind to the bacterial cell via surface complexation reactions; the extent of reaction is dependent upon pH, ionic strength, metal speciation, competing ions, and bacterial species. Generally, the surface is composed of amino sugars, polypeptides, and phospholipids and depending upon the "gram" character of the cell, may have greater complexity (gram-negative) or be relatively simple (gram-positive). These biomolecules possess functional groups that, depending upon local pH of the cell, ionize and interact with metal species in the cell's external surface. A functional group is the part of a molecule where most of its chemical reactions occur. Predominant functional groups include carboxyl, phosphato, hydroxyl, and amine; the activities of these functional groups are primarily controlled by pH. Each group has a different pH at which it is deprotonated. In addition to surface-active functional groups, the biomembrane is permeable, and metal species can be transported across via translocation, porins, and porters. Once inside the cells, sequestration often occurs and the bioaccumulated metal may be "packaged" within a storage polymer (such as poly-hydroxybutyrate or polyphosphate). Understanding surface functionality responsible for contaminant uptake is critical for making assessments of fate and transport away from the contaminant source. In addition, knowledge of functional group association will allow for the prediction of contaminant-microbe stability, likelihood of interaction, and potential for contaminant immobilization or remobilization in the environment.

STXM can be used to provide spectroscopic information about a bacterial sample at 40 nm spatial resolution. X-ray absorption near-edge spectroscopy (XANES) contains information about the binding environment of the edge element (C, O and Fe in this work), as described in Section 3.2. Functional groups have unique electronic structures and therefore can be identified by specific electronic transitions or peaks within a XANES spectrum, and a 'building block' approach can be applied to analyze spectra [35]. Changes in the binding or coordination chemistry of these functional groups that perturb the electronic structure of the functional group will potentially result in measurable shifts in the peak energies of a spectrum. Standard spectra from single component model substances with known electronic structures can be compared to spectra from a complex bacterial sample to first identify the presence of specific functional groups and secondly to identify shifts due to metal binding. Figure 4.1 shows a representative C 1s bacterium spectrum with peaks assigned to specific functional groups and bonds.

The unique combination of high spatial resolution and spectroscopy enables novel investigations into the cell wall chemistry of single cells, and in specific cases the carbon chemistry of subcellular features such as carbon storage poly-

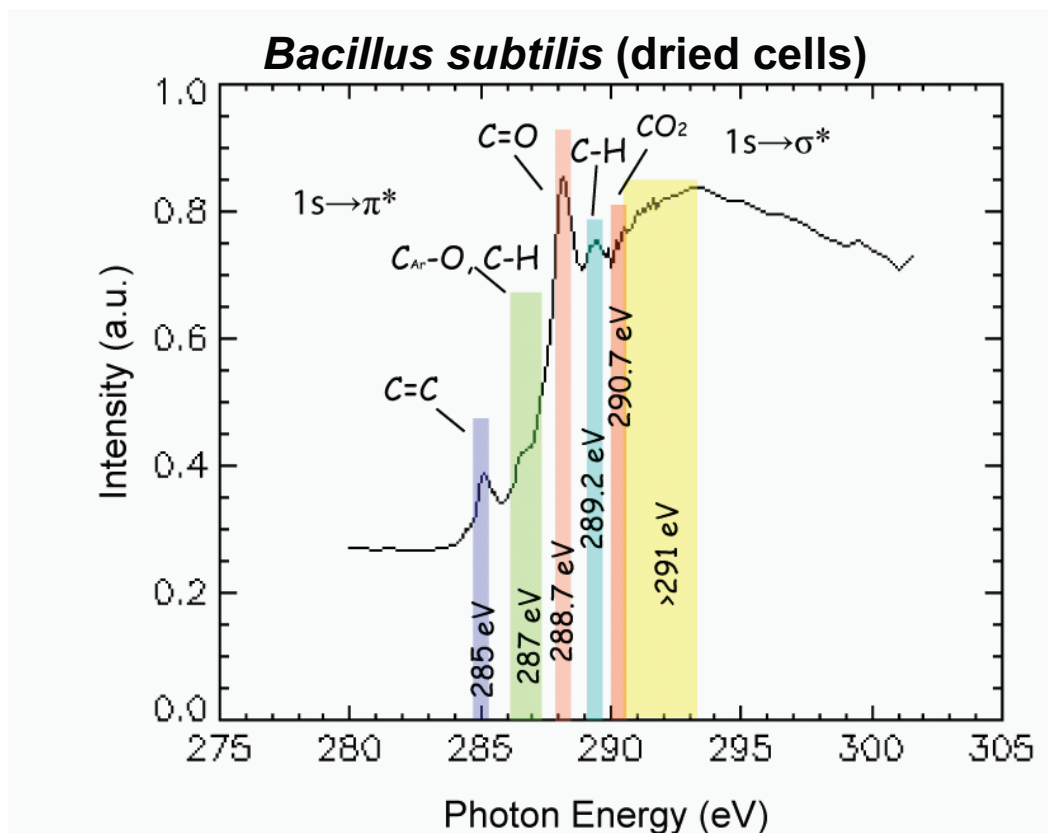Figure 4.1: A typical spectrum from the bacterium *Bacillus subtilis*. The colored vertical bars demark the ranges of peak energies observed for different functional groups and their various binding configurations. In this chapter it will be shown that changes in the position and shape of a specific peak can be used to identify changes in chemistry in the bacterium due to interactions with contaminants.

mers and spores can be investigated. Current models of cell composition and functional group chemistry are based on mass balance reconstructions, where large numbers of cells are digested, separated and the separates are analyzed using mass spectrometry. Research presented in this chapter are among the first single cell investigations using C $1s$ spectroscopy to study cell wall functional group chemistry (Section 4.2.1), carbon storage polymers used for environment detoxification (Section 4.2.2) and sporulation as a survival mechanism (Section 4.2.3).

STXM can also be used to investigate metal-bacterial interaction from the perspective of the metal ion. Metal binding to bacteria and mineral surfaces, and the solubility of different mineral phases is often determined by the valence state of the metal ion. The valence state of a metal ion can in many cases be readily identified by features in a XANES spectrum at the absorption edge of the metal. The iron L_2 absorption edge is used in Section 4.3 to investigate the biomineralization of goethite and ferrihydrite. These two $Fe_{(III)}$-containing minerals are ubiquitous in soils and their relative abundance greatly impacts soil reactivity towards contaminants and nutrients alike.

It is also possible to study the sorption of a metal ion or radionuclide onto microbial cell walls and biomass from the point of view of the carbon edge. For example, a relatively small shift in the carboxyl peak to higher energy indicates cation binding to the carboxyl functional groups. This trend is confirmed in this work by observing similar shifts for Ca, U and Ni cation binding to carboxyl functional groups. Section 4.4 will present studies of uranium-bacteria interactions using STXM at the carbon edge that show how the carbon spectrum is sensitive to both uranium binding to functional groups at the bacterial surface and changes in the valence state of the surface-bound uranium. The oxidized, water-soluble form of uranium, U(VI) is used as an electron acceptor by the *Geobacter* species of bacteria to form the insoluble form U(IV) [38]. In Section 4.4 it will be shown that the changes in the uranium chemistry due to interaction with a *Clostridium* species can be identified by shifts in the carbon $1s$ absorption spectrum of the bacteria-uranium sample.

The final section of this chapter (Section 4.5) combines spectroscopic and scattering methods to investigate how nickel-resistant bacteria employ different mechanisms to detoxify their immediate environment. Bacteria-metal ion interactions can be divided between active mechanisms where the metal ion is integral to a particular metabolic process, and passive mechanisms where metal ions interact with biomass but do not directly factor into cell metabolism. Active mechanisms include scavenging aqueous and mineral-bound electron donor metal ions, and detoxification processes that expel metal ions from the cell body. Passive mechanisms include metal ion complexation by functional

groups at the cell surface or in biomass exudates, and metal ion precipitation in or around the cell membrane as a result of chemical gradients in the near-cell environment. There is a critical need to understand the complex relationship between cell metabolic processes and the passive mechanisms controlling metal ion availability and fluxes in the near-cell environment. STXM spectroscopic and dark field imaging are used in Section 4.5 to directly characterize the spatial distribution of nickel(II)-containing precipitates and nickel-organic complexes at the cell surface of two strains of Ni-resistant bacteria.

The collection of STXM results presented in this chapter demonstrates the powerful insights into the chemistry of microbial processes made possible by combining sub-cellular spatial resolution with spectroscopic and scattering methods. Section 4.2.1: C 1s spectra do reveal differences in the relative intensity at the carboxyl peak position between gram negative and gram positive bacteria, which is consistent with expectation that gram positive bacteria have more carboxyl groups within its cell wall. Section 4.2.2: Intracellular PHB granules are clearly identified by its unique carbon chemistry, although further model compound studies are required to determine the distinguishing spectral features identified in the cluster analysis. Section 4.2.3: Intracellular spores are clearly identifiable by its relatively high dipicolinic acid concentration relative the surrounding cell body; chemical changes were also properly correlated with the evolution of endospores to spores. Section 4.3: C 1s spectral images highlight the strong interaction between iron phases and extracellular polymer substances, and Fe L edge spectral images reveal *Clostridium*'s ability to reduce ferrihydrite to an Fe(II)-containing phase which is relatively stable against re-oxidation. Section 4.4: C 1s spectral images indicate that uranyl ions sorb onto the bacterial cell wall by binding to the carboxy functional groups at the cell surface. Section 4.5: Detailed analyses of the carboxyl peak in C K-edge spectra and dark field scattering images of nickel hydroxide precipitates indicate that both active metabolic and passive sorption mechanisms play significant roles in controlling the concentration of bioavailable nickel in the near-cell environment. The results also expose current limitations that must be overcome before revealing the next details of the chemistry of microbial processes including heterogeneity of cell wall functional group distribution; some limitations are simply a matter of more close involvement of microbiologist to design experiments, develop sample preparation methods and conduct model compound studies in wet cells; while other limitations will be overcome by the next generation of focusing optics, detectors and data analysis software.

4.2 Cell Wall Chemistry and Subcellular Features

Bacteria are termed prokaryotic microorganisms because they do not have a membrane-bound nucleus as do eukaryotic cells found in animals, plants, fungi and protists. Therefore, the cell wall of a bacterium is the only membrane separating its genetic information from the surrounding environment. As a result, cell wall chemistry has a major role in protecting the genetic information within the cell from toxins in the environment. Bacteria have also developed other defense mechanisms within the cell body, two of which, spores and intracellular carbon storage compounds, present subcellular features large enough to investigate using STXM-based spectroscopic methods. In both cases, STXM can provide important molecular chemical information by identifying and fingerprinting the predominant organic carbon species. The spore and biopolymer-forming bacteria play an important role in the biotransformation of radionuclides and toxic metals in wastes and impacted environments. Subcellular structures such as membrane-bound polyhydroxybuterate affect metal ion accumulation within the cell.

In the first subsection, *Clostridium* species BC1 and *Ralstonia* species CH34 provide examples of the two types of cell wall structure found in bacteria. STXM is used to investigate cell wall chemistry of the two contrasting structural types. In the second subsection, STXM will be used to image subcellular features including carbon-storage polymers, exopolysaccharides and spores in whole cells of the bacterial genera *Clostridia, Bacillus, Pseudomonas* and *Ralstonia* These genera are found in natural soil environments and were chosen for their resistance to heat, desiccation, toxic metals or radiation.

4.2.1 Gram-Positive and Gram-Negative Bacteria

The cell membrane protects the cell interior from external hazards and transports molecules such as carbohydrates, vitamins, amino acids, and nucleotides into and out of the cell. The Gram stain is used to distinguish between the two fundamentally different types of bacterial cell walls based on their ability to retain the dye crystal violet, which depens on the physical and chemical structure of the cell wall. Those cells that maintain the stain are called 'gram positive,' and those that do not retain the stain are called 'gram negative.' The surfaces of gram negative cells are more complex than those of gram positive cells, as shown schematically in Figure 4.2. The wall of gram-positive cells is made of two major layers. The first layer is composed of multiple sublayers of peptidoglycan, which is a linear polymer of alternating units of *N*-acetylglucosamine
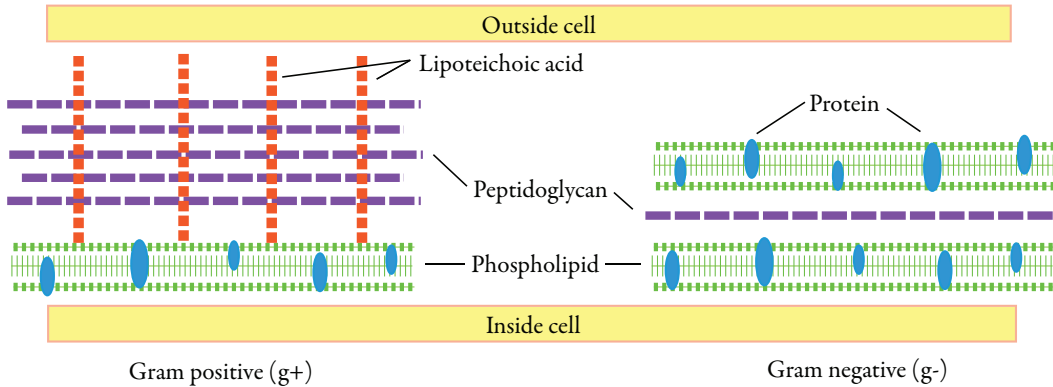
Figure 4.2: Drawing of contrasting of gram-positive and gram-negative cell wall structures. The gram-positive cell surface has two major structures: the cell wall and the cell membrane. The cell wall of gram-positive cells is composed of multiple layers of peptidoglycan, a linear polymer. In gram-negative cells, the peptidoglycan forms a single monolayer. An outer membrane surrounding the gram-negative cell is composed of phospholipid, lipopolysacharide, enzymes and other proteins. Table 4.1 further compares the composition of gram-positive and gram-negative cell structures.

and *N*-acetylmuramic acid, as shown in Figure 4.4. In gram-negative cells, a monolayer of peptidoglycan makes up one layer of the membrane, and an outer membrane is composed of phospholipids, lipopolysacharide, enzymes and other proteins [39]. Table 4.1 compares the composition of gram-positive and gram-negative cell structures. It is important to note that the cell wall of gram-positive cells is made up primarily of peptidoglycan while the gram-negative cell wall is constructed of mostly lipids and lipoproteins. Teichoic acid is only present in the gram-positive cell wall .

Clostridium is a genus of gram-positive bacteria. They are obligate anaerobes, meaning they cannot survive in the presence of oxygen. They are capable of producing spores, which makes them particularly resistant to heat and dessication. The genus Clostridium includes the species *botulinum*, responsible for producing the toxin botulism, and also the species *tetanus*, the cause of tetanus infections. The species of Clostridium used in the work in this chapter was isolated from the residues that remain following coal-cleaning at power generating plants. Its growth is unaffected by the presence of metal oxides such as manganese, iron, nickel and cadmium oxides [40]. As shown in [40], the solubility of the metal oxides are changed by direct or indirect mechanisms due to the presence of the bacterium. This particular organism is referred to

Property	Gram Positive	Gram Negative
Thickness of wall	20-80 nm	10 nm
Number of layers in wall	1	2
Peptidoglycan	>50%	10-20%
Teichoic acid in wall	Yes	No
Lipid and lipoprotein content	0-3%	58%
Protein content	0%	9%
Lipopolysaccharide	0%	13%

Table 4.1: Comparison of gram-positive and gram-negative cell wall structures. The two differences we will attempt to exploit using STXM is the presence of teichoic acid and the large quantity of peptidoglycan in the gram-positive cell wall. There is no teichoic acid in the gram-negative cell-wall and only a small fraction of the gram-negative wall is made of peptidoglycan.

as BC1 in this chapter.

Ralstonia is a gram-negative bacterium able to grow autotrophically in a mineral medium under a gas mixture containing H_2, O_2 and CO_2 at various ratios. A strain of nickel-, cobalt- and cadmium-resistant *Ralstonia* was isolated from a decantation tank of a zinc factory in Belgium.

The bacteria were grown in a mineral medium and sampled at 24 and 48 hours. The culture was determined to be in the exponential growth phase at 24 hours and had reached the stationary growth phase by 48 hours. The samples were rinsed in double distilled water and centrifuged at $5000g$ for 10 minutes to separate the cells from the medium. They were rinsed and spun down three times to leave little growth medium in the cell sample. Finally the cells were mixed in double-distilled water and a droplet (about a microliter) was placed on a silicon nitride window and allowed to air-dry. A series of 4 μm $\times$ 4 μm images were taken in the STXM at NSLS X1A1 at 40 nm resolution. The images were taken at energies between 280 and 305 eV at 0.1 eV steps. (Lower energy resolution was used in the normalization regions of 280-283 eV and 290-305 eV in order to save time and avoid unneccessary damage to the sample.) Taken together, these images form a 'stack' of data. The images in the stack are aligned and processed using the program `stack_ analyze` written by members of the Stony Brook X-ray Microscopy Group. The program is available for download at the group website http://xray1.physics.sunysb.edu. An I_0 spectrum is obtained by selecting the pixels in the stack that have the highest transmitted flux, and therefore are free of sample. The stack is then processed using PCA and cluster analysis as described in Section 3.3.

Pure standards were dissolved in double-distilled water. A droplet was

placed on a silicon nitride window and allowed to air-dry. Because the standards are homogeneous, taking a spectral image sequence is not necessary; instead several point spectra were taken and averaged. To obtain a point spectrum, a suitably thin section of the dried film was found by comparing the photon count rate through an empty portion of the window (the I_0 signal) to the sample-filled section (the I signal). The sample is then brought out of focus by $10 \mu m$. This increases the beam spot size on the sample, and so reduces the damage to the sample by reducing the number of photons per area incident on the sample. The absorption spectrum is taken from 280 to 305 eV in 0.1 eV steps. The optical density displayed in the following figures is defined as $OD = \ln(I/I_0)$.

The structure of teichoic acid and its C1s spectrum is shown in Figure 4.3. Teichoic acid is a component of gram-positive cell wall but is not found in gram-negative cell walls. The spectrum features a strong step at 288 eV with two distinct peaks at 288.0 eV and 289.5 eV. There is no carbon ring in the structure of teichoic acid, so there is no double peak at 285 eV in the spectrum.

The structure and C1s spectrum of peptidoglycan is shown in Figure 4.4. Peptidoglycan makes up the majority of the cell wall in a gram-positive organism. The N-acetylglucosamine and N-acetylmuramic acid (which make up the peptidoglycan) each has a carbon ring structure. These structures account for the double peak between 285-286 eV in the carbon spectrum of peptidoglycan.

The gram character of the cell wall is determined by both chemical and structure differences. The structural differences of cell wall thickness are at 5 nm length scales, below the resolution limit of STXM. Table 4.1 shows two significant differences in the cell wall chemistry, however, that might be detectable in C1s spectra. Teichoic acid is only present in gram-positive cell walls, and peptidoglycan makes up a much greater percentage of gram-positive cell walls than in gram-negative cell walls. The standard spectrum of peptidoglycan shown in Figure 4.4 has a very strong peak at 288.2 eV corresponding to the carboxyl group (COOH) and a double peak at 285 eV that corresponds to the carbon ring structures of N-acetylglucosamine and N-acetylmuramic acid. The relative strength of the 288.2 eV peak in the gram-positive (BC1) cell wall spectrum is much greater than in the gram-negative (CH34) cell wall spectrum, and therefore is consistent with a cell wall that has a greater percentage of peptidoglycan molecules. In addition, lipoteichoic acid, which is only found in gram-positive cell walls, has a spectrum (Figure 4.3) with two strong features at 288.3 eV and 289.5 eV. The 289.5 eV peak is present in cell wall spectra from both the BC1 and the CH34 cells. The 288.3 eV peak, however, lines up better with the BC1 288.3 eV peak.
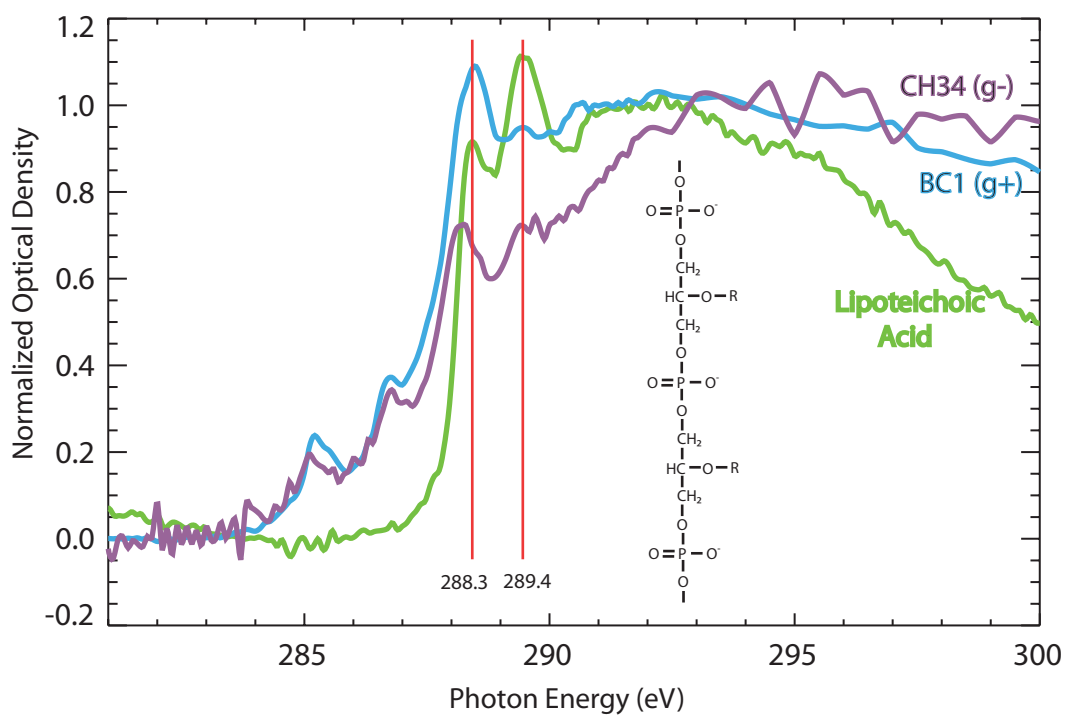
Figure 4.3: Cell wall spectrum from *Clostridium* species BC1, a gram-positive bacterium, *Ralstonia* species CH34, a gram-negative bacterium and lipoteichoic acid. Liposteichoic acid is only found in gram-positive cell walls.
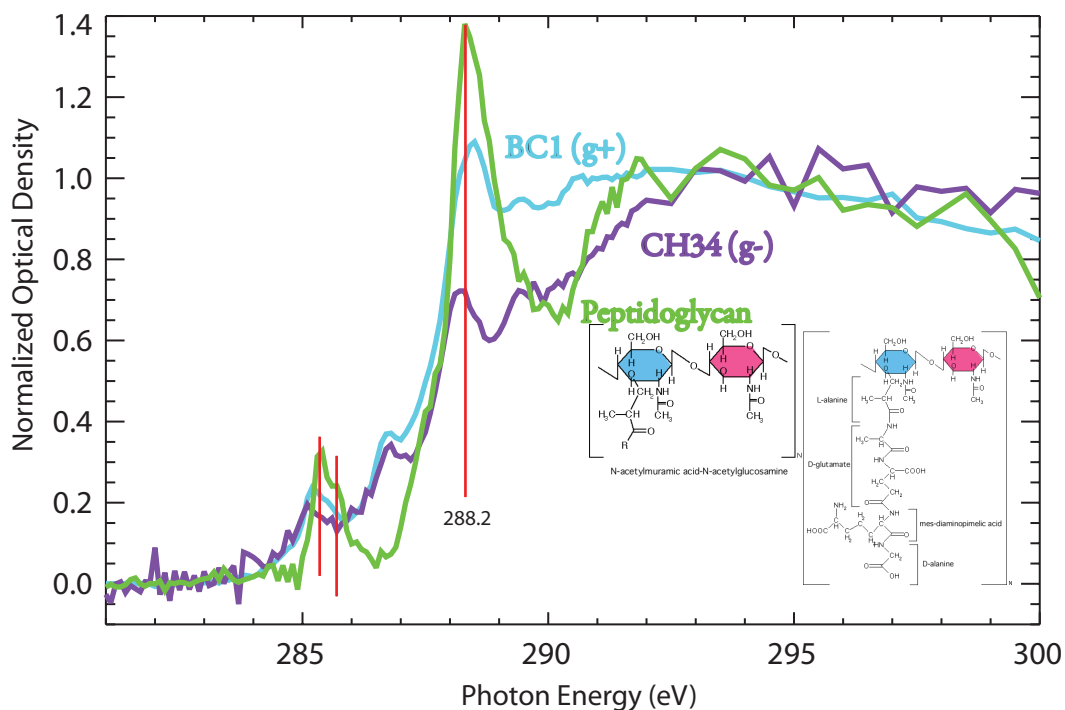
Figure 4.4: Cell wall C 1s spectrafrom *Clostridium* species BC1, *Ralstonia* species CH34 and the polymer peptidoglycan. The structure of peptidoglycan is inset. Peptidoglycan is a linear polymer that makes up more than 50% of the cell wall of gram-positive bacteria and 10-20% of gram-negative cell walls. The units of *N*-acetylglucosamine and *N*-acetylmuramic acid that make up the peptidoglycan chain each have a carbon ring structure, which corresponds to the double peak at 285 - 286 eV.

These two observations do suggest that the position and relative intensity of the carboxyl peak can be used to distinguish gram negative and gram positive bacteria. These distinguishing features, however, need to be measured and confirmed for a large number of different gram positive and gram negative species. In addition, new sample preparation protocols involving cryogenic microtome sectioning are needed to produce thin sections of bacteria that are thick enough to provide contrast, and yet allow STXM spectral imaging of the cell wall in relative isolation from the cell body. Finally, extensive model compound studies of pure compounds and mixtures of cell wall components in solid and liquid states are required, especially to determine how peak intensity is related to relative component composition.

Microbiological research would benefit greatly from a method such as STXM that could distinguish gram positive and gram negative character of individual cells within mixed bacterial colonies and biofilms.

4.2.2   Carbon Storage Polymers

Polyhydroxybuterate (PHB) is a polymer that is produced by micro-organisms in response to conditions of physiological stress. It is used as a form of energy storage to be metabolized when other energy sources become scarce.

PHB is not water soluble, but the similar molecule, β-hydroxybuteric acid is water soluble. Both of these standards were prepared by placing 0.1 g into 100 mL of deionized water and mixed using a vortex mixer. A droplet of 1-2 μL was placed onto a silicon nitride window. The standard spectrum is shown in Figure 4.5. The spectrum is rather featureless. The structure of PHB does not contain any ring structures to produce the peak at 285 eV and there are no carboxyl groups (COOH) to produce a strong feature at 288 eV.

Three different strains of the aerobic biopolymer producer (R. eutropha) were used in the current study. The first, a wild-type R. eutropha, accumulates PHB in well-defined granules within the cell. The second is an engineered PHB-deficient strain. The third strain produces amorphous, or poorly-packaged intracellular forms of PHB.

Figure 4.6 shows cluster images and corresponding cluster component C $1s$ spectra for these three bacterial species. The STXM image of the wild-type R. eutropha shows features within the cells (purple areas) appear to be PHB granules. Applying PCA and cluster analysis to the stack clearly identifies the membrane (green cluster) and spectrum in Figure 4.6. Non-PHB producing R. eutropha (Figure 4.6b) looks considerably different, where cluster analysis identified only two almost identical spectra within the cell.

Although the PHB standard spectrum is relatively featureless, the cluster analysis is able to identify the PHB granules within the wild-type R. eutropha
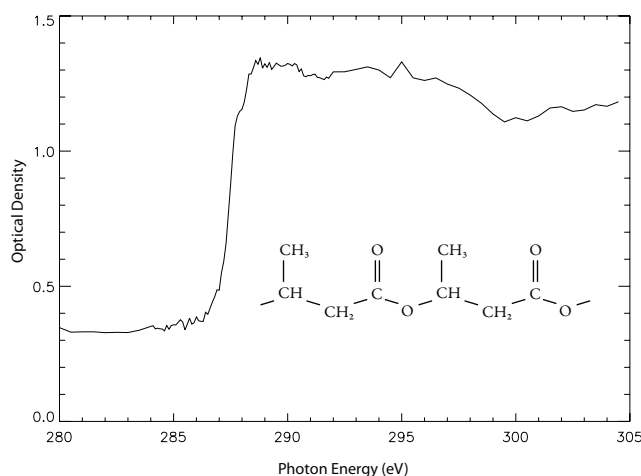
Figure 4.5: Spectrum of the water-soluble β-hydroxybuterate (PHB). PHB is accumulated by some bacteria as a carbon-storage compound. The spectrum has a strong step, but otherwise appears rather featureless.

cell body. In the amorphous-PHB producing cells, it appears that the PHB granules, if present, may be too small to resolve with the 40 nm beamspot. In order to determine the particular spectral and chemical features that produces unique clusters for PHB granules and the cell body additional model compound data is required.

4.2.3 Spore-Forming Bacteria

The bacteria species *Bacillus subtilis* and *Clostridium* BC1 are both gram-positive and both form spores. The formation of spores is a defense mechanism to resist heat, dessication and radiation. When faced with poor conditions, the bacterium forms a secondary membrane of peptidoglycan around a copy of its DNA. As the spore coat matures and hardens, the remainder of the cell dies. When conditions improve a new cell is grown from the spore. Dipicolinic acid and Ca-dipicolinate, shown in Figure 4.7, are major components of spores.

STXM was used to identify the spores and endospores in the bacteria samples. Transmission electron microscopy was performed to complement and aid in interpretation of results of STXM analysis. This work was part of a project to determine the effect of stress in the form of desiccation, metals and radiation on bacterial cells and to track the chemical evolution of the subcellular features.

Bacterial cultures of *Clostridium* and *Bacillus subtilis* were prepared. Growth

73

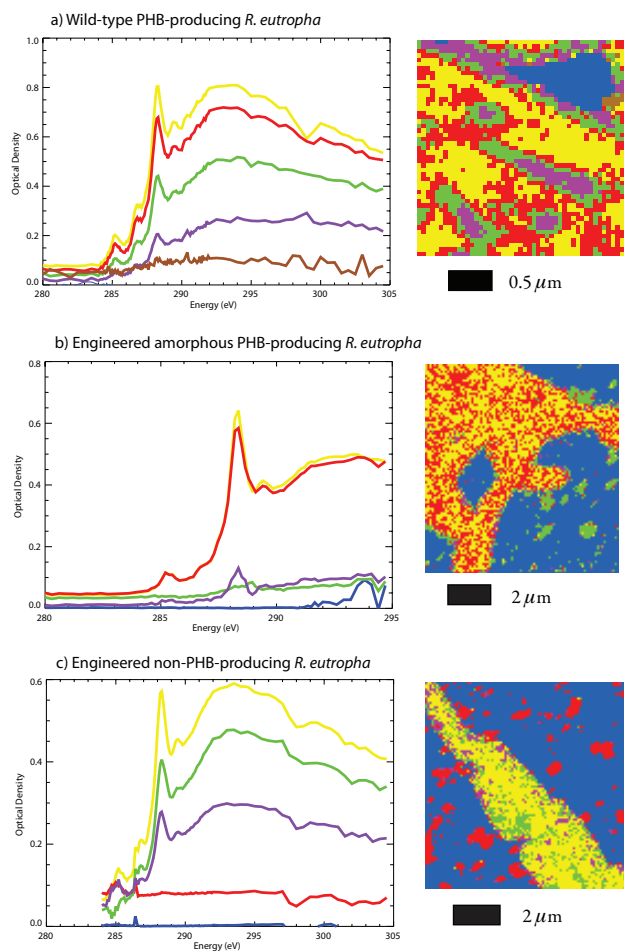Figure 4.6: STXM of three strains of *Ralstonia eutropha*, a PHB-accumulating bacterium. a) Wild-type *R. eutropha*, which accumulates well-defined granules of PHB within the cell. b) A PHB-deficient strain of *R. eutropha*. c) A strain of *R. eutropha* that produces amorphous, or poorly-packaged, PHB. The cluster analysis identifies a struture within the wild-type cell that appears to be PHB granules.
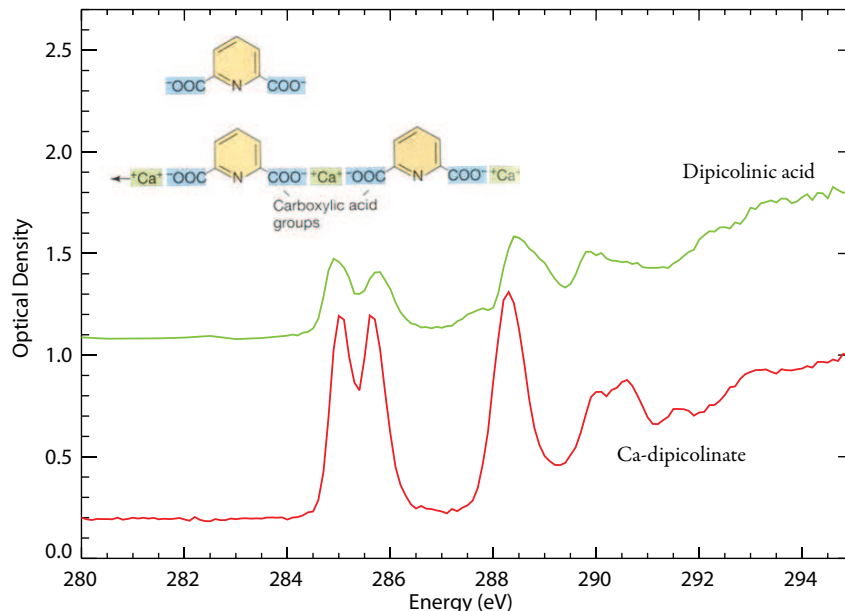
Figure 4.7: Dipicolinc acid and Ca-dipicolinicate are major constituents of spores. Spectra from pure samples of dipicolinic acid and Ca-dipicolinicate show a strong feature at 285 eV.

media was optimized to promote sporulation by the aerobic (*B. subtilis*) and anaerobic (*Clostridium*) spore formers. (*Clostridium* and *Bacillus*) were collected at sporulation stages 0-VII [41] centrifuged at $5000g$ to recover whole cells, and washed in water several times to eliminate the growth medium from the sample. The cells were dried on silicon nitride windows. The outboard STXM at beamline X1A at NSLS was used to examine the cells at the C K-edge from 280 to 310 eV. High-resolution scans were performed (5×5 μm images, 50 nm resolution at 0.1 eV steps). Finally, pure compounds (e.g. nucleic acids, proteins, phospholipids, glycan tetrapeptides and polypeptides, acid polysaccharides and spore constituents dipicolinic acid and phosphoglyceric acid) were analyzed by STXM to obtain standard XANES spectra to identify the chemical species obtained from cluster analysis.

Analyses of pure peptidoglycan and exopolysaccarides revealed extensive chemical modification due to x-ray damage. Sample damage was determined by taking several point spectra on the same spot on the sample and noting a change in the spectra over the series. While the pure samples of peptidoglycan and exopolysaccharides showed extensive damage, this did not occur while imaging whole cells and associated structures.

75

Cluster analyses of both *Clostridium* sp. and *Bacillus subtilis* clearly identify distinct cluster spectra for endospores. These spectra indicate that the endospore is chemically different from the vegetative cell. A strong feature at 285 eV in the endospore cluster spectrum matches with the features observed in the spectra of pure dipicolinic acid and Ca-dipicolinate samples. Figure 4.8 shows cluster maps and the associated cluster spectra for *Bacillus* subtilis with endospores (a) and spores (b). The relative height of the 285 eV peak and the 288 eV peak indicates the presence of the (endo)spore. The ratio of the 285 eV peak height to the 288 eV peak height for the endospore spectrum in the 72 hour sample is 0.56 while for the vegetative cells the ratio is 0.26. This ratio holds for the 96 hour *Bacillus* sample, with ratios of 0.56 and 0.29, respectively. For the *Clostridium* sample, shown in Figure 4.9, the cells are in an earlier stage of sporulation, but the ratio of peaks follows a similar trend. These results demonstrate a new method to identify spores and endospores in single bacterial cells. It is important to note that the earlier stages of sporulation do not produce markedly different spectra when compared to later stages of sporulation, and therefore it is not possible to identify stages of sporulation using this method.

The images of the *Clostridium* sp. sample also show the presence of exopolysaccharide (EPS) surrounding the cells. The cluster analysis indicates that EPS is spectrally different from both the spores and the vegetative cells. Specifically, the height of the 288 eV peak is diminished compared to the total step height in the EPS spectra for both the 48-hour and 72-hour samples.

Cluster analysis of STXM data on the same samples identified unique C $1s$ absorption features in the endospore not present in the vegetative cells, as seen in Figures 4.8 and 4.9. Endospores of *Bacillus subtilis* exhibited similar absorption features as did exospores. The C1s XANES of pure chemical standards implicate the pyridine salts in the spores as the likely molecular signature revealed by cluster analysis. In addition, TEM shows extensive exoploysaccharide accumulation around cells of *Clostridium* sp.

4.3   Studies of Iron-Bacteria Interactions

Ferrihydrite is a ubiquitous naturally-occurring nanoparticulate iron hydroxide which can also serve an important model system for the study of biofilm-nanoparticle interactions to understand how microbial processes affect the fate and transport of engineered nanoparticles. The following two subsections present carbon K-edge and iron L-edge data to examine the differences in iron chemistry due to the interaction with *Clostridium* and the exopolysaccharide (EPS) material that leads to the formation of biofilms.

a) *Bacillus subtilus* at 72 hour growth

b) *Bacillus subtilis* at 96 hour growth
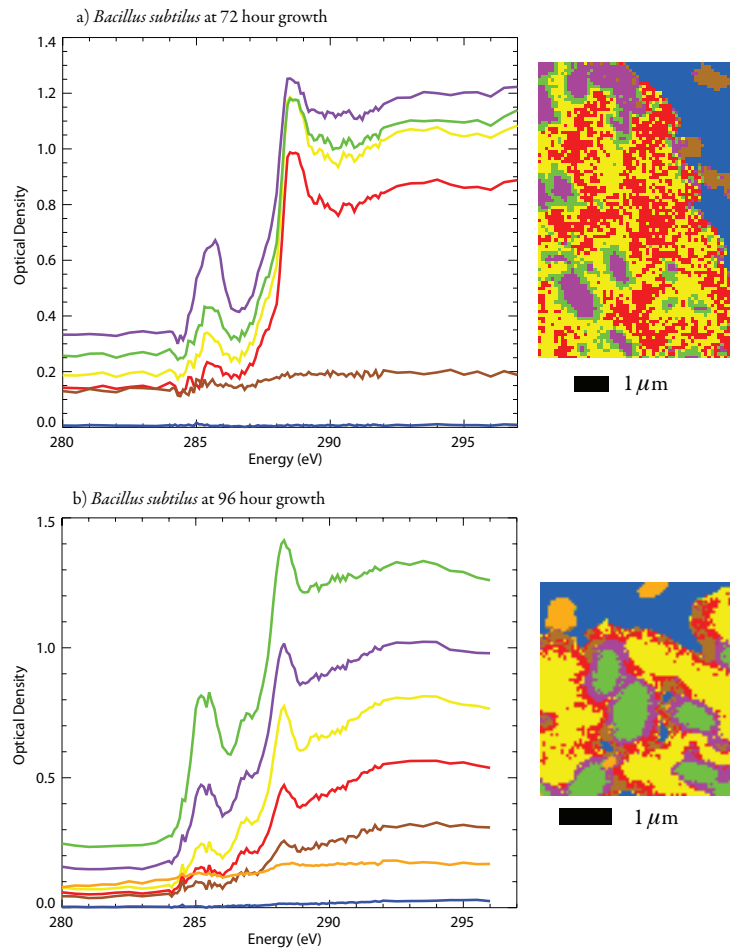
Figure 4.8: Cluster map and spectra of *Bacillus* subtilis with spores. (a) *Bacillus subtilis* at 72 hour growth (showing endospores) and (b) 96 hour growth (showing spores) both indicate that the spore can be identified as different from the vegetative cell by the strong feature at 285 eV, which is indicative of the presence of dipicolinic acid which has strong 285 eV features, as seen in Figure 4.7.
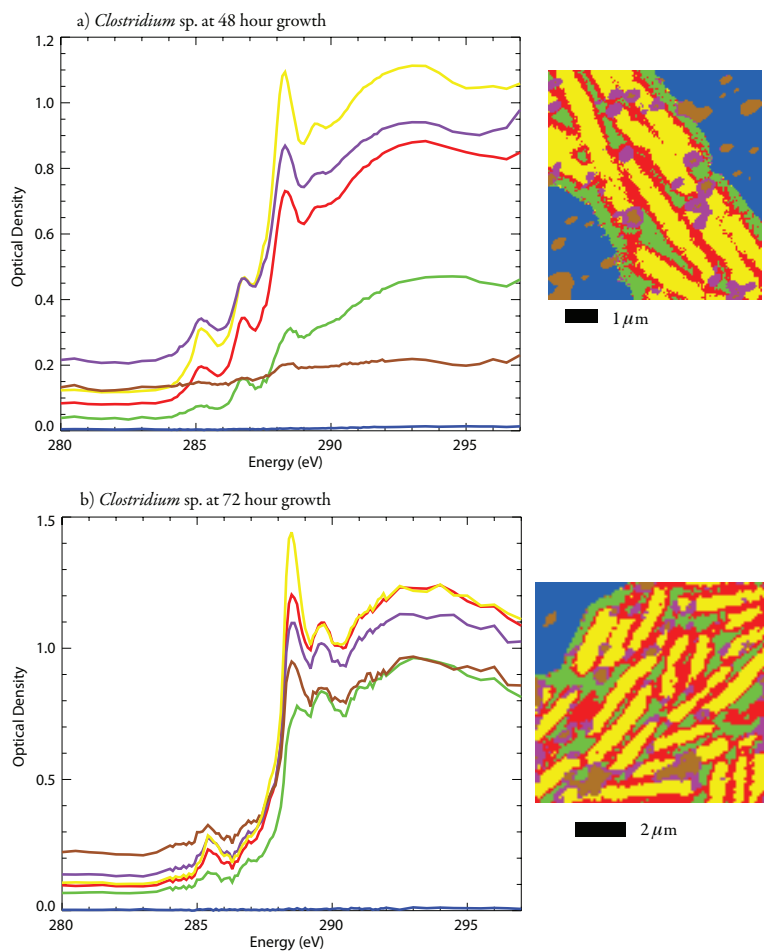
Figure 4.9: Cluster map and spectra of *Clostridium* sp. with endospores. The endospore was identified as different from the vegetative cell by the stong feature at 285 eV, which is indicative of the presence of dipicolinic acid and Ca-dipiconicate, which both have strong 285 eV features, as seen in Figure 4.7.

4.3.1 Iron-Bacterial Interactions Studied at the Carbon K-Edge

The interactions of sporulating bacteria, important for many mineral and con-taminant transformations in the natural environment, with iron (hydr)oxides was examined using STXM at the carbon K-edge. The anaerobic fermentative bacterium *Clostridium* species BC1 was grown in the presence of ferrihydrite to determine what effect the mineral has on the chemistry of the subcellular features, specifically exopolymeric substances (EPS). Samples were prepared at 48 hours and 6 day growth. Figure 4.10(a) shows the results of using cluster analysis on the 48-hour sample, with a carbon K-edge false-color map inset on the absorption spectra correlated to the colors in the map. The analysis picked out shifts in the C=O peak around 288 eV. The yellow cluster is the bacterium, the red is most likely the exopolymer, and the green and purple clusters correspond to areas where the ferrihydrite is interacting with the ex-opolymer at the iron oxide-organic carbon interface. Figure 4.10(b) shows an electron micrograph of the *Clostridum* species grown in the presence of ferrihydrite at pH 3.

The scanning electron microscopy analysis supports the results of the STXM study, providing evidence of the EPS coating the ferrihydrite particles. The STXM measurements provide information related to the chemical interaction of the EPS with the ferrihydrite particles. The EPS is known to play a role in preventing the dissolution of the ferrihydrite at low pH due to passivation by the EPS, specifically organic carbon and phosphate sorption, due to phosphate groups present in the EPS.

4.3.2 The Iron L-Edge

The iron mineral standards were mixed in water and allowed to air dry on a silicon nitride window. The Fe L_2 and L_3 absorption edge spectra (700-730 eV) were taken on the X1A2 branch using the segmented silicon detector and the high energy slits. Figure 4.11 compares the Fe L_3 absorption edge spectra of the two model $Fe_{(III)}$ mineral compounds goethite and ferrihydrite, and ferrihydrite after having been added to a suspension of actively growing Clostridium bacteria. The peak at about 711 eV indicates that the minerals goethite and ferrihydrite are primarily made of iron in the 3+ oxidation state. The peak at 709 eV indicates iron in the 2+ oxidation state. The spectrum of the biotransformed ferrihydrite shows that the fraction of the mineral in the 2+ oxidation state is much greater than in the standard sample of ferrihy-drite. These results show the extraordinary reductive ability of the Clostridium species. Furthermore, the high spatial resolution of STXM will enable novel

a) Cluster map and spectra of BC1 and ferrihydrite

b) SEM of BC1 and ferrihydrite
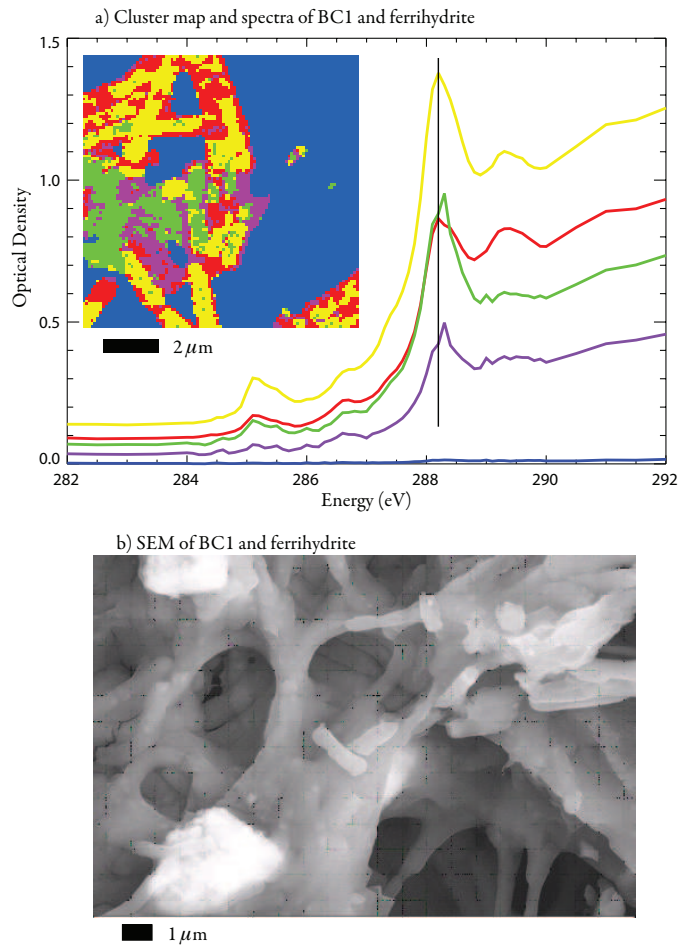
Figure 4.10: a) Carbon K-edge scanning transmission spectromicroscopy (STXM) of the interaction of *Clostridium* sp. with ferrihydrite. Inset shows a false-color map of the bacterial cells and EPS-coated iron oxide with corresponding K-edge absorption spectra. b) Scanning electron micrograph of *Clostridium* sp. bacterial cells grown in the presence of ferrihydrite for 48 hours. The whole bacterial cells are clearly visible embedded in EPS surrounding the ferrihydrite particles (large bright particles).
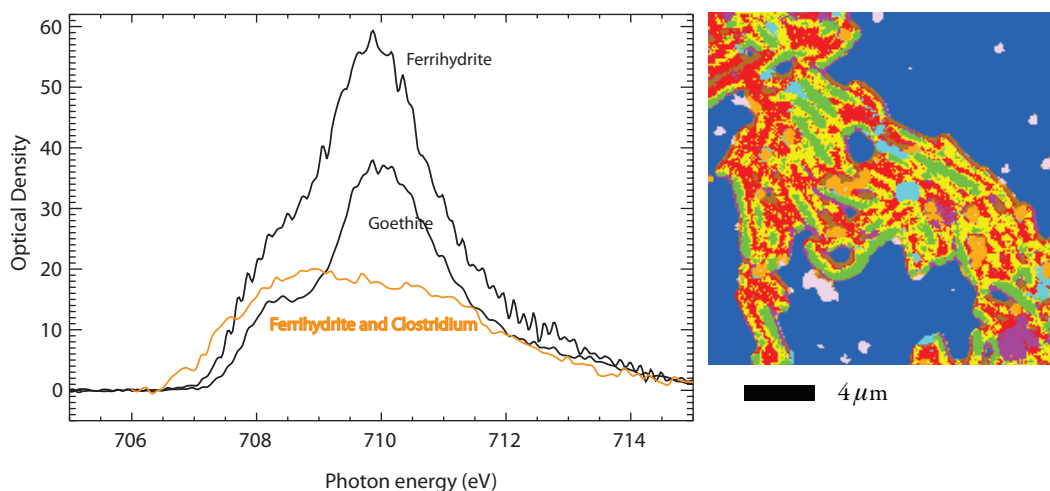
Figure 4.11: The Fe L_3 absorption edge spectra of iron mineral standards goethite and ferrihydrite. These spectra indicate the valence state of the iron mineral. The peak at about 711 eV indicates that the minerals goethite and ferrihydrite are primarily made of iron in the 3+ oxidation state. The peak at 709 eV indicates iron in the 2+ oxidation state.

investigations into highly reactive minority phases that are not detected using bulk spectroscopy and diffraction methods. These minority phases, such as the case of biotransformed ferrihydrite, can dominate the reactivity of a soil toward contaminant radionuclides and metal ions.

# 4.4 Uranium Speciation and Uptake in Bacteria

While Section 4.3 showed that it is possible to identify the valence state and therefore the binding environment of iron by using the iron absorption edge, it may also be possible to infer metal binding from the carbon absorption edge spectra. In this section we will show that x-ray spectromicroscopy may be used to elucidate the functional groups at the bacterial cell surface that are involved in soprtion of radionuclides such as uranium and toxic metals such as lead.

Studies of the interaction of uranium with microorganisms have identified reduction mechanisms that alter chemical speciation [42], solubilization mechanisms due to production of carbonate [43] and biosoption mechanisms resulting in biocolloid formation [44]. As determined by potentiometric titration of

various bacterial species, the carboxylate group whould be the predominant functional group responsible for uranyl ($UO_2{}^{2+}$) uptake at pH 5 [45].

The bacterial cell wall is negatively charged, and in slightly alkaline pH solutions aqueous uranium is predominantly present as anionic species. Therefore these anionic uranium species should not necessarily bind to bacterial cells by strictly electrostatic arguments. However, there is evidence that uranium forms a carbonato and calcium complexes that may mask charge and thereby make bacterial sorption of uranium a favorable reaction. The carboxylate anion is the deprotonated form of carboxyl functional groups. Potentiometric titrations provide extensive evidence that metal ions an dradionuclides overcome electrostatic constraints to form complexes with the carboxyl functional groups at the bacterial cell surface. STXM C K-edge spectroscopy could provide powerful insights into the formation and occurrence of U-carboxyl complexes at the cell surface by carefully analyzing the 288 eV peak of the carbon spectrum.

The bacteria examined were the gram-negative bacterium *Pseudomonas fluorescens* and the gram-positive bacterium *Bacillus subtilis* These two species represent bacteria that coexist in soil microbial communities, but they possess very different cell wall structures and surface functional group distributions. Data were gathered from the C K-edge XANES spectra of cells before and after exposure to uranium. Shifts of features within XANES spectra can reveal infomation about the uranium bonding environment, and STXM images provide the spatial information neccessary to determine regions of radionuclide accumulation.

Studies of the interaction of uranium with microorganisms have identified reduction mechanisms that alter chemical speciation [42], solubilization mechanisms due to production of carbonate [43] and biosoption mechanisms resulting in biocolloid formation [44]. As determined by potentiometric titration of various bacterial species, the carboxylate group whould be the predominant functional group responsible for uranyl ($UO_2{}^{2+}$) uptake at pH 5 [45].

Spectra obtained at X1A from analysis of cells of the gram-negative bacterium, *Pseudomonas fluorescens*, imaged at and below the C K-edge after exposure to uranium is presented in Figure 4.12. The image clearly shows strong absorption at the C-edge throughout the entire cell. Below the edge, there is weaker absorption, with a distinct area of strong absorption within the boundary of the cell margin. This region is rich in inorganic material and may be enriched in uranium or some other element such as phosphorus. The spectra shown in Figure 4.12 shows a distinct shift in the C K-edge XANES from 288.5 eV before uranium exposure to 288.0 eV after uranium exposure. There is no shift in the resonances at 285 eV from the C=C group which is
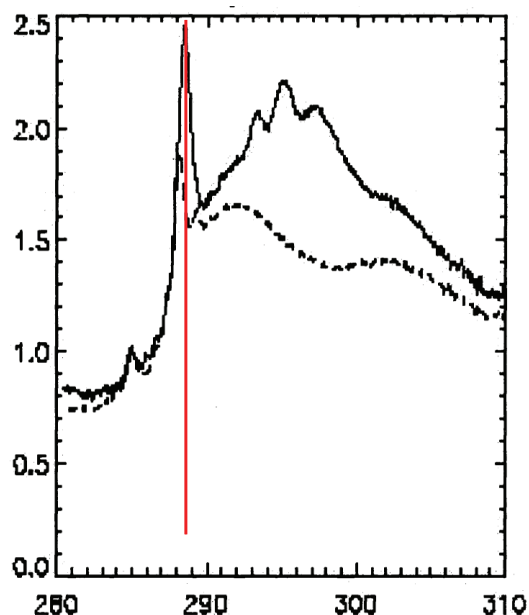
Figure 4.12: Carbon K-edge spectrum of *P. fluorescens* exposed to U (dashed line) and unexposed to U (solid line)

expected given that these carbon atoms are present within ring structures and therefore its electronic structure should not be effected by the formation of uranium-carboxyl complexes. These resonant features provide a very useful internal energy calibration and verification that the shift in the carboxyl peak is significant, suggestion that uranium forms complexes with carboxyl groups at the gram-negative cell surface. In contrast, the same analysis STXM images and cluster spectra of *Bacillus subtilis*, shown in Figure 4.13, the gram-positive bacterium, shows no peak shift.

One possible arrangement for the binding of uranium to the gram-negative cell is bidentate bonding to carboxylate and the neighboring amine group. This type of association may account for our preliminary results with *P. fluorescens*. The *P. fluorescens* that we have analyzed is a good canidate for the study of strictly surface sorption, as opposed to bacterial species and conditions which have been shown to produce uranium precipitates. Transmission electron microscopy performed in collaboration with Dr. Terrence Beveridge at The University of Guelph shows how uranium concentrates both at the outer membrane and in the periplasmic space of *P. fluorescens* when the cells are exposed to U at pH 5. The TEM observations are consistent with the C K-edge spectra and STXM images which provide evidence that uranium accu-
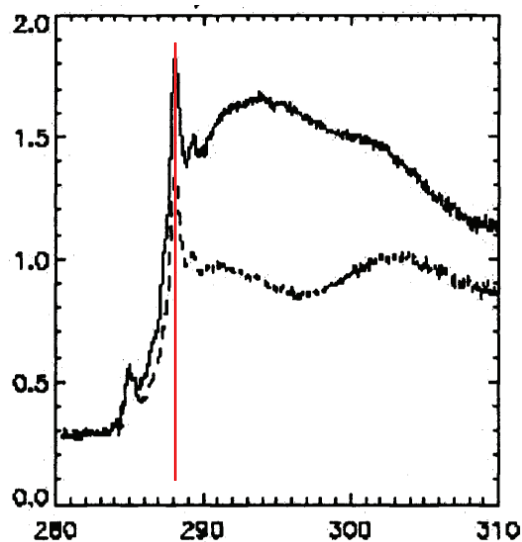
Figure 4.13: Carbon K-edge spectrum of *B. subtilis* exposed to U (dashed line) and unexposed (solid line).

mulation in the cell-surface region is at to a significant extent due to binding between uranium ions and carboxyl surface functional groups.

4.5 Nickel Binding and Precipitation by Resistant Microorganisms

The density of organic functional groups capable of binding metal ions at the cell surface is an important factor controlling the flux of metal ions across the cell membrane. The proportional distribution of different functional groups at cell surfaces have been assumed based on reconstructions of digested cells, and more recently, estimated based on x-ray photoelectron spectroscopy studies for a large number of bacteria species. Bacterial cell walls have a net negative charge due to amino, phosphoryl and carboxyl groups. The metal binding capacity of gram-positive bacterial cell surfaces present the carboxyl groups of peptidoglycan and the phosphorylgroups of teichoic acids. In the case of gram-negative bacteria, the polar heads (phosphoryl groups) of phospholipids in the membrane and lipopolysaccharides in the cell wall are responsible for binding metals. Mass-balance and potentiometric titrations of bacterial suspensions have been used to construct models of metal ion complexation at the cell surface and predict metal ion uptake. Synchrotron-based STXM studies of

84

hydrated samples of soil biomass [46] and amino acids [35] have been used to directly characterize functional group chemistry with the spatial resolution necessary to be a single cell technique. This work applies STXM to characterize Ni complexation at the cell surface of metal resistant bacteria strains.

Ni-resistant bacteria employ a variety of mechanisms to expel metal ions from the cell body including metal ion efflux pumps and metal transporter complexes. Electron microscopy studies have revealed exquisite detail of sub-cellular biostructures following active Ni detoxification and accumulation, revealing in some cases the formation of nanoscale precipitates within and associated with bacterial cell walls. Ni(II) is both required as a micronutrient and toxic in excess, without being subject to bacterial redox chemistry. Ni(II) as with other micronutrients that are toxic at high levels is closely regulated for both uptake and efflux.

Unique contributions of this work include using STXM to characterize metal-organic complexation by measuring π^* transition energies for metal-carboxy complexes. The work combines STXM C and O 1s microspectroscopy and darkfield imaging of single bacterial cells to distinguish between passive and active metabolic (biodirected reactions) interactions with Ni ions at cell surfaces. Spectroscopic evidence that Ni(II) is binding to carboxy (likely amino-acid) groups at the cell surface. Darkfield imaging and O NEXAFS show precipitate spatial distribution and precipitate type, respectively. This work ultimately provides the chemical identity, stoichiometry and spatial distribution of Ni complexes and precipitates, information which is necessary for coupling in silico models of metabolic pathways with models to predict bacterial behavior in natural and industrial processes.

Experimental Details

Two nickel-resistant bacterial species used in this study. The Ralstonia CH34 strain, which was described in section 4.2.1, was isolated from a zinc smelter operation and has resistance to a wide range of toxic metal cations. The second strain (FRC) was isolated from soils from a uranium and metal contaminated soil from Oak Ridge, Tennessee. Prior to isolating FRC the soil was exposed to high levels of nickel in soil column experiments conducted at Brookhaven National Lab. The FRC strain is capable of growing in the presence of 6 mM nickel-containing aqueous solutions, and has genetic characteristics similar to the *Pseudomonas* genera of bacteria.

To prepare the samples for STXM, bacterial cultures prepared with and without Ni were rinsed using two distilled water rinses and centrifugation in order to dilute the media. The spectromicroscopy data sets are generally composed of 10,000 spectra, the components of which may not be fully known. To

deal with this complexity, the data is first reduced by rewriting each spectrum as a linear combination of its most significant principle components, which are the eigenvalues of the covariant data matrix. The program PCA GUI (http://xray1.physics.sunysb.edu/data/software.php) then uses cluster analysis to group spectra based on the similarity of their linear combinations as described in Section 3.3.

To eliminate a strong feature that would otherwise dominate the clustering of the data, such as the σ^* peaks around 295 eV, the energy range can be restricted to exclude that feature. If the strong σ^* peaks are present while clustering the data, the clustering algorithm will produce clusters that differ only in the height of that peak, rather than slight shifts in the position of the pre-edge peaks. In some cases it may be helpful to select an energy range that includes a only a single peak of the spectrum. This eliminates the dependence of the clustering algorithm on spectral features that are not of interest. But after the analysis, normalization of the peak for comparison with other spectra is impossible without the absorption edge step. The pixels belonging to each cluster must be averaged over the original energy range.

Peak fitting of C and O 1s spectra was performed using Athena. The carboxyl peak (288 eV) was fit using three peaks plus a fourth peak for the lower energy shoulder at 287.5 eV. The position and width of the three peaks was set using the nickel-free bacteria sample spectra. Then the nickel-exposed sample spectra were fit using the same three peaks and allowing the height to change. As shown in the Figures 4.17 and 4.16 of the results section, nickel binding to the carboxyl group causes an upward shift in the corresponding peak at 288 eV. Because only a fraction of the carboxyl groups are bound to nickel, instead of a simple shift in the peak position there will be a shift in the shape of the peak toward higher energy. There is still some component of the lower energy nickel-free carboxyl group present in the spectrum. The shift to a larger proportion of nickel-bound carboxyl groups can be shown by the relative heights of the 288.0, 288.3 and 288.6 eV lorentzian peaks used to fit the carboxyl peak.

X-ray absorption spectroscopy measurements were performed at the NSLS beamline X27A microprobe equipped with a Si(111) double-crystal monochromator. Fluorescence-yield Ni K-edge XAFS data were collected using a 13-element energy-dispersive germanium detector (Canberra). Energy calibration was checked by collecting the transmission spectrum of a Ni metal foil before and after each set of energy scans. The first inflection point of the K-edge of the Ni metal foil was assigned as 8333 eV. XAFS spectra were collected over the energy range of 8.2-8.9 keV. Averaging, normalization, and background subtraction of the raw XAFS spectra were performed with Athena Each av-

eraged XAFS spectrum was separated into two regions, the X-ray absorption near-edge structure (XANES) spectral region and the extended XAFS (EXAFS) spectral region. XANES spectra (8320-8370 eV) were normalized and compared for qualitative information. EXAFS oscillations were isolated with a spline function and converted from energy to k-space ($k = 2m_e(E - E_0)/h^2$, where m_e is the mass of the electron, E is the energy, E_0 is the energy at $k = 0$, h is Planck's constant, and E_0 was defined as 8349 eV based on fits of Ni(II)-containing model compounds). Two to four transmission scans for model compounds and 10 fluorescence scans for Ni-biomass samples were collected out to $k = 10^{-1}$. Beam-induced sample changes were not observed in the XANES or EXAFS region of sequential spectra for any of the samples, indicating no detectable change in the coordination environment of Ni(II) during data collection. Initially, the k^3-weighted EXAFS spectra of the model compounds nickel(II) hydrous oxide, nickel(II) oxide, and aqueous Ni were fit with phase shift and amplitude functions generated by FEFF7 These fit results were used to test the theoretical phase shift and amplitude functions that were later used to fit unknown Ni-biomass samples. Values for coordination number (CN) and distance to scattering atoms (R) were determined from least-squares fits of the EXAFS and the Fourier-filtered EXAFS of each shell. The Debye-Waller values (σ^2) and the accuracy of parameters varied during the least-squares fits of Ni-biomass samples ($R \pm 0.01\mathring{A}$ 1st shell; $R \pm 0.02\mathring{A}$ for more distant shells) were derived from a comparison of the fitted parameters of the model compounds with inter-atomic distances reported in X-ray diffraction refinements of the structures of nickel(II) oxide and Ni(II) hydroxide

Results of Nickel Binding in Bacterial Samples

Figure 4.14 shows a representative carbon 1s NEXAFS spectrum of the gram positive bacterial strains studied. The edge step and predominant electronic transitions were modeled with an error function and five lorentzian functions (labeled A-E in Figure 4.14) were used to fit the peaks. A spectroscopic survey of organic model compounds that comprise the dominant building blocks of bacterial intercellular and cell membrane regions, was used to identify the different peaks in the bacterial spectrum. These compounds included teichoic acid, lipoteichoic acid, amino acids, and phospholipids (phosphoglyceric). Kaznacheyev et al (2002) confirmed the relative position of the π^* and σ^* energy transitions responsible for the peaks observed for a series of amino acids [35]. The peak-fitting methodology is described in the experimental section above. Peaks A-C and E represent inter-molecule carbon species not capable of binding metal ions Amino groups provide excellent metal-binding sites, but do not fall within the carboxyl group energy range and do not have a pronounced en-

ergy peak [35]. The remainder of this work will focus on the spectral features corresponding to inter-molecular carbon species capable of binding metal ions, namely the carboxyl groups.

The carboxyl functional group transitions of the model compounds fall within the energy range 288-289 eV. These functional groups represent the highest metal binding capacity of carbon-containing functional groups within the cell membrane and surface region. Other carbon species which have transitions within this range do not interfere or swamp out the signal from the carboxyl group chemistry.

Figure 4.15 shows how the position and width of the carboxyl spectral peak varies within the CH34 gram-negative bacterium. Fits of the bacterial spectra reveal that this peak in each case represents a superposition of a range of carboxyl functional groups. An inherent full width at half maximum (FWHM) of 0.63 ± 0.03eV was observed for the π^* transition of the five model compounds containing a single carboxyl group. Fixing the FWHM to the value of a single carboxyl group, the superposition of the carboxyl peak in the bacterial spectra require two to three approximately equally spaced Lorentzian functions. The centroids of the three peaks occur at 288.0, 288.3 and 288.6 eV.

Figures 4.16 and 4.17 show the C K edge spectra of Ni-organic model compound complexes. In each case the pronounced peak corresponding to the carboxyl π^* transition shifts to higher energy when the Ni complex is present. Although the carboxyl peak position varies depending on the identity of the neighboring side chains, the relative shift of the carboxyl peak when bound to Ni(II) is constant for the four model compounds measured at 0.3 ± 0.05eV. It is also important to note that the FWHM remains constant 0.63 ± 0.03eV in the presence and absence of Ni.

The C1s spectra of CH34 bacteria with and without Ni present are shown in Figure 4.18. The top figure (a) shows the spectrum from the body of a CH34 cell that was in the resting state before the nickel was added. The spectrum corresponds to the yellow cluster in the cluster map of the sample shown in (b). The spectrum in (c) is from the body of a CH34 cell that was grown in the presence of nickel. The spectrum corresponds to the yellow cluster in (d). The spectra were fit using four peaks with set peak positions of 287.6, 288.0, 288.27 and 288.7 eV. The peak height was allowed to vary. Shown inset in Figure 4.18 are the resulting peak heights used for the fit, normalized to the height of the 287.6 eV peak. The ratio between the 288.0 and 288.27 eV peaks show a shift to higher energy for the sample that was grown in the presence of nickel. This indicates that the nickel was forming complexes with the carboxyl group inside the cell only in the case where the organism was actively involved in the nickel uptake.
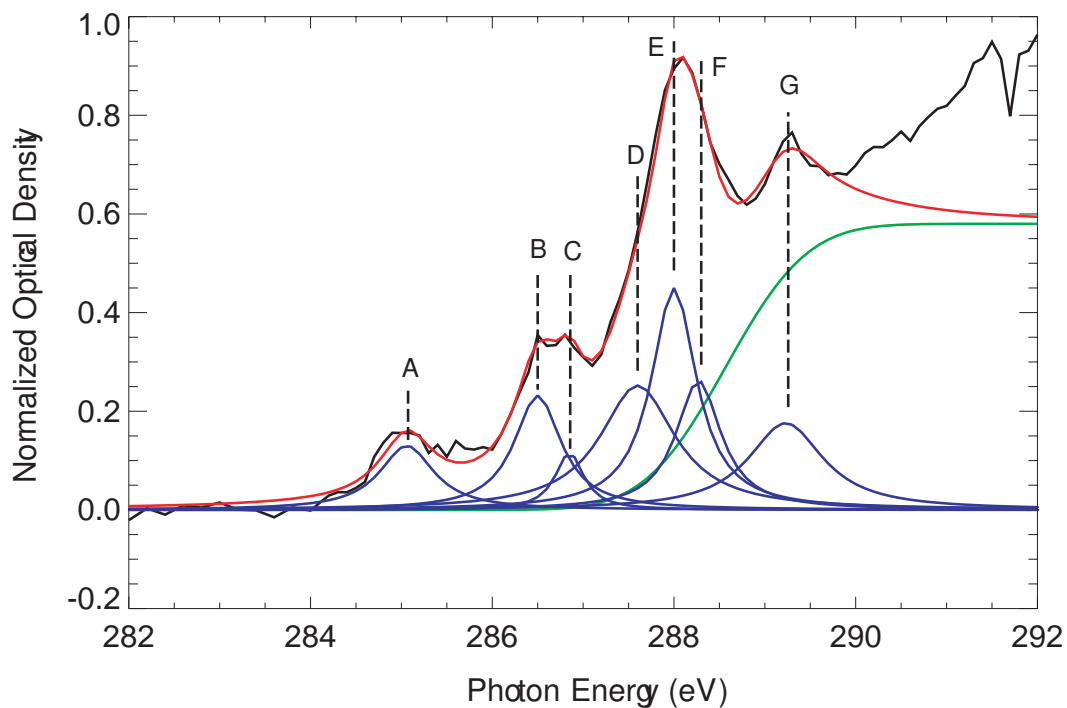
Figure 4.14: Representative STXM C 1s NEXAFS spectrum of a 24-hour CH34 cell grown without the presence of Ni. The spectrum is fit using Lorentzian functions for the peaks and Error function for the step from 275-291 eV. The peaks (A-G) are labeled according to carbon species coordination and assigned electronic transition.
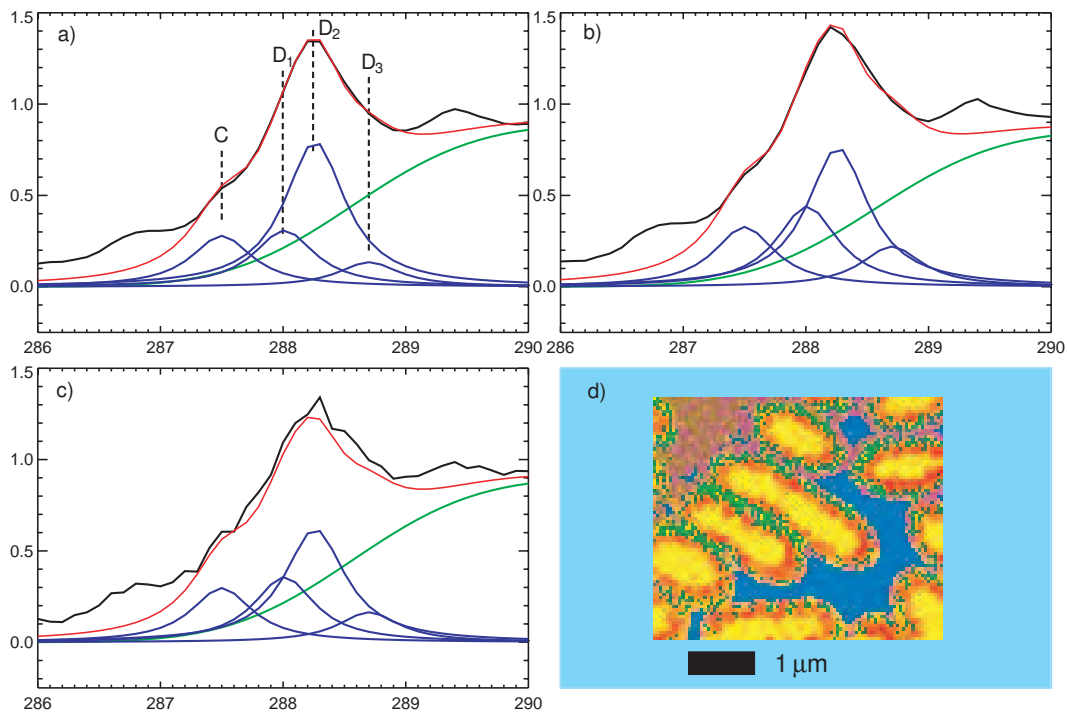
Figure 4.15: The carboxyl peak is fitted with three peaks for three regions of the CH34 bacterium. Spectrum (a) is representative of the body of the cell, averaged over the yellow pixels in panel (d). Spectrum (b) is the cell wall region of the cell, corresponding to the red pixels in (d). Spectrum (c) is the region outside of the cell, containing extrapolysaccarides produced by the cell, corresponding to the green pixels in (d). The peak fits reveal that this peak can be represented in each case by a superposition of a range of caboxyl functional groups. A full width at half maximum (FWHM) of 0.63 ± 0.03eV was observed for the π^* transition of five model compounds containing a single carboxyl group. Fixing the FWHM to the value of a single carboxyl group, the superposition of the carboxyl peak in the bacterial spectra require two to three approximately equally spaced Lorentzian functions. The centroids of the three peaks occur at 288.0, 288.3 and 288.6 eV.
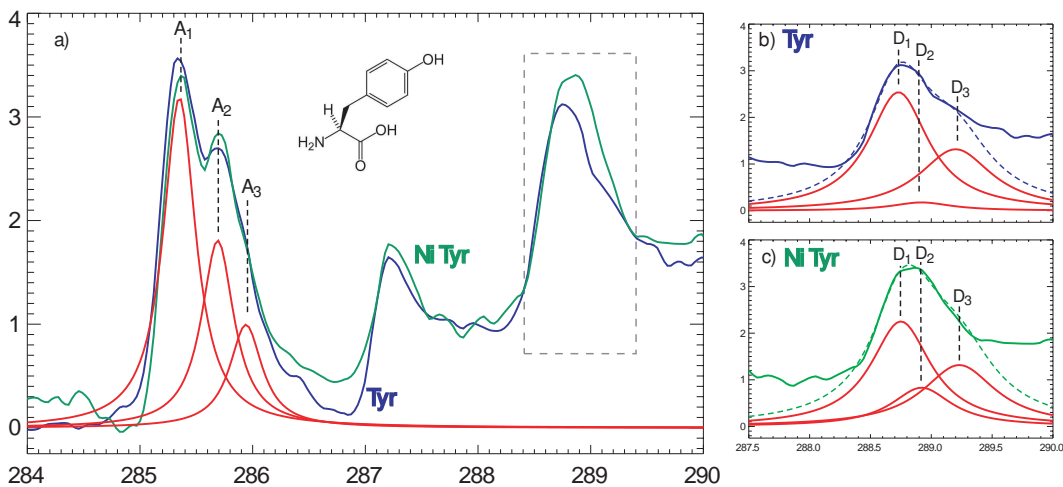
Figure 4.16: Carbon 1s spectra of a sample of tyrosine and the compound Ni-tyrosine. The peaks in the region 285-286 eV correspond to the ring structure (see inset) of tyrosine. These peaks are not affected by the complexation of nickel. Panels (b) and (c) show a peak fit of the carboxyl region of the tyrosine and Ni-tyrosine, respectively. The Ni-tyrosine complex has a larger component of the 289.3 eV component.
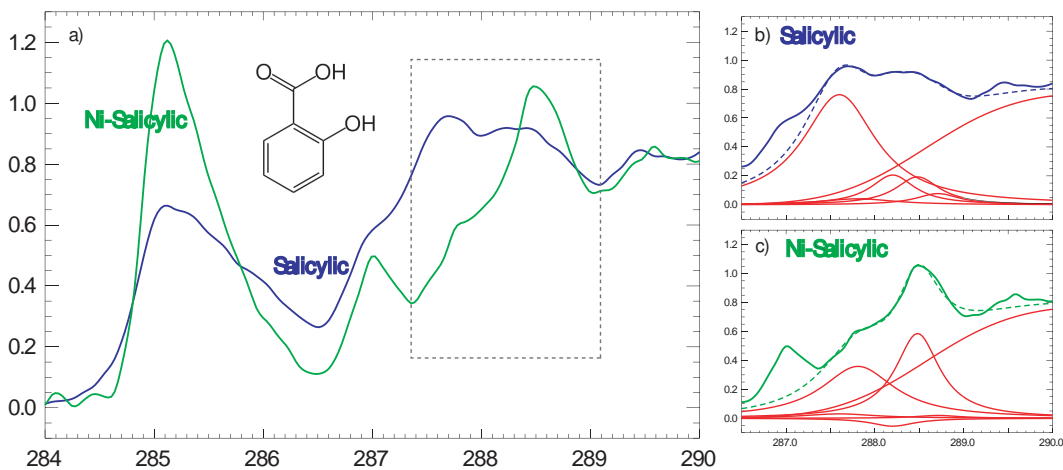
Figure 4.17: Carbon 1s spectra of a sample of salicylic acid and Ni-salicylicate. Panels (b) and (c) show that the component of the carboxyl peak at 288.5 eV is greater in the Ni compound.

Figure 4.18: A comparison of CH34 grown in the presence of Ni (c),(d) with CH34 rinsed and then Ni added (a),(b). The spectrum is an average over the yellow pixels, associated with the cell body. The fits of the carboxyl peak show that there is more nickel binding within the cell for the sample that was grown in the presence of Ni.

4.5.1 Dark Field Imaging of Nickel Precipitates

We know from electron microscopy studies that nickel precipitates are formed by the interaction with the living cell. These precipitates will scatter strongly, and so dark field x-ray imaging can be used to identify the areas of 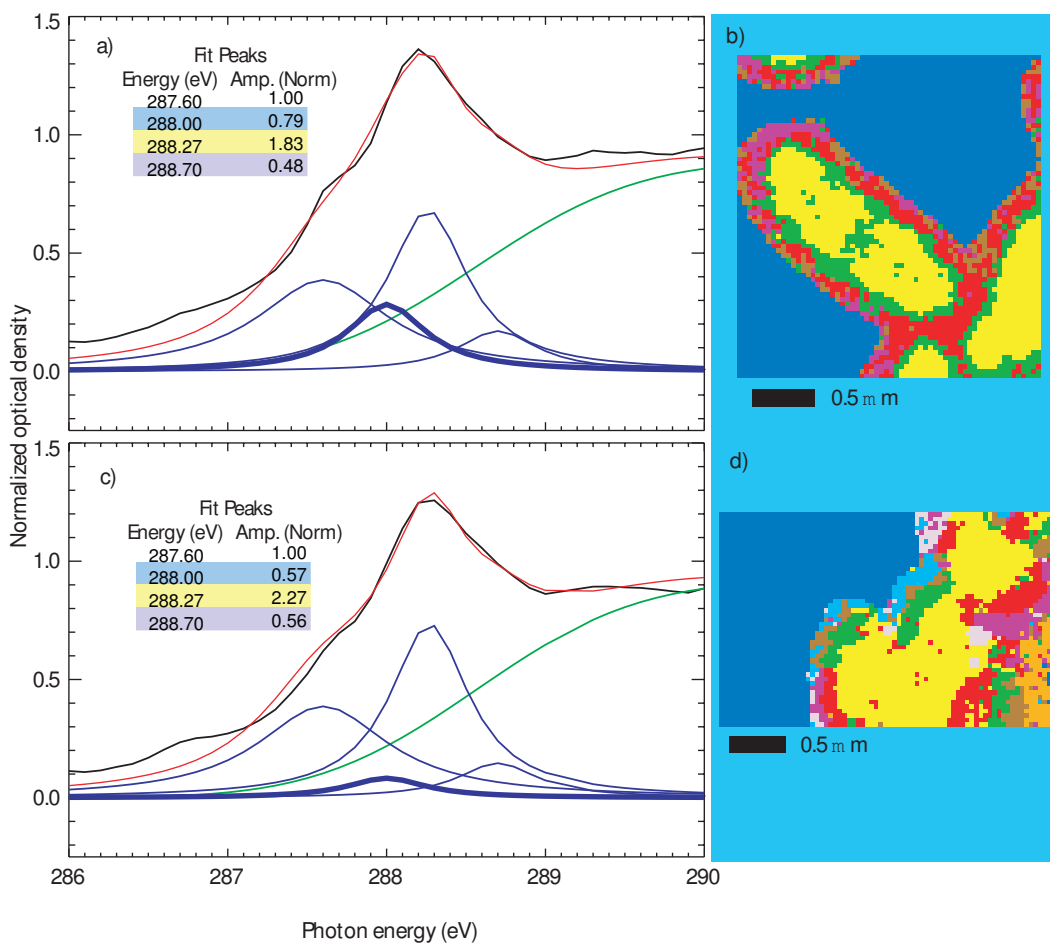nickel accumulation for spectroscopic analysis, as described in Section 2.4. For the CH34 sample grown in the presence of nickel, simultaneous bright and dark field images were collected over the O1s edge, 520-560 eV. The dark field images are shown in Figure 4.19. A threshold of 2430 kHz was used to identify bright pixels in the 520 eV dark field image (a), then overlaid on the bright field image in (d).

The same process was used to identify nickel precipitates for the CH34 sample with nickel added to the resting bacteria. Figure 4.20 shows the dark field image in (a). The precipitates were identified using a threshold flux of 600 kHz as shown in (e). The bright field image in (c) does not indicate the presence of nickel, but shows a wide margin of EPS surrounding the cell. The dark field pixels overlaid on the bright field image in (d) indicates that the nickel precipitates are closely associated with the cell wall and the EPS.

By combining the detailed analyses of the carboxyl peak in C K-edge spectra and darkfield scattering images of nickel hydroxide precipitates, the STXM results indicate that both active metabolic and passive sorption mechanisms play significant roles in controlling the concentration of bioavialable nickel in the near-cell environment. These results are important because they provide the chemical identity, stoichiometry and spatial distribution of Ni complexes and precipitates. This information is necessary for coupling in silico models of metabolic pathways with models to predict bacterial behavior and metal resistance in natural and industrial processes.

Figure 4.19: Dark field and bright field images of CH34 *Clostridium* bacteria [20] grown in the presence of nickel. a) Dark field image of CH34 grown in the presence of nickel chloride. b) Dark field image with overlay of pixels which lie above the flux threshold, as chosen using the histogram in (e). c) The bright field image does not indicate the presence of nickel precipitates. d) Bright field image with dark field pixels superimposed. This indicates that there most likely are nickel precipitates present, and they tend to be closely associated with the cell.

a) Dark field b) Dark field with threshold

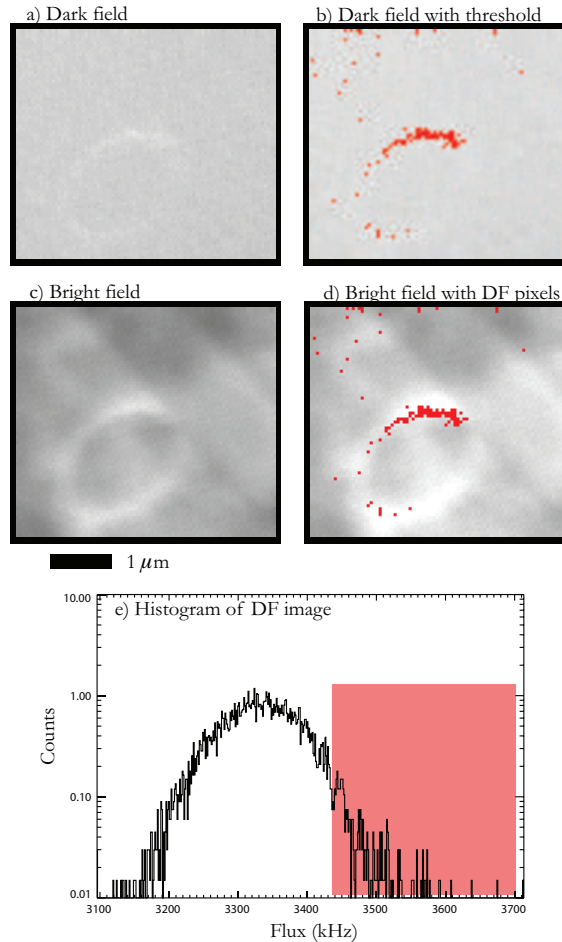c) Bright field d) Bright field with DF pixels

e) Histogram of DF image flux
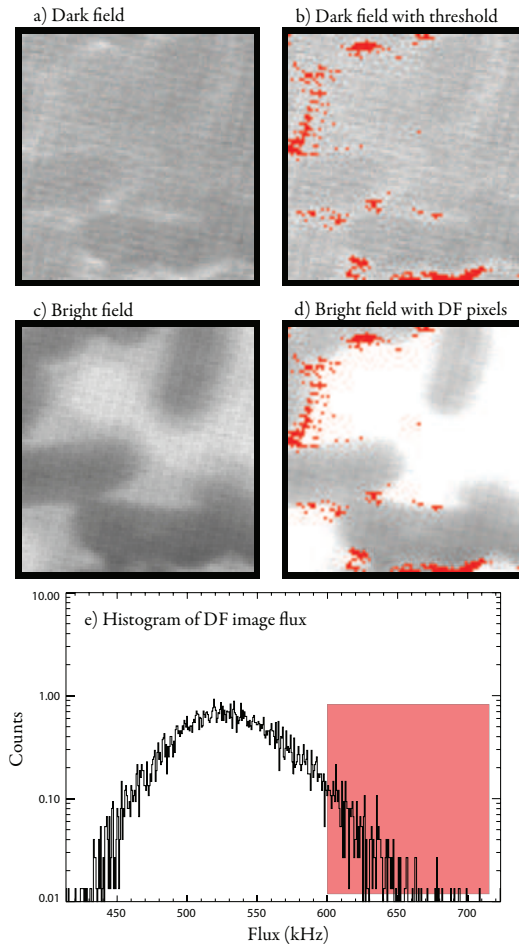
Figure 4.20: Dark field and bright field images of CH34 *Clostridium* bacteria [20] with nickel added. a) Dark field image of CH34 with nickel added. b) The dark field image with overlay of pixels which lie above the flux threshold suggests that the nickel does form precipitates when in contact with the bacteria. c) The bright field image shows a wide margin of exopolysaccharides surrounding the cell, and the superimposed dark field pixels in (d) indicate that the precipitates tend to clump in the exopolysaccharides surrounding the cell. e) Histogram of pixel flux in dark field image.

Chapter 5

Conclusions and Outlook

This thesis concerns the use of soft x-ray microscopy to study issues in the interaction of bacteria with environmental contaminants. Following the introduction to microscopy in Chapter 1, x-ray microscopy in Chapter 2, and the discussion of near-edge spectroscopy in Chapter 3, in Chapter 4 a number of applied studies of bacteria were reported.

In Chapter 4 we investigated many questions that pertain to bacterial chemistry. In this section I will summarize the findings from each section of that chapter.

In Section 4.2.1 we showed that it may be possible to determine the difference between gram-positive and gram-negative bacteria in a mixed colony. We did this by comparing samples of gram-positive and gram-negative bacterial cell-wall spectra to standard spectra. The standard spectra chosen were peptidoglycan, which makes up more than 50% of the gram-positive cell wall, and lipoteichoic acid, which is only present in the gram-positive cell wall. A comparison of these spectra show that the strong 288 eV peak, which corresponds to the carboxyl functional group, is indicative of a larger number of carboxyl groups in the gram-positive cell wall. This can be attributed to the larger fraction of peptidoglycan in the gram-positive cell wall. This technique could be useful for identifying the gram character of a cell in a sample with mixed bacterial types. From a single data set one could first identify the gram character of the cell and then identify other interactions of interest, such as nickel resistance or iron mineral interactions. However, in order to know whether this is in fact a definitive indication of a larger number of types of gram-positive cell, more examples of gram-positive and gram-negative cells need to be examined.

PHB granules are a method of carbon storage to be used by the organism in times of nutrient deprivation. These granules may also play a significant role in contaminant sequestration. If a suitable spectral signature could be identi-

fied for PHB, these interactions could be studied using STXM techniques. In Section 4.2.2, a polyhydroxybuterate (PHB)-producing *Ralstonia* bacterium was studied in order to determine whether the PHB granules can be identified using STXM. The large granules formed by the wild-type *Ralstonia* were identified by the cluster analysis. It was difficult to compare them with a pure PHB standard because the near-edge spectrum of PHB shows a single step-edge without distinct near-edge resonances.

Section 4.2.3 shows that spores and endospores can be identified using STXM. Not only are the spores visible in absorption images, but the spectral signature of the spores is unique and clearly identifies the spore as being different from the vegetative cell. While the stages of sporulation cannot be differentiated, it is still important that the presence of very young endospores can be readily identified. This can lead to studies of the interaction between the sporulating cell and its environment, and one could imagine developing studies that could investigate the binding of metals and other contaminants to the spore coat, as indicated by the changes of the spectrum associated with the spore. Sporulation is a common method used by organisms to resist harsh conditions, and STXM could be used to identify the mechanisms by which the spores interact with their environment.

The interaction between iron minerals and bacteria can be studied in two ways: using both the carbon and the iron absorption edges. The iron L_2 edge spectrum of the iron mineral indicates the valence state of Fe in the mineral. The carbon edge spectrum indicates changes in the binding of the carbon atoms in the sample, and so can tell us about the functional group responsible for binding with the iron. We also can identify where in the sample most of the iron binding is taking place, whether inside or outside the cell, associated with the cell wall or the exopolysaccharides. Specific examples of naturally occurring iron minerals ferrihydrite and goethite and the bacterium *Clostridium* BC1 were used in Section 4.3. The two standard minerals were naturally found in the 3+ state, as indicated by the strong peak at 710 eV compared to the peak at 708 eV, which indicates the 2+ state. In this way we can then determine what effect an interaction with an organism will have on the valence state of the iron mineral. For example, the interaction between the mineral ferrihydrite and the bacterium *Clostridium* BC1 changes the valence state of the ferrihydrite to primarily a 2+ state from the naturally-occurring 3+ state.

In the case of the *Clostridium* BC1, the ferrihydrite was determined to bind to the carboxyl groups in the cell as indicated by the large shift in the 288 eV peak. This peak shift was only found in areas of the sample that correspond to the exopolysaccharides.

97

The last set of data, discussed in Section 4.5 of this thesis, was nickel-bacterial interactions. Nickel is a metal that is generally toxic to organisms in excess. However, there are known nickel-resistant bacteria. We wished to determine whether STXM could be used to find new information about this interaction between the nickel and the resistant organisms. What we found is that the changes to carbon chemistry were very subtle, and careful peak-fitting was required to determine whether nickel binding does occur at the carboxyl group. If this is done carefully, we can determine the physical location of the nickel binding, whether the nickel is inside the cell or outside the cell, associated with the cell wall or more generally associated with the EPS.

In this thesis I also showed that dark field imaging is a useful tool to determine the presence and location of small scatterers such as gold labels or, as shown in Section 4.5.1, nickel precipitates. We showed that the nickel that is expelled from the cell forms a nano-sized precipitate that is then associated with the exterior of the cell wall. This information is not available in the bright field image, and so is a complimentary method to the absorption imaging and spectroscopy discussed in other sections.

While Sections 4.2.1, 4.2.2 and 4.2.3 describe methods for identifying spectral signatures of subcellular features such as the cell wall, carbon-storage polymers and spores, Sections 4.3-4.5 deal with metal interactions with the microorganisms. This thesis has shown that STXM is a method that can be used to answer many questions about bacterial chemistry and structure with 40 nm spatial resolution. Environmental scientists have not had a method such as STXM to probe these questions before, as most commonly used methods require extensive sample preparation (electron microscopy, visible light microscopy) that may alter the chemistry of the sample, or low spatial resolution that cannot probe the subcellular features of the cell (visible light microscopy). Other bulk methods have no spatial resolution, and determine the chemistry of an entire sample. STXM can be used as a very powerful tool to compliment these traditional techniques by providing chemical information at a subcellular level as well as the spatial distribution of precipitates and other labels.

Looking to the future, the construction of the NSLS II synchrotron at Brookhaven National Lab promises to bring higher flux and better spatial resolution to our efforts. Higher flux will result in faster data collection times, which can mean a higher throughput of samples. Spatial resolution of a few nanometers could mean probing in even more detail the subcellular chemistry, such as the cell wall, PHB granules and spores. All of these advances should make STXM an even greater asset to the environmental science community.

Bibliography

[1] A.T. Stone and J.J. Morgan. *Reductive dissolution of metal oxides*, pages 221–254. John Wiley & Sons, 1987.

[2] Ernst Abbe. Note on the proper definition of the amplifying power of a lens or a lens-system. *Journal of the Royal Microscopical Society*, 4: 348–351, 1884.

[3] R. Brydson. *Electron Energy Loss Spectroscopy*. BIOS Scientific Publishers, UK, 2001.

[4] R.F. Egerton. *Electron Energy-loss Spectroscopy in the Electron Microscope, 2nd Ed.* Plenum Press, NY, 1996.

[5] R.D. Young. *Phys. Rev.*, 113:110–114, 1959.

[6] H. Wolter. Spiegelsysteme streifenden Einfalls als abbildendeOptiken für Röntgenstrahlen. *Ann. Phys.*, 10:94–114, 286, 1952.

[7] H. Ade, X. Zhang, S. Cameron, C. Costello, J. Kirz, and S. Williams. Chemical contrast in x-ray microscopy and spatially resolved XANES spectroscopy of organic specimens. *Science*, 258:972–975, 1992.

[8] J.D. Jackson. *Classical Electrodynamics*. John Wiley & Sons, 1998.

[9] David Attwood. *Soft X-Rays and Extreme Ultraviolet Radiation*. Cambridge University Press, 1999.

[10] C. Buckley, H. Rarback, R. Alforque, D. Shu, H. Ade, S. Hellman, N. Iskander, J. Kirz, S. Lindaas, I. McNulty, M. Oversluizen, E. Tang, D. Attwood, R. DiGennaro, M. Howells, C. Jacobsen, Y. Vladimirsky, S. Rothman, D. Kern, and D. Sayre. Soft x-ray imaging with the 35 period undulator at the NSLS. *Review of Scientific Instruments*, 60:2444–2447, 1989.

[11] C. Jacobsen, J. Kirz, and S. Williams. Resolution in soft x-ray microscopes. *Ultramicroscopy*, 47:55–79, 1992.

[12] B. L. Henke, E. M. Gullikson, and J. C. Davis. X-ray interactions: Photoabsorption, scattering, transmission, and reflection at E=50–30,000 eV, Z=1–92. *Atomic Data and Nuclear Data Tables*, 54:181–342, 1993.

[13] M. Lu. *Nanofabrication of Fresnel zone plates for soft X-ray imaging at carbon edge*. PhD thesis, Department of Physics and Astronomy, Stony Brook University, 2006.

[14] Holger Fleckenstein. PhD thesis, SUNY Stony Brook, 2008.

[15] M. Lerotić. *Finding the patterns in complex specimens by improving the acquisition and analysis of x-ray spectromicroscopy data*. PhD thesis, Department of Physics and Astronomy, Stony Brook University, 2005.

[16] H. N. Chapman, C. Jacobsen, and S. Williams. A characterisation of dark-field imaging of colloidal gold labels in a scanning transmission x-ray microscope. *Ultramicroscopy*, 62(3):191–213, 1996.

[17] H. N. Chapman, J. Fu, C. Jacobsen, and S. Williams. Dark-field x-ray microscopy of immunogold-labeled cells. *Journal of the Microscopy Society of America*, 2(2):53–62, 1996.

[18] S. Vogt, H. N. Chapman, C. Jacobsen, and R. Medenwaldt. Dark field x-ray micrscopy: the effects of condenser/detector aperture. *Ultramicroscopy*, 87:25–44, 2001.

[19] D. Sayre, J. Kirz, R. Feder, D. M. Kim, and E. Spiller. Transmission microscopy of unmodified biological materials: Comparative radiation dosages with electrons and ultrasoft x-ray photons. *Ultramicroscopy*, 2:337–341, 1977.

[20] Safieh Taghavi, Hilde DeLanghe, Cindy Lodewyckx, Max Mergeay, and Daniel van der Lelie. Nickel-resistance-based minitransposons: New tools for genetic manipulation of environmental bacteria. *Applied and Environmental Microbiology*, pages 1015–1019, 2001.

[21] M. Lerotic, C. Jacobsen, J.B. Gillow, A.J. Francis, S. Wirick, S. Vogt, and J. Maser. Cluster analysis in soft x-ray spectromicroscopy: finding the patterns in complex specimens. *Journal of Electron Spectroscopy and Related Phenomena*, 144-147:1137–1143, 2005.

[22] M. Lerotic, C. Jacobsen, T. Schäfer, and S. Vogt. Cluster analysis of soft x-ray spectromicroscopy data. *Ultramicroscopy*, 100(1-2):35–57, 2004. doi: 10.1016/j.ultramic.2004.01.008.

[23] E.R. Malinowski. *Factor Analysis in Chemistry*. John H. Wiley & Sons, New York, 2nd edition, 1991.

[24] B.S. Everitt, S. Landau, and M. Leese. *Cluster Analysis*. Arnold Publishers, London, 4th edition, 2001.

[25] C. Jacobsen, G. Flynn, S. Wirick, and C. Zimba. Soft x-ray spectroscopy from image sequences with sub-100 nm spatial resolution. *Journal of Microscopy*, 197(2):173–184, 2000.

[26] X. Zhang, R. Balhorn, J. Mazrimas, and J. Kirz. Mapping and measuring DNA to protein ratios in mammalian sperm head by XANES imaging. *Journal of Structural Biology*, 116:335–344, 1996.

[27] K. Pearson. *Philosiphical Magazine*, 2(Series 6):559, 1901.

[28] H. Hotelling. *Journal of Education Psychology*, 24:417, 1933.

[29] S. R. Wasserman. The analysis of mixtures: Application of principle components analysis to XAS spectra. *Journal de Physique IV*, 7 (C2): 203–205, 1997.

[30] N. Bonnet, N. Brun, and C. Colliex. Extracting information from sequences of spatially resolved eels spectra using multivariate statistical analysis. *Ultramicroscopy*, 77:97–112, 1999.

[31] P. L. King, R. Browning, P. Pianetta, I. Lindau, M. Keenlyside, and G. Knapp. Image-processing of multispectral x-ray photoelectron-spectroscopy images. *Journal of Vacuum Science and Technology A*, 7 (6):3301–3304, 1989.

[32] A. Osanna and C. Jacobsen. Principle component analysis for soft x-ray spectromicroscopy. pages 350–357. XRM, 1999.

[33] Chein-I Chang. *Hyperspectral Imaging: Techniques for Spectral Detection and Classification*. Kluwer Academic/Plenum Publishers, 2003.

[34] B. L. Henke, P. Lee, T. J. Tanaka, R. L. Shimabukuro, and B. K. Fujikawa. Low-energy x-ray interaction coefficients: photoabsorption, scattering, and reflection. *Atomic Data and Nuclear Data Tables*, 27:1–144, 1982.

[35] K. Kaznacheyev, A. Osanna, C. Jacobsen, O. Plashkevych, O. Vahtras, H. Ågren, V. Carravetta, and A. P. Hitchcock. Innershell absorption spectroscopy of amino acids. *Journal of Physical Chemistry A*, 2002. In press.

[36] Derek R. Lovley. Cleaning up with genomics: applying molecular biology to bioremediation. *Nature Reviews*, 1:35–44, 2003.

[37] W.F. Fitzgerald, C.H. Lamborg, and C.R. Hammerschmidt. Marine biogeochemical cycling of mercury. *Chemical Reviews*, 107(2):641–662, 2007.

[38] D.R. Lovley, E.J.P. Phillips, Y.A. Gorby, and E.R. Landa. Microbial reduction of uranium. *Nature*, 350:413–416, 1991.

[39] Albert G. Moat and John W. Foster. *Microbial Physiology*. John Wiley & Sons, 1995.

[40] A.J. Francis and C.J. Dodge. Anaerobic dissolution of transition and heavy metal oxides. *Applied and Environmental Microbiology*, 54:1009–1014, 1988.

[41] M.T. Madigan, J.M. Martinko, and A. W. J. Parker. *Biology of Microorganisms*. Prentice Hall/Pearson Higher Education Group, 2003.

[42] A.J. Francis, C.J. Dodge, F. Lu, G.P. Halada, and C.R. Clayton. Xps and xanes studies of uranium reduction by clostridium sp. *Environmental Science and Technology*, 28(4):636–639, 1994.

[43] A.J. Francis, C.J. Dodge, J.B. Gillow, and H.W. Papenguth. Biotransformation of uranium in high ionic strength brine by a halophilic bacterium under denitrifying conditions. *Environmental Science and Technology*, 34(10), 2000.

[44] J.B. Gillow, M. Dunn, A.J. Francis, D.A. Lucero, and H.W. Papenguth. The potential of subterranean microbes in facilitating actinide migration at the grimsel test site and waste isolation pilot plant. *Radiochimica Acta*, in press.

[45] J.B. Gillow, A.J. Francis, C.J. Dodge, R. Harris, T.J. Beveridge, P.V. Brady, and H.W. Papenguth. Actinide biocolloid formation in brine by halophilic bacteria. In *Mat. Res. Soc. Symp. Proc.*, volume 556, pages 1133–1140, 1999.

[46] T. Schäfer, F. Claret, A. Bauer, L. Griffault, E. Ferrage, and B. Lanson. Natural organic matter (NOM)-clay association and impact on Callovo-Oxfordian clay stability in high alkaline solution: spectromicroscopic evidence. *Journal de Physique IV*, 104:413–416, 2003.